

# The $^{152}\text{Sm}(p,n)$ reaction and its astrophysical importance

Dissertation  
zur Erlangung des Doktorgrades  
der Naturwissenschaften

vorgelegt beim Fachbereich Physik  
der Goethe Universität  
Frankfurt am Main

von  
**Moritz Pohl**  
aus Frankfurt am Main

Frankfurt am Main 2014  
(D30)

vom Fachbereich Physik der  
Goethe-Universität Frankfurt als Dissertation angenommen.

**Dekan:** Prof. Dr. René Reifarth  
**Gutachter:** Prof. Dr. René Reifarth  
Dr. Kerstin Sonnabend

Datum der Disputation : 17.12.2014

*What can be asserted without evidence  
can be dismissed without evidence*

HITCHENS'S RAZOR





# Abstract

Within the nucleosynthetic processes of the slow neutron-capture reaction network (called the *s process*) the so called branching points, unstable isotopes where different nuclear reactions are competing, are important to understand. For modeling and calculating the nucleosynthesis and compare the resulting abundances to the observed ones, it is indispensable to know the branching ratios as well as the corresponding cross sections.

A great challenge in measuring those rates in experiments may be the radioactivity of the isotopes involved, which can make it nearly impossible to manufacture the needed targets. In addition, in stellar environments the excited states of isotopes can be in equilibrium with the ground state, affecting the half-lives and the branching ratios significantly. The isotope  $^{152}\text{Eu}$  is such a branching point, with neutron captures and  $\beta$ -decays competing. Those challenges were approached in the s405 experiment performed at the GSI Helmholtzzentrum für Schwerionenforschung GmbH: the challenge of the radioactivity can be approached by experiments carried out in inverse kinematics with radioactive beams, solving the problem of unstable targets. Also a reversed reaction was used to access the excited states of the studied isotope. The performed  $^{152}\text{Sm}(p,n)^{152}\text{Eu}$  is a pioneering attempt to use those methods on heavy ions. The (p,n) reaction was used as a substitute for electron capture, the focus lies on reactions with low-momentum transfers, resulting in the emission of low-energy neutrons. The new developed low-energy detector array LENA was put to test for the first time in the s405 experiment.



# Inhaltsangabe

Verzweigungspunkte im Netzwerk der langsamen Neutroneneinfangprozesse sind ein Schwerpunkt der aktuellen Forschung im Gebiet der nuklearen Astrophysik. Für die Modellierung der Isotopenhäufigkeit und damit des Verständnisses der gesamten Nukleosynthese ist es unabdingbar, die Reaktionsraten und Verzweigungsverhältnisse zu kennen. Schwierigkeiten bei der Messung dieser treten beispielsweise auf, wenn die involvierten Isotope radioaktiv sind: Isotope mit einer kurzen Halbwertszeit eignen sich nicht für die Targetproduktion. Zudem können sich in stellaren Umgebungen angeregte und Grundzustände eines Isotopes in einem thermischen Gleichgewicht befinden. Da angeregte Zustände eine gegenüber dem Grundzustand abweichende Halbwertszeit haben können, führt dieses Gleichgewicht zu einer Änderung der Zerfallszeiten gegenüber nur im Grundzustand liegenden Isotopen, wie im Labor meist üblich. Der Verzweigungspunkt  $^{152}\text{Eu}$  ist solch ein Fall.

Für beide Herausforderungen gibt es am s405 Experiment, durchgeführt am GSI Helmholtzzentrum für Schwerionenforschung GmbH, einen Lösungsansatz. Studiert wurde die Reaktion  $^{152}\text{Sm}(p,n)^{152}\text{Eu}$  in inverser Kinematik. Die Ausnutzung von inverser Kinematik erlaubt es, an Stelle radioaktiver Targets radioaktive Strahlen zu nutzen.

Des Weiteren wird durch die Substitution des Elektroneneinfangprozesses durch eine Ladungsaustauschreaktion der eigentliche Zerfall umgedreht und vom Zerfallsprodukt ausgehend studiert. Dies hat den Vorteil, dass auf diesem Wege angeregte Zustandslevel des zu vermessenden Kerns bevölkert werden können. Eine Folge der Ladungsaustauschreaktion ist die Emission von niederenergetischen Neutronen in großem Winkel relativ zum Target. Um diese zu messen wurde ein neuer Detektor, LENA, entwickelt und das erste mal unter vollen experimentellen Bedingungen getestet. Eine Zusammenfassung der Arbeit samt des Ergebnisses in deutscher Sprache befindet sich im Anhang.



# Contents

<b>1</b>	<b>Preface</b>	<b>1</b>
1.1	Astrophysical Motivation	1
1.2	Nucleosynthetic Processes	4
1.2.1	Primordial Nucleosynthesis	4
1.2.2	Nucleosynthesis in Stars	5
1.2.3	The Stellar s Process	8
1.2.3.1	Branching Points	10
1.2.3.2	Components I: The Main s Process	14
1.2.3.3	Components II: The Weak s Process	15
1.2.4	Other Stellar Nucleosynthesis Processes	17
1.2.4.1	The r Process	17
1.2.4.2	The Production of Proton-rich Isotopes	17
1.3	Nuclear Reactions in the Laboratory	19
1.3.1	Reactions in Inverse Kinematics	19
1.3.1.1	Limitations of Experimental Approaches	19
1.3.2	The (p,n) Reaction as a Probe of the Beta-Decay Strength	20
1.3.2.1	Charge-Exchange Reactions	20
1.3.2.2	Gamow-Teller and Fermi Transitions	20
1.3.2.3	Similarity between B(GT) and (p,n) Reactions	23
<b>2</b>	<b>The Experimental Method</b>	<b>25</b>
2.1	Basics	25
2.2	The Low-Energy Neutron detector Array LENA	29
2.2.1	Operating Mode of a Scintillation Detector	30
2.2.2	Characteristics and Testing	32
2.2.3	LENA in s405	33

<b>3</b>	<b>The Infrastructure</b>	<b>35</b>
3.1	The LAND/R <sup>3</sup> B Setup at the GSI Helmholtzzentrum	35
3.2	Other Detectors used in the s405 Experiment	38
3.2.1	ROLU	38
3.2.2	POS	39
3.2.3	LaBr <sub>3</sub> :Ce	40
3.2.4	GFI	41
3.2.5	TFW	42
3.3	Further Devices in the Beam Line	43
3.3.1	The Target	43
3.3.2	ALADIN	44
<b>4</b>	<b>Data Acquisition and Analysis</b>	<b>45</b>
4.1	Electronics and Software	45
4.1.1	Data Acquisition and Trigger Patterns	45
4.1.2	The Land02 Framework	48
4.2	Detector Calibration	49
4.2.1	CLOCK and TCAL	49
4.2.2	POS	49
4.2.3	LaBr <sub>3</sub> :Ce	50
4.2.4	LENA	52
4.2.4.1	Calibration of Time and Energy	52
4.2.4.2	Position Reconstruction of LENA	54
4.2.5	GFI	58
4.2.6	TFW	59
<b>5</b>	<b>Results and Discussion</b>	<b>61</b>
5.1	Removal of the Background Contribution	61
5.2	Data Selection Steps	63
5.2.1	Reconstruction of the Kinetic Energy	63
5.2.1.1	Time-of-Flight	64
5.2.1.2	Inverted Velocity	66
5.2.1.3	Reconstruction of the Kinetic Energy	68
5.2.2	Neutron-Related Cuts	69
5.2.2.1	Trigger Patterns	69
5.2.2.2	Deposited Energy - DSS 3	71

5.2.3	Non-Neutron-Related Data Selection	74
5.2.3.1	Analyzing the $\gamma$ -Energy Signals	74
5.2.3.2	Separating Reaction Products from the Unreacted Beam	78
5.2.3.3	Combining the $Z$ Determination - DSS 5	84
5.2.4	Summary	87
5.3	Calculating the $E_{\text{kin}}$ as a Function of $\Theta_{\text{lab}}$	88
5.4	Simulation of LENAs Response to Neutrons	90
<b>6</b>	<b>Summary and Perspectives</b>	<b>95</b>
6.1	Summary	95
6.2	Perspectives	99
6.2.1	Future Plans - R <sup>3</sup> B at FAIR	99
	<b>Bibliography</b>	<b>i</b>
	<b>List of Figures</b>	<b>v</b>
	<b>List of Tables</b>	<b>ix</b>





# 1

## Preface

### 1.1 Astrophysical Motivation

*Some part of our being knows this is where we came from. We long to return. And we can. Because the cosmos is also within us. We're made of star-stuff. We are a way for the cosmos to know itself.*

CARL SAGAN, COSMOS: A PERSONAL VOYAGE, 1990

The universe is filled with thin clouds of, mainly hydrogen, gas. Those clouds may collapse under gravitational pressure, forming spheres of hot, dense matter. When nuclear processes start and become the energy source of the now shining sphere, a star is born.

Within the stars, a tremendous variety of nuclear processes produces the melange of chemical elements that we encounter in our daily life.

Aside from hydrogen and helium, all elements are synthesized during the life and death of the stars, and finally blasted into the universe. The underlying mechanisms are the

## 1. Preface

research field of nuclear astrophysics, which aims ultimately for the complete understanding how the universe we observe today evolved during the last 13.8 billion years. Those produced and ejected elements can be found throughout our solar system, in grains extracted from meteoroids, in both, the bottom of the oceans as well as high up in the atmosphere of our planet earth, and even within our body.

The observed abundance distribution of isotopes in our solar system is shown in figure 1.1. The different production mechanisms, and thus the associated physical scenarios, are color-coded. A key ingredient to a quantitative description of the stellar nucleosynthesis-processes are the nuclear-reaction probabilities under stellar conditions - the stellar reaction-rates. Some can be determined easier than others in the laboratory, and the development of new tools and techniques expands the experimentally reachable reaction rates and reaction types continuously.

While there are successfully used techniques to measure the *s process* ( $n,\gamma$ ) reactions,  $\beta$ -decay measurements in nucleosynthesis reactions are less explored. To proof a new measurement principle for the  $\beta^+$ -decay/electron-capture rates, a detector specifically developed for the measurement of low-energy neutrons was put to test for the first time. This work explicates the motivation, experience and results of the performed experiment and furthermore possible consequences for future applications.

## 1.1 Astrophysical Motivation

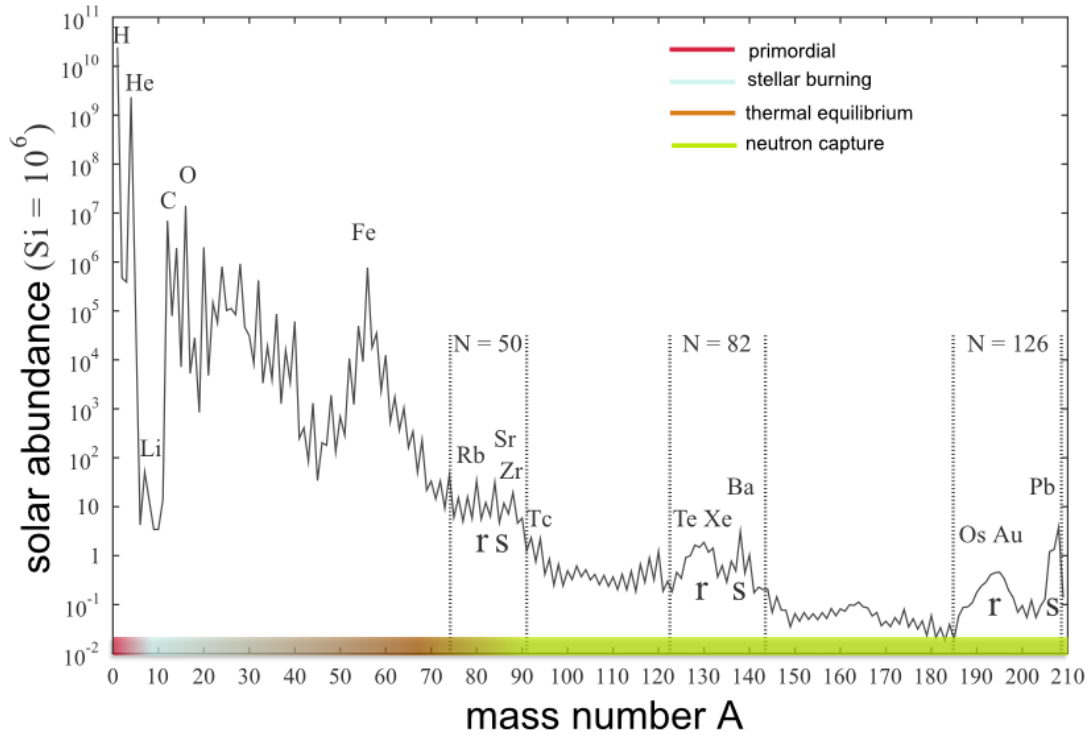


**Figure 1.1** – The abundances of isotopes as found in the solar system normalized to silicon. The lightest elements (red marked mass region) were produced during the primordial nucleosynthesis. The adjacent elements were produced during stellar burning (marked light-blue). The elements with a mass number between roughly  $A = 30$  and  $A = 65$  are produced in the nuclear statistical equilibrium with an abundance peak at  $^{56}\text{Fe}$ . All heavier elements are produced in the neutron captures as explained in chapter 1.2. Image by courtesy of [1], with data from [2].

(Note: There are no stable isotopes with a mass number of  $A = 5$  and  $A = 8$ )

## 1.2 Nucleosynthetic Processes

### 1.2.1 Primordial Nucleosynthesis

The diverse nuclear processes, producing elements, starting with the lightest elements around hydrogen and up to the heavy isotopes, are summarized under the term nucleosynthesis.

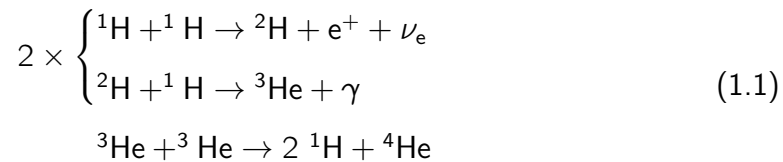
In the first minutes of the universe light isotopes were produced. Following current models, between  $10^{-6}$  and 1 seconds after the Big Bang, the quark-gluon plasma cooled down, leading to the hadronic freeze out. During this hadron epoch, protons and neutrons were formed from quarks. Hadrons and anti-hadrons were produced in nearly the same amount. The declining temperature lead eventually to an environment where the hadronization stopped, and thus, since no new hadron-anti-hadron pairs were produced anymore, to the annihilation of most of the existing matter. Only a residual of the original amount of formed hadronic matter continued to exist in the lepton epoch, which took place about 1 to 10 seconds after the Big Bang. In this period, lepton-antilepton pairs were produced in a thermal equilibrium, until the temperature of the universe dropped below the production threshold and just a small fraction of the leptons sustained the inevitable annihilation reactions [3].

Beginning roughly 3 minutes after the Big Bang and lasting around 15 minutes, the first nucleosynthesis phase, known as the primordial or Big Bang nucleosynthesis, started. It began with temperatures around  $10^{11}$  K and ended when the temperature dropped below  $10^9$  K, respectively. About 75-76 % of the produced mass abundances were  $^1\text{H}$ , roughly 25 %  $^4\text{He}$  and about 0.01 % deuterium. Even smaller amounts of lithium and beryllium (and possibly boron) were produced. No traces of heavier isotopes are found, implying that they are produced much later in processes in stars, where the primordial nucleosynthesis distribution serves as the seed [4, 5, 6].

### 1.2.2 Nucleosynthesis in Stars

The isotopes of elements with a mass number above  $A = 7$  are bred in stars. The elements up to a mass number of  $A = 56$  are created via fusion reactions. Those elements are marked with a blue and a orange color code in figure 1.1.

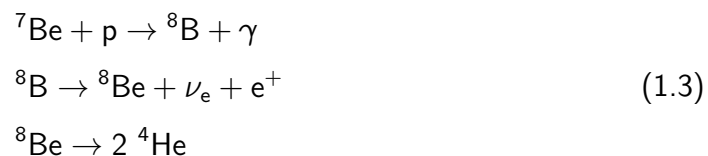
The first phase is the hydrogen burning. The occurring reactions depend on the mass of the star and its metallicity. First generation stars consist only of the isotopes available after the primordial nucleosynthesis. Therefore, only the so called *p-p chain* takes place. Three different reactions that produce one  ${}^4\text{He}$  isotope from four  ${}^1\text{H}$  are summed up with this term. In the sun about 91 % of the  ${}^4\text{He}$  is produced by this reaction-sequence (called *PP-I*):



If the temperature exceeds 14 million Kelvin, a second reaction-sequence (*PP-II*) is becoming the most relevant. It uses the in PP-I produced  ${}^4\text{He}$ :



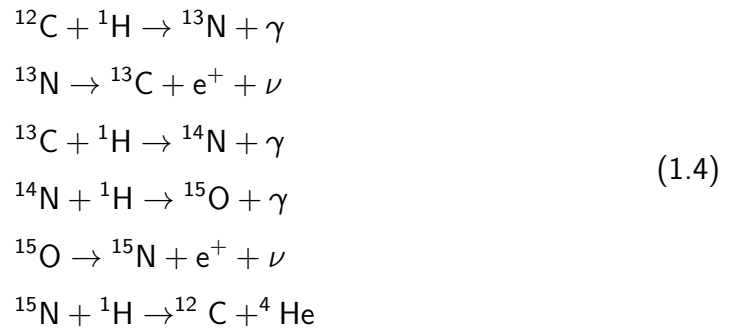
If the temperatures are even higher,  ${}^7\text{Be}$  can capture a proton instead of an electron. This reaction-sequence is also known as *PP-III*:



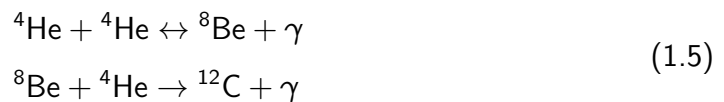
The mass difference between the four ingredient protons and one  ${}^4\text{He}$  is about 24.4 MeV (0.635 %). Those exothermic processes are the main energy source of the most stars on the sky, including the sun.

## 1. Preface

In second (and later) generation stars, where heavier isotopes like carbon and nitrogen are existent, the Bethe-Weizsäcker cycle (or *CNO-cycle*) takes place during the helium burning. The reaction also uses up four hydrogen isotopes to produce one helium isotope. Within the cycle, starting with  $^{12}\text{C}$ , heavier isotopes are built and destroyed, leaving  $^{12}\text{C}$  in the exit channel and therefore just using those heavier isotopes as a catalyst. The main CNO-cycle is described by equation (1.4):



The  $^{12}\text{C}$  isotopes needed in the CNO-cycle originate from the so called triple alpha process. This process occurs in helium burning phases in stars. Thus, it can take place in first generation stars with low metallicity and produces elements heavier than H and He. After the stars death the synthesized heavier elements are ejected into the interstellar medium (*ISM*), the initial material of new stars. The triple alpha process describes the synthesis of  $^{12}\text{C}$  from  $^4\text{He}$  isotopes. The involved reactions are:



Apart from the hydrogen and helium burning, there is a variety of other burning phases in the life cycle of a star which fuse elements and isotopes with increasing mass. Those phases are carbon-, neon- and oxygen burning, leading to the creation of elements up to the mass region between  $A = 40$  and  $A = 50$ . [4, 7, 8, 6]

With the increasing charge of the elements, the coulomb barrier poses an increasing resistance for fusion processes. This is reflected in figure 1.1 by the exponential decrease of the abundances in this mass region.

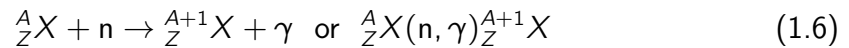
The production of elements with the masses around  $A = 56$  occurs during the thermal equilibrium in the silicon-burning phase. The temperatures are high enough to reach a statistical nuclear equilibrium, where the isotopes with the highest binding energy are formed. The maximum is reached at  $^{56}\text{Fe}$ , because elements with higher mass and a

## 1.2 Nucleosynthetic Processes

smaller binding energy require endothermic reactions to be reached, which in combination with the coulomb barrier prevents fusion reactions. From here on, neutron capture processes take place and produce heavier elements. Depending on the astrophysical scenario and the environmental variables two different neutron capture processes are distinguished, the slow neutron-capture process and the rapid neutron-capture process.

### 1.2.3 The Stellar s Process

Nucleosynthesis beyond the mass region of iron is almost impossible through fusion processes of charged particles. From this point on, the main nucleosynthesis proceeds mainly via the capture of neutrons:



Depending on the neutron-capture times and the astrophysical scenario associated with it, two different mechanisms are known: The rapid neutron-capture process, called the *r process* and the slow neutron-capture process, the *s process* [9, 10, 11, 12]. This work focuses on the latter, therefore it will be discussed in detail in this chapter. The *r process* and other possible nucleosynthetic processes for elements heavier than iron are briefly introduced in chapter 1.2.4.

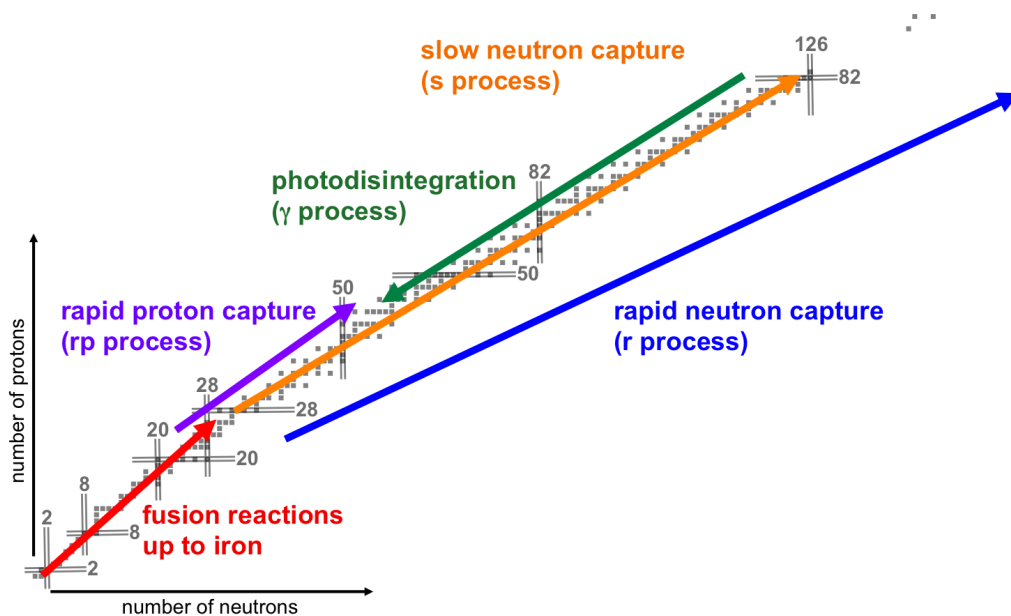


**Figure 1.2** – Schematic chart of nuclides with different nucleosynthetic processes. The figure shows the different nucleosynthesis processes and the mass region where they take place.

In figure 1.2 the different nucleosynthetic processes are shown, according to the region in the chart of nuclides where they occur. The *s-process* path runs along the *valley of stability*. The name refers to the energy per nucleon which is smaller for the stable isotopes than for the surrounding unstable ones, inhibiting decays.



The s process takes place in environments where the neutron fluxes are found in the range between  $10^5$  and  $10^{11}$  per  $\text{cm}^2$  per second and the temperature range between  $10^6$  and  $10^8$  K. Under these conditions the average neutron capture time for an isotope is in the order of years. In general, the further the mass flows away from the valley of stability, the shorter the half-life of the isotope. Once a  $\beta^-$ -unstable isotope is reached, it usually decays to the next element before a further neutron capture occurs.

The  $\beta^-$ -decay is a radioactive decay of an atomic nucleus, which is mediated by the weak force and where an electron is emitted. Due to the conservation of the lepton number, an antineutrino is emitted along with the  $\beta^-$ -particle:



In contrast to the neutron-capture reaction, the charge  $Z$  is changed during the decay, resulting in a change of the isotope  $X$  to the different chemical element  $Y$ . The continuous kinetic energy spectrum of the emitted electron ( $\beta^-$ ) ranges from zero to the maximal available energy, the  $Q$ -value, which depends on the excitation states of the parent and the daughter nuclei. In the chart of nuclides, where the neutron number is assigned to the abscissa and the number of protons to the ordinate, respectively, the reaction path went one step up and one to the left during a  $\beta^-$ -decay (compare figures 1.2 and 1.3). A more detailed view on the mechanisms of a  $\beta^-$ -decay is given in chapter 1.3.2.2.

### $\beta^+$ -decay and electron capture

The  $\beta^+$ -decay is related to the  $\beta^-$ -decay, following the same interactions and principles. A positron is emitted. The notation for the  $\beta^+$ -decay is



With a decreasing number of protons  $Z$  and a constant mass number  $A$ , in the chart of nuclides the reaction path goes one step down and one step to the right (compare figures 1.2 and 1.3). While the  $\beta^-$ -decay can occur on a single neutron, forming a proton, the  $\beta^+$ -decay is not possible on a single proton because the neutrons mass is slightly greater than the protons.

The electron capture reaction is a competitor of the  $\beta^+$ -decay. If the  $\beta^+$ -decay is energetically allowed, the electron capture is so, too. In proton rich nuclei, where the

## 1. Preface

energy difference between the initial and the final state is less than  $m_e c^2$ , a  $\beta^+$ -decay is not possible, so the electron capture is the only  $\beta$ -particle involving decay mode, making it the primary decay mode for proton rich nuclei. It is notated as



The necessary electron originates from the inner most shell of the atomic nucleus or from the stellar plasma. In the latter case, it is also possible that protons undergo a electron capture and become a neutron. This is a significant distinction from the  $\beta^+$ -decay. Often the capture of the electron leads to an energetically excited state of the nucleus. In this case the electron capture is followed by the emission of  $\gamma$ -rays. This is also true for  $\beta$ -decays to excited daughter states.

### 1.2.3.1 Branching Points

If the rates for two different reaction processes of an isotope are of the same order of magnitude, the processes are competing and the path of the s process branches. The figure 1.3 shows an excerpt of the chart of nuclides, with the s-process path drawn in. The thicker arrows mark the main s-process path, while the thinner ones depict the minor path after a branching point is passed. The mass flows from the stable  ${}^{149}\text{Sm}$  via neutron captures until the unstable branching point  ${}^{151}\text{Sm}$  is reached. This isotope has a  $\beta^-$ -decay half-life of 93 years (the blue color of the isotope in the chart of nuclides stands for a  $\beta^-$ -unstable isotope), which is in the same order of magnitude as the neutron capture time. Therefore the path branches. Most of the  ${}^{151}\text{Sm}$  is further processed via neutron captures until  ${}^{153}\text{Sm}$ , which decays before it can capture a neutron under s-process conditions.

The minor part of the s-process mass-flow reaches  ${}^{152}\text{Eu}$ , which is a branching point with three different processes in direct competition. Since the resulting abundances depend on the relative strength of the different branches, the knowledge of each of the competing reaction rates is important for detailed models of the s-process nucleosynthesis.

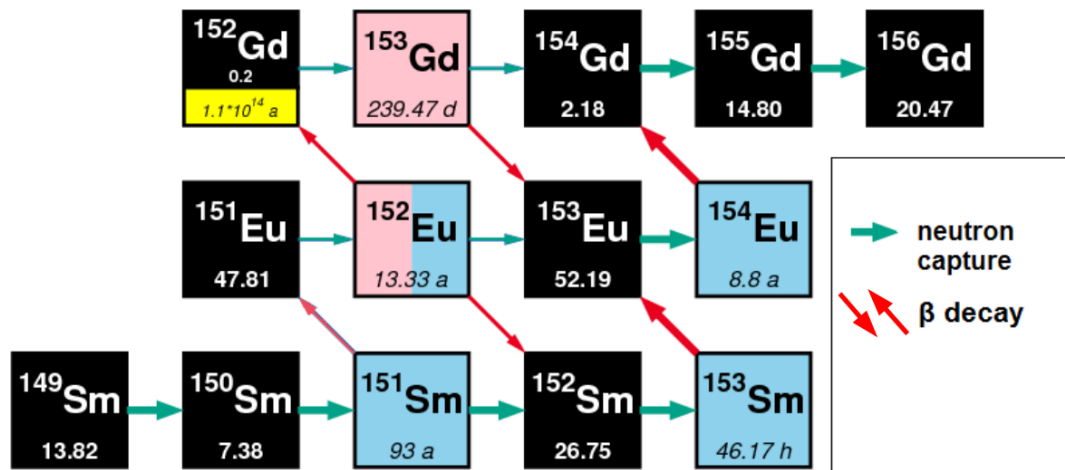


**Figure 1.3** – Excerpt of the chart of nuclides with focus on the s process branching point  $^{152}\text{Eu}$  and original color coding. The thick green arrows mark the major path of the s process, while the thinner blue ones the minor path after branching points. Blue dyed isotopes are  $\beta^-$ , red ones  $\beta^+$  - unstable isotopes, while the black ones are stable. Beneath the isotope name, the half-life, or for stable isotopes the percentage of all stable isotopes of the specific element is notated. The isotope  $^{152}\text{Eu}$  is a branching point where different decay or capture mechanisms are possible: The half-lives for the  $\beta^+$ - and  $\beta^-$ -decays are in the same order of magnitude as neutron-captures. It is elemental for the modeling of nucleosynthesis processes to have an excellent knowledge about branching ratios.

## 1. Preface

A huge challenge are the  $\beta$ -decay rates that may be different for different excitation levels of an isotope. The decay rates dependent on the population of ground state and excited states of the respective nucleus. Analogue to a comparable effect in particle reactions this may be described as *stellar enhancement*. The population of excitation levels depends on the temperature. For  $^{152}\text{Eu}$  the  $\beta^-$ -decay rates vary by six orders of magnitude for temperatures between 0.5 and  $5 \times 10^8$  K, the  $\beta^+$ -rates by up to four orders of magnitude [13]. The  $\beta$ -decay rates for  $^{152}\text{Eu}$  in dependence of the temperature are shown in figure 1.4.

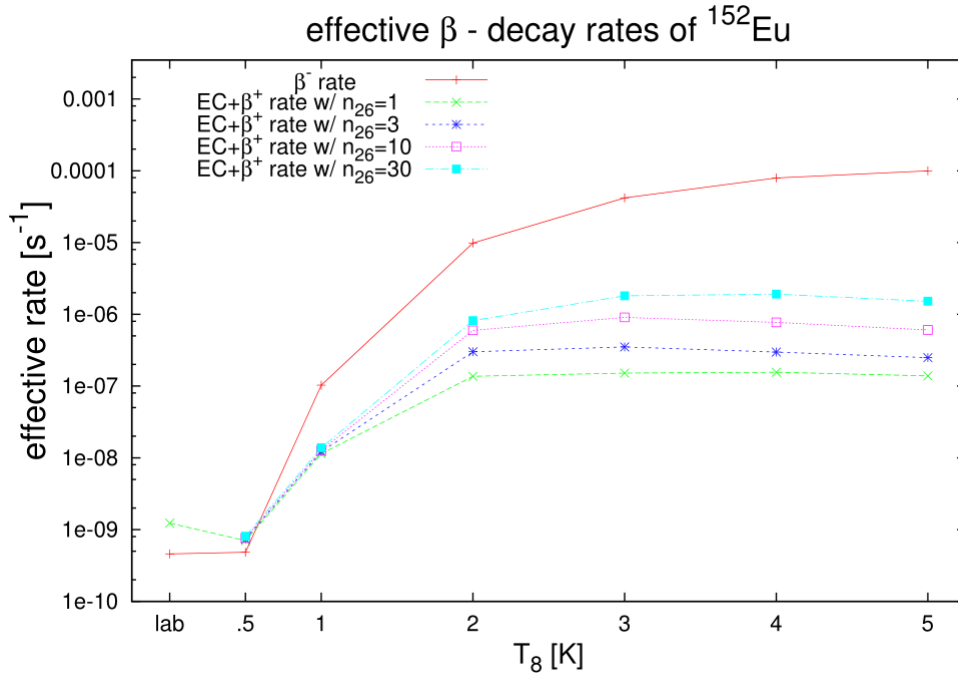


**Figure 1.4** – The calculated effective  $\beta$ -decay rates of  $^{152}\text{Eu}$  in dependence of the environment temperature. The decay rates under laboratory conditions are represented by (*lab*) on the abscissa. The effective rate is given in  $\text{s}^{-1}$  and the temperature in units of  $10^8$  K. In the  $\beta^+$ -decay rates the electron-capture rates are included. Different electron number densities are considered with  $n_{26}$  in units of  $10^{26} \text{ cm}^{-3}$ . All the effective rates are those under the condition of thermal equilibrium. Data from [13].

The s-process ends with the production of  $^{209}\text{Bi}$ . Since the following short-lived  $\alpha$ -emitters can not be overcome the mass-flow recycles [14].

While historically the s process was associated with a specific determined set of neutron densities and environment temperatures, nowadays it is commonly divided in two components: the main and the weak s process.

The main difference between the main and weak s process is the neutron exposure of the isotopes and hence the astrophysical scenario. Furthermore the main and weak s process are dominant in different ranges of the mass of the produced stable isotopes.

Classically, the main s process component can be described using coupled differential equations [9]. The equation 1.10 specifies for each isotope with the mass number  $A$  the change in the abundance  $N$  as a consequence of neutron capture and  $\beta$ -decay processes over time:

$$\frac{dN_{(A)}}{dt} = \lambda_{n(A-1)}N_{(A-1)} + \lambda_{\beta(A+1)}N_{(A+1)} - \lambda_{n(A)}N_{(A)} - \lambda_{\beta(A)}N_{(A)} \quad (1.10)$$

For stable nuclei the equation 1.10 evolves to

$$\frac{dN_{(A)}}{dt} = \sigma_{n(A-1)}v_{th}n_n N_{(A-1)} - \sigma_{n(A)}v_{th}n_n N_{(A)} \quad (1.11)$$

The term  $d\tau = v_{th}n_n dt$  represents the neutron flux in the star and can be inserted in equation 1.11:

$$\frac{dN_{(A)}}{d\tau} = \sigma_{n(A-1)}N_{(A-1)} - \sigma_{n(A)}N_{(A)} \quad (1.12)$$

It was shown that not all observable abundances can be reproduced with only one scenario. Different neutron exposures, thus a varying ratio between neutrons and seed isotopes are needed to recreate the abundances. This is eventually leading to the distinction between the main and the weak s process and the associated scenarios with different metallicities, meaning stars from different generations [15].

## 1. Preface

### 1.2.3.2 Components I: The Main s Process

The main s process is especially affiliated with the production of isotopes with a mass number greater than  $A = 90$ . It is affiliated with stars in the asymptotic giant branch (AGB). The name is derived from the position of the star in the Hertzsprung-Russell Diagram.

The stars in the asymptotic giant branch undergo two different phases, which have to be distinguished. In the first, the stars reside in a phase of hydrogen burning. The nuclear fusion reactions in the hydrogen core of the star have been explained in section 1.2.2. During those processes, the star lacks the neutrons needed for the reaction in the s process. The hydrogen burning is eventually leading to a helium-enriched core. If enough helium is available, the helium burning starts. The fusion of helium particles leads to the production of the carbon isotope  $^{12}\text{C}$ . After the completion of the helium core burning, the star enters the thermal pulse phase (TP-AGB).

The core consists now mostly of carbon and oxygen, while the helium shell surrounding it (which is again enclosed by hydrogen) is still subject to fusion reaction until it is depleted of helium. Then the star swells, becoming a red giant. During the TP-AGB phase, the helium burning is triggered again and stops after some time: The fusion processes in the outer hydrogen shell of the star supply the inner shell with new helium. The helium burning starts again until too much helium is consumed and the helium burning fades. During those phases of helium burning the star expands while it contracts during the non-burning phases. This pulsing is in progress for a period of some hundreds of years for the active pulse and some thousands of years for the time between the pulses, while the exact sequences depend on the mass of the individual star.

During the pulses are produced via the reactions  $^{13}\text{C}(\alpha, n)^{16}\text{O}$  (with neutron densities up to  $10^7 \frac{1}{\text{cm}^3}$  at around  $10^8 \text{ K}$ ) and  $^{22}\text{Ne}(\alpha, n)^{25}\text{Mg}$  (with neutron densities up to  $10^9 \frac{1}{\text{cm}^3}$  at around  $5 \times 10^8 \text{ K}$ ) during the thermal pulses, respectively [6, 10, 11].

### 1.2.3.3 Components II: The Weak s Process

While working well for elements with a mass of  $A = 90$  and higher, models using the processes mentioned in section 1.2.3.2 can not reproduce the observed abundances in the mass region between iron and strontium. If a different neutron flux is assumed and model calculations are fitted to the data, the abundances in the lower mass region can be reproduced while the heavier ones can not. This leads to the perception of a second s process with a different neutron exposure of the seed isotopes. Figure 1.5 shows the product for the  $(n,\gamma)$  cross section multiplied with the s-process abundance as a function of the mass number. The red line represents the product for a model with one the main s process taken into consideration. While it may reproduce the s-only nuclei (marked with circles) with an atomic mass of  $A = 90$  and higher, it fails to do so in the lower mass region. The blue line represents the model for the weak s process, which is in agreement with the lower mass region but fails with an atomic mass of  $A = 90$  and higher. The green line shows the current model with the combination of main and weak s process. This observation led to the conclusion that an additional mechanism has to exist [10, 16].

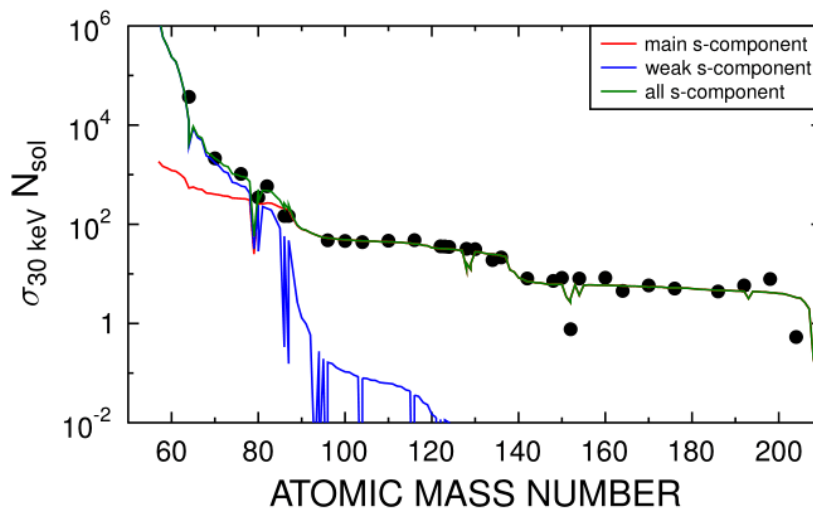


**Figure 1.5** – The product of s-process abundance and cross section as a function of the mass of the isotopes. The circles notate s-only isotopes. The red line represents the classical s process. It is apparent, that the lower mass isotopes are not reproduced correctly by it. Therefore, the mechanism of a weak s-process nucleosynthesis is introduced. It is shown as a blue line. The combination of both models is shown with the green line, which allows to reproduce the abundances of the s-only nuclei over the whole atomic mass range. Image by courtesy of [16].

## 1. Preface

Heavy stars with a mass greater than  $10 M_{\odot}$  are identified as the astrophysical scenario identified as the sites where the weak s process takes place. The  $^{14}\text{N}$  isotopes produced in the CNO cycle react via  $\alpha$ -capture to  $^{22}\text{Ne}$ . During this phase, temperatures up to  $T = 2.5 \times 10^8 \text{ K}$  are reached, initiating the  $^{22}\text{Ne}(\alpha, n)^{25}\text{Mg}$  reaction, neutrons are produced and provided for further reaction.

When the star evolves to a point where it reaches  $k_{\text{B}}T = 90 \text{ keV}$ , the neutron sources are activated for a second time, and the carbon shell burning via  $^{12}\text{C}(^{12}\text{C}, \alpha)^{20}\text{Ne}$  produces the needed  $\alpha$ -particles. The various burning phases are followed by the collapse of the star. In this procedure the core of the star is so compact, that electrons and protons form neutrons and neutrinos. Neutrinos escape and transport energy to the outer parts of the star, leading eventually to a supernova. The matter is released into the universe.

This influence of the carbon shell burning was taken into account to the theoretical approaches to the s process and results in a better reproduction of the observed abundances.



## 1.2.4 Other Stellar Nucleosynthesis Processes

### 1.2.4.1 The *r* Process

The rapid neutron-capture process (*r process*) is essentially similar to the discussed *s* process. The differences lay in the astrophysical scenario and the environmental variables.

In comparison to the *s* process, the neutron densities and temperatures in the *r* process environments are significantly higher. This leads to higher probabilities for neutron captures and allows unstable isotopes with a huge neutron excess to be produced. The need of the *r* process follows the abundances of isotopes of heavy elements. The creation of so called *r*-only isotopes can only be explained if the neutron-capture times are smaller than the half-life of the highly unstable isotopes. Therefore, the ratio between neutrons and isotopes has to be different from the one assumed in the *s*-process scenarios. There are different theories about the specific astrophysical sites, in which the *r* process takes place. Currently different possible scenarios are discussed to be the origin of the *r* process, although everything is speculation and a definite conclusion is not found yet.

One plenty discussed candidate are core-collapse supernovae. Those provide the necessary physical conditions for the *r* process. On the other hand, this theory and observations do only match, if the amount of *r*-process nuclei emitted in the core-collapse supernova is limited to a small fraction of what is observed. Besides core-collapse supernovae a second scenario is suggested: neutron-star mergers could play a role in the production of *r*-process nuclei, although this is just a theoretical consideration by now and lacks experimental fortification [7, 17, 18].

### 1.2.4.2 The Production of Proton-rich Isotopes

While the *s* and *r* process describe the nucleosynthesis via neutron-capture reactions, the proton-rich nuclei on the left hand of the valley of stability are produced via different reactions. About 35 stable isotopes can not, or not in the entire observed abundances, be produced by the *s* and *r* process.

In principle there are two basic reactions which can lead to the synthesis of a proton-rich nucleus. Analogue to the neutron capture in the *r* and *s* process, protons can be captured via ( $p,\gamma$ ) reactions. Because of the increasing Coulomb barrier, the capture

## 1. Preface

of protons requires high proton energies to overcome it. The other possibility is the photodisintegration of neutron-rich isotopes.

Historically, the term *p process* referred to the reactions responsible for the creation of proton-rich nuclei between selenium and mercury. Today *p process* is the generic term for the ensemble of nucleosynthesis mechanisms where proton-rich nuclei are produced. In environments with a high proton density, it is possible for protons to surpass the Coulomb wall and be captured by a nucleus. By capturing protons, the masses move away from the valley of stability until the  $\beta$ -decay rates of the isotopes are bigger than the proton capture reaction rates or it is energetically not possible to accumulate more protons. The fast proton-capture reactions are called *rp process* [7, 17, 18, 19]. It is possible that isotopes undergo a (n,p) reaction, which is called *pn process* and allows to accelerate the production of heavy elements. The needed neutrons for those reactions can be produced in the  $\nu p$  process: In proton-rich environments it is possible that an antineutrino and a proton react to a positron and a neutron [20].

The heavier the element, the more dominant are the photodesintegration reactions on the s and r process seeds over the (p, $\gamma$ ) reactions. The underlying reactions are ( $\gamma,\alpha$ ), ( $\gamma,n$ ) and ( $\gamma,p$ ), hence it is also referred to as the  $\gamma$  process.

If the nucleosynthesis reaction is induced by neutrinos, it is called a  $\nu\gamma$  process. Those can be found in core-collapse supernovae [21].

The complexity of these various nucleosynthesis mechanisms is apparent and therefore it is clear, how much even small uncertainty factors in the network calculation, i.e. reaction rates or half-lives, can affect the results. Adapting the theories to reproduce the empirical observations is relying on the measurement of those variables in the laboratories with sophisticated experiments.

## 1.3 Nuclear Reactions in the Laboratory

While some creation and destruction rates can be measured directly via inbeam or activation experiments, others can not. This is especially the case for short-lived isotopes. Because of their radioactive nature they are not suitable for target production and thus to be irradiated or used in inbeam experiments. This makes it challenging to acquire the needed reaction rates with the needed precision, and other than the direct approaches have to be considered.

### 1.3.1 Reactions in Inverse Kinematics

One possibility to overcome this problem is to exchange the role of target and the projectile. A radioactive beam can be produced in experimental facilities. Usually it takes the freshly produced ion less than seconds between the extraction from the ion source and the arrival at the experimental setup. Using fragmentation processes in the beamline the desired radioactive beam can be delivered to the target, allowing to utilise isotopes with half-lives down to the order of microseconds, far off the stability.

#### 1.3.1.1 Limitations of Experimental Approaches

It is often necessary to modify the experimentally determined rates for the comparison to those in stellar plasmas. Due to the extreme conditions within the hot and dense plasma of a star the excited states of isotopes are populated and in thermal equilibrium with the ground states. The destruction rates of excited states can be several orders of magnitude different than the one of the corresponding ground states. For the isotope  $^{152}\text{Eu}$ , calculations show a difference in the  $\beta^-$ -decay rate of six orders of magnitude for temperatures between 0.5 and  $5 \times 10^8$  K, up to four orders of magnitude in the  $\beta^+$ -decay and electron-capture rates, respectively (see figure 1.4).

Contrary to the ground states, it is not possible to access the excited states of an isotope and use them as target or beam material in reactions, since they decay immediately. Therefore, to gain valuable information, other paths have to be considered. In this work, a method to measure the  $\beta^+$ -decay and electron-capture rates of  $^{152}\text{Eu}$  with an inverse substitute reaction is tested for the first time.

### 1.3.2 The (p,n) Reaction as a Probe of the Beta-Decay Strength

While at the first glimpse it seems odd to substitute a electro-weak with a strong interaction, there is a proportionality between the Gamow-Teller strength distribution  $B(GT)$  and (p,n) reaction cross-sections at low-momentum transfers. Before justifying this proposition, (p,n) reactions and Gamow-Teller transitions will be briefly discussed.

#### 1.3.2.1 Charge-Exchange Reactions

A charge-exchange reaction is characterized by the transition of one unit of charge between the projectile and the target. One possible charge exchange reaction is the (p,n) reaction. The sketch in figure 1.6 shows the basic mechanism of this reaction. Moderated by an  $\pi^+$ -meson the projectile isotope  $X$  exchanges a proton with a neutron from the target isotope  $Y$ . This leads to the creation of two new chemical elements with the same mass but a charge changed by one unit. In the  $^{152}\text{Sm}(p,n)^{152}\text{Eu}$  reaction the consequence is forming  $^{152}\text{Eu}$  from  $^{152}\text{Sm}$ .

The (p,n) reaction is mediated by the strong nuclear force and exchanged via a  $\pi$ -meson. Since the mass of the  $\pi$ -meson ( $140 \text{ MeV}/c^2$ ) is relatively low compared to the mass of protons and neutrons ( $\approx 1 \text{ GeV}/c^2$ ), (p,n) reactions allow to study reactions with a small momentum transfer at  $\vec{q} \approx 0$ . Reactions with a small momentum transfer are related to a scattering angle in the center-of-mass system around  $\theta_{CM} \approx 0^\circ$ . The second advantage the (p,n) reactions offer the experimentalist results from the low mass of the  $\pi$ -meson. It mediates from great distances on nuclear scales and is therefore very suitable for probing nucleon-nucleon reactions [4].

Also, the  $\pi$ -meson can access different nuclear-spin excitations. This makes it a powerful tool to access properties of the nucleus, which are not accessible by other interactions.

#### 1.3.2.2 Gamow-Teller and Fermi Transitions

Both, the Gamow-Teller ( $GT$ ) and the Fermi ( $F$ ) transition, describe a  $\beta$ -decay. The difference is found in the spin vector of the emitted (anti-) electron and (anti-) neutrino, which are both spin  $1/2$  objects. In the  $GT$  transition, the spin vectors are parallel whereas for the Fermi transition they are anti-parallel. Commonly, the Gamow-Teller transition is considered as an extension to Fermis theories. While the baryon and

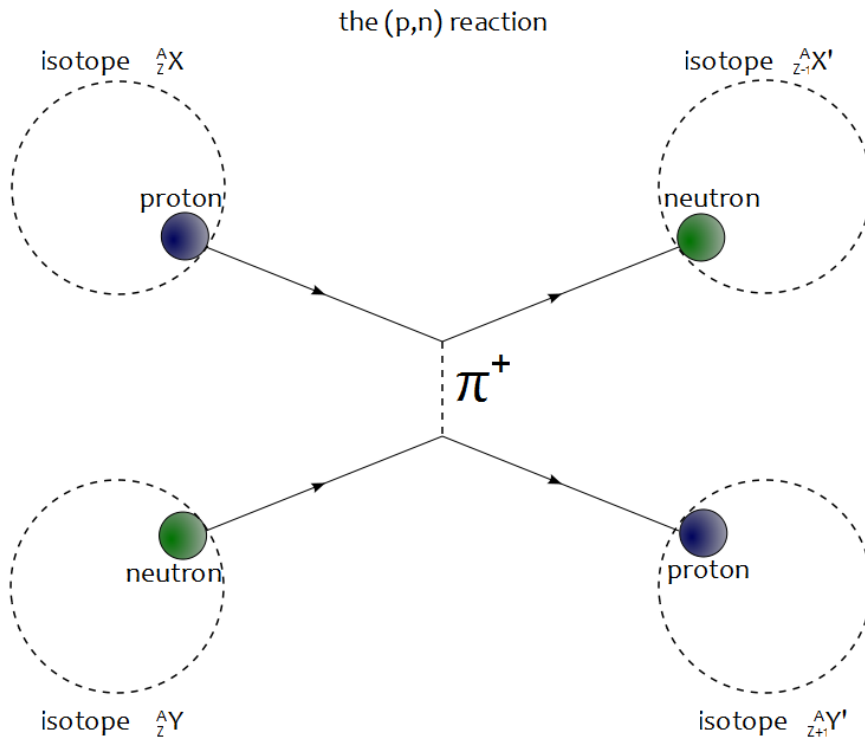


**Figure 1.6** – Principle mechanisms of a (p,n) reaction. Two nuclei undergo a (p,n) reaction which is transmitted by an  $\pi^+$ -meson. The projectile isotope  $X$  exchanges a proton with a neutron from the target isotope  $Y$ . This leads to the formation of two new isotopes with a different proton number  $Z$ , therefore a change in the chemical element while maintaining the atomic mass  $A$ .

lepton number are conserved during the  $\beta$ -decay, this is not the case for the parity, which can be violated under reactions mediated by the weak force [22]. While nuclear transitions are symmetric under parity, weak interactions depend on the chirality. This was not considered by Fermi. Gamow and Teller added the relevant matrix elements and defined the Gamow-Teller transitions.

In the Fermi decay the iso-spin of the isotope can be changed during the decay, while the spin can not. This transition leads to the so-called isobaric analog state (*IAS*). The spin-change is described by the  $\vec{\tau}$ -operator, which de- or increases the iso-spin number by one unit. The  $\vec{\tau}$ -operator is also involved in the charge exchange reaction, where it comes into play when the reactions contain an iso-spin but no spin-flip.

In contrast, the Gamow-Teller transition involves a iso-spin and a spin-flip. Therefore, the spin of the parent nucleus can change by one unit or remain unchanged, but unlike in the fermi decay, the parent nucleus can not maintain the spin of 0. The responsible

## 1. Preface

operators for an Gamow-Teller transition are the  $\vec{\sigma}\vec{\tau}$ -operators. In a charge exchange reaction with a spin-flip involved, those operators are also involved. For a graphical explanation see figure 1.7.

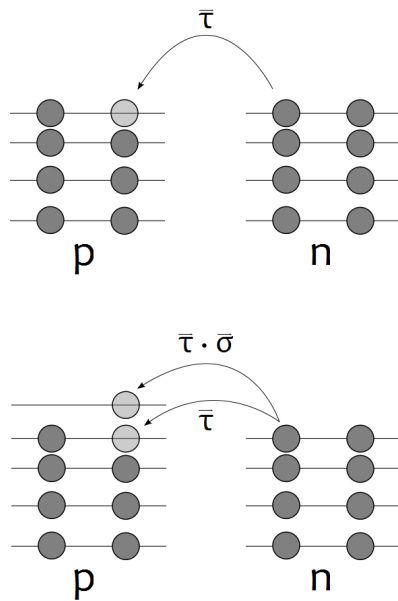


**Figure 1.7** – Gamow-Teller, mediated by  $\vec{\sigma}\vec{\tau}$ -operators, and Fermi transitions mediated by the  $\vec{\tau}$ -operator, respectively, in a single particle model. The Gamow-Teller transition does include a possible spin flip, while the Fermi transition does not.

The spin-flip also allows the daughter nucleus to be in an excited state. This is a significant difference to the Fermi transition.

A  $\beta$ -decay is a mixture of Fermi and Gamow-Teller transitions. In astrophysical scenarios, when electron captures are favored, Gamow-Teller transitions are dominating. This also has an impact on decay rates due to the equilibrium of excited and ground states (see 1.2.3 and 1.3.1.1). Therefore, the Gamow-Teller strength distribution  $B(\text{GT})$  is an important ingredient for modeling nucleosynthesis.

### 1.3.2.3 Similarity between B(GT) and (p,n) Reactions

As pointed out in the previous section, the (p,n) reaction and the Gamow-Teller transition share the matrix elements of the  $\vec{\sigma}\vec{\tau}$ -operators. The matrix elements for Fermi and Gamow-Teller transitions are:

$$B(F, i \rightarrow f) = | \langle f | T_- | i \rangle |^2 \quad (1.13)$$

and

$$B(GT, i \rightarrow f) = \sum \mu | \langle f | \beta_{-(\mu)} | i \rangle |^2 \quad (1.14)$$

respectively.  $B(X, i \rightarrow f)$  is the reduced transition strength of Fermi or Gamow-Teller transitions,  $T_-$  and  $\beta_{-(\mu)}$  the operators for isospin-flip and isospin-spin-flip.

Those are the matrix elements existing also in the charge-exchange cross sections. Using the Born-approximation for distorted waves and the nucleus-nucleus interaction theory under forward-scattering, one gets

$$\frac{d\sigma}{d\theta}(q \approx 0) = \left( \frac{\mu}{\pi\hbar^2} \right)^2 \frac{k_f}{k_i} N_\tau |J_\tau^{NN}|^2 B(F, i \rightarrow f) \quad (1.15)$$

for the Fermi transitions, and

$$\frac{d\sigma}{d\theta}(q \approx 0) = \left( \frac{\mu}{\pi\hbar^2} \right)^2 \frac{k_f}{k_i} N_{\sigma\tau} |J_{\sigma\tau}^{NN}|^2 B(GT, i \rightarrow f) \quad (1.16)$$

for the Gamow-Teller transition, respectively. The reduced mass is denoted as  $\mu$ , while  $k_i$  is the kinematic factor for the initial and  $k_f$  final plane wave,  $N$  is a special distortion factor for the distorted waves and  $J^{NN}$  indicates the volume integral of the bare central part of the nucleon-nucleon reaction.

Examining the matrix elements, one finds that they include the reduced transition strength  $B(X, i \rightarrow f)$ . Therefore, the measurement of the (p,n) reaction cross section under  $\theta_{cm} \approx 0^\circ$  scattering is directly linked to Fermi and Gamow-Teller transitions [23, 24, 25].

This makes the (p,n) reaction a very powerful and promising tool for astrophysical motivated investigations of nuclear reactions. In combination with the time reversed reaction, which allows to scatter from the daughter nucleus into a excited state of the parent isotope.





# 2

## The Experimental Method

### 2.1 Basics

The  $^{152}\text{Sm}(p,n)^{152}\text{Eu}$  reaction experiment (internally called *s405*) was performed at the GSI facility (see chapter 3.1) in October of 2011. The goal was to verify the technique of populating excitation levels of  $^{152}\text{Eu}$  via the charge-exchange reaction and reconstruct the reaction kinematics. It was carried out in inverse kinematics, transferring the actual performed reaction to  $p(^{152}\text{Sm}, ^{152}\text{Eu})n$ . If successfully proven, this method allows to study those transitions in further experiments with radioactive beams, for example at the upcoming FAIR facility and the R<sup>3</sup>B setup (see 6.2.1). Table 2.1 gives an overview of the basic experimental details.

## 2. The Experimental Method

<b>s405 - experimental details</b>	
beam isotope	$^{152}_{62}\text{Sm}$
ions per spill	$5\text{-}7 \times 10^5$
beam energy	300A MeV
studied reaction	$p(^{152}_{62}\text{Sm}, ^{152}_{63}\text{Eu})n$
$^{152}_{63}\text{Eu}$ excitation level energies [keV]	79/158/249
duration $\text{CH}_2$ -target runs	22 hours
duration <i>carbon</i> -target runs	18 hours
duration <i>no</i> -target runs	8 hours
location	cave C at GSI
date	October 2011

**Table 2.1** – The important details of the performed s405 experiment. The different durations for physics ( $\text{CH}_2$  target) and background (carbon and no-target) runs are shown and add up to about 48 hours of usable recorded beam time.

The experiment was focused on the measurement of low-energy neutrons, which carry information of the reaction kinematics of the daughter nucleus. The upper graphic in figure 2.1 shows the correlation between the emission angle in the center of mass system ( $\Theta_{\text{cm}}$ ) and the laboratory system ( $\Theta_{\text{lab}}$ ) in a non-relativistic Galilean picture.

In the reaction  $p(^{152}\text{Sm}, ^{152}\text{Eu})n$  the  $^{152}\text{Sm}$  isotope exchanges a pion with a target proton. The reaction product is  $^{152}\text{Eu}$ , which can be emitted in an excited state. The energy of the emitted neutron depends on the emission angle and on the excitation energy of the  $^{152}\text{Eu}$ . A relativistic simulation of the reaction kinematics was performed (code by John O'Donnell). In figure 2.1 on the top the result of this simulation, the kinetic energy of the neutron as a function of the emission angle  $\Theta_{\text{lab}}$  for 300A MeV  $^{152}\text{Sm}$  beam is shown. The three different dotted lines shown at the bottom of figure 2.1 correspond to three accessible excitation states of  $^{152}\text{Eu}$  at 79, 158 or 249 keV.

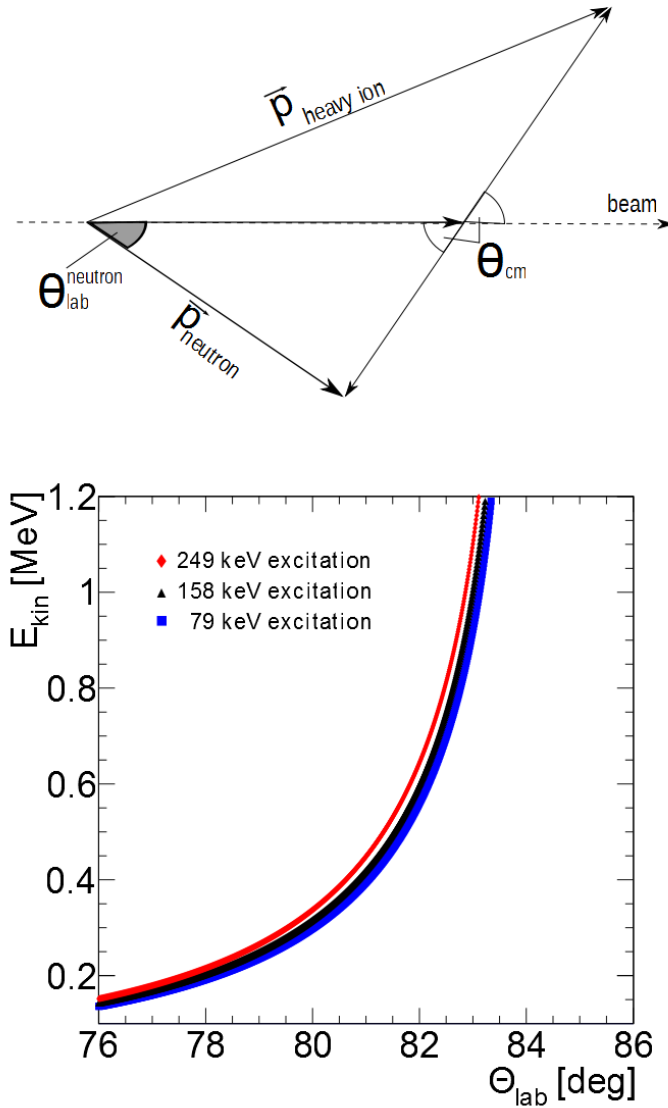


**Figure 2.1** – The upper part of the figure shows the correlation of the angle in the center of mass ( $\theta_{cm}$ ) and the laboratory system ( $\theta_{lab}$ ) in a purely Galilean picture. A  $\Theta_{cm}$  of only a few degrees, as expected at low-momentum transfers, is proportional to huge  $\Theta_{lab}$ . With increasing  $E_{kin}^{neutron}$  the  $\Theta_{lab}$  increases, too. On the bottom the result of the kinetic neutron energy as a function of  $\Theta_{lab}$  is shown. The x-axis is zoomed into the area in which LENA was positioned. The three different symbols represent the three different possible excitation levels of the  $^{152}\text{Eu}$ .

## 2. The Experimental Method

### General Requirements on a Neutron Detector in s405

A characteristic of the discussed kinematics of (p,n) reactions with a low-momentum transfer is the emission angle  $\Theta_{\text{lab}}$  of the neutrons. Bigger emission angles are highly correlated with the  $E_{\text{kin}}$  of the emitted neutrons.

This confronts the experimental researcher with the need of a flexible detector: depending on the individual reaction kinematics the detector has to be positioned in varying angles close to the target (see figure 2.1). In addition the reconstruction of the neutron kinematics is highly dependent on the designated detector position as well as the point of interaction within the individual detector volume.

Therefore a suitable detector has to combine the flexibility with a sufficient granularity and time resolution. Only then a reliable determination of the time and  $E_{\text{kin}}^{\text{neutron}}$  can be assumed. Great demands are made on an adequate tool. The detector and its characteristics have to be known in detail to reconstruct the reaction kinematics in sufficient detail.

## 2.2 The Low-Energy Neutron detector Array LENA

To endorse the LAND/R<sup>3</sup>B setup with a detector capable of measuring low-energy neutrons emitted under great angles, a new detector was developed at ATOMKI Debrecen [26] in cooperation with the GSI Helmholtzzentrum and the Goethe Universität Frankfurt am Main.

To provide a good angular and time resolution, the uncomplicated adjustment to the reaction-dependent position as well as high efficiency and low costs, organic plastic scintillator bars were chosen as detector material. Those organic scintillation detectors are a well known and easy-to-handle type of detectors, as various likewise detectors were created and used in the LAND/R<sup>3</sup>B setup.

The LENA prototype consisted of fifteen individual detector bars, put in three arrays with five bars each, while for future applications the total number of paddles may be upgraded. Each paddle is made of the polyvinyltoluene EJ-200 in the dimensions of 1000×45×10 mm<sup>3</sup>. The emission peak of this material is found around  $\lambda \approx 425$  nm. Together with an PMT (PhotoMultiplierTube) on each end of the paddle the detector provides a time resolution below 1 ns. Silicon grease of a high viscosity was used to improve the transport of light from the organic scintillation material to the PMT. Each paddle is wrapped with a multilayer polycarbonate reflector foil (3M VM2000), followed by a lightproof wrapping with black tape. Figure 2.2 shows the two possible alignments of each paddle in direction of the target. Version (a) was used during s405.

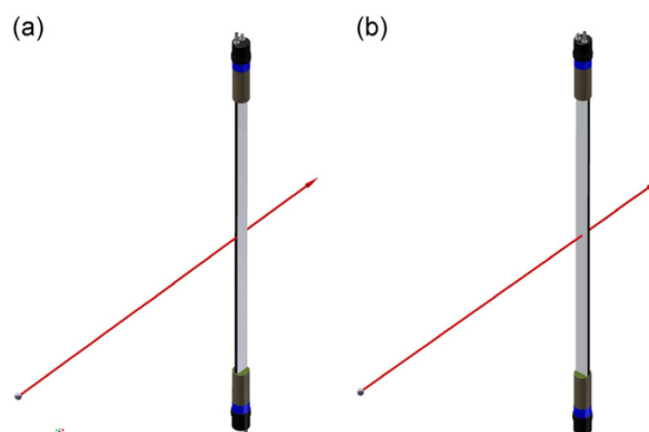


**Figure 2.2** – Two possible alignments of the individual LENA bars. In option (a) the narrow side of the individual paddle faces the neutron emission point, while in (b) the broad side does. For the s405 experiment, the alignment version (a) was chosen. Image by courtesy of [27].

## 2. The Experimental Method

### 2.2.1 Operating Mode of a Scintillation Detector

The most likely interaction of neutrons between 1 keV und 10 MeV with the detector material is elastic scattering. When the scattering occurs on protons between 0 and 100 % of the neutron energy is transferred to the proton, whose energy is in partly transferred into scintillation light.

Since different ionizing particles interact differently with the material, the light yield varies for different particles, traversing the scintillation detector. The carbon within the material can be neglected. If a neutron scatters on the carbon atoms, less energy is transferred and significantly less light is produced compared to the interaction between a neutron and a proton.

The light-transportation within the scintillator material can be described with the following equation, taking reflection and absorption of the light into account:

$$I(x) = I_0 \cdot e^{-\lambda \cdot x} \quad (2.1)$$

where  $x$  is the path length,  $\lambda$  the inverse of the optical light attenuation and  $I_0$  the light intensity, which is proportional to the deposited energy. As mentioned before, one PMT is attached on each end of the detector bar. Thus, two independent measurements of time and energy are performed. With  $I \propto E$ , and  $e_1$  and  $e_2$  are the energies in both PMTs, 2.1 can be written as

$$e_1 \cdot e_2 = E_0^2 \cdot e^{-\lambda \cdot (x_1 + x_2)} = E_0^2 \cdot e^{-\lambda \cdot L} \quad (2.2)$$

Considering that  $e^{-\lambda(x_1+x_2)}$  is a material-dependent constant and the length of the bar  $L$  is fixed, we find the proportionality for the deposited energy:

$$E_0 \propto \sqrt{e_1 \cdot e_2} \quad (2.3)$$

The neutron scatters on a proton, whose energy is measured as  $E_0$ .  $E_0$  depends on different reaction variables, like the scattering angle, and therefore the measured  $E_0$  is only an upper limit of the neutron energy. Thus, the measurement of the neutron energy is not possible on the light output.

Better suited for gathering the kinematic energy of the neutron is the time-of-flight measurement. With the time measurement using both PMTs, one is able to calculate the position of the interaction of the neutron within the detector bar. This is indis-

## 2.2 The Low-Energy Neutron detector Array LENA

pensable, because the flight path depends on the position inside the detector. The time-of-flight and the kinetic energy of the neutron are connected for the classical case as

$$E_{\text{kin}}^{\text{neutron}} = \frac{1}{2} \cdot m_n \cdot \left( \frac{s}{\Delta t} \right)^2 \quad (2.4)$$

with  $m_n$  the neutron mass,  $s$  the flight path and  $\Delta t$  as the time-of-flight.

For relativistic neutrons, the corresponding relationship is given as

$$E_{\text{kin}}^{\text{neutron}} = \left( \frac{1}{\sqrt{1 - \left(\frac{v}{c}\right)^2}} - 1 \right) mc^2 \quad (2.5)$$

or simplified to

$$E_{\text{kin}}^{\text{neutron}} = (\gamma - 1)mc^2 \quad (2.6)$$

with the speed-of-light  $c$ .

The position of the interaction within a single scintillator bar can be calculated from the measured times with the first order approximation

$$x = c' \cdot \frac{\Delta t_{\text{PMT}}}{2} \quad (2.7)$$

where  $x$  is the position,  $\Delta t_{\text{PMT}}$  the time difference between the two PMTs on each bar, and  $c'$  the material specific speed-of-light in the scintillator bar.

Alternately the position can be derived from the ratio of the deposited energies in the PMTs.

$$\frac{e_1}{e_2} = e^{-2\lambda} \quad (2.8)$$

with  $e_1$  and  $e_2$  as the energy as measured in the PMTs,  $\lambda$  the attenuation-length of the detector material and  $x$  as the point of interaction. This can be transposed to:

$$x = \left( \frac{\ln(e_1) - \ln(e_2)}{-2\lambda} \right) \quad (2.9)$$

The middle of the bar is defined as  $x = 0$ .

## 2. The Experimental Method

### 2.2.2 Characteristics and Testing

Prototypes of the Low-Energy Neutron detector Array have been tested with  $\gamma$ -rays from radioactive sources as well as neutron beams at the LANL facility. Those measurements were compared to Monte-Carlo simulations, performed with GEANT3 [28]. The testing and simulation were performed by Christoph Langer et al. For a detailed review of the testing and the results see [29]. The results are in good agreement with a measurement of a similar detector prototype done in Dresden [30].

The determined parameters and characteristics of the individual LENA paddles are summarized in table 2.2.

<b>LENA - characteristics</b>	
material	Polyvinyltolulene EJ-200
dimensions per active volume [mm <sup>3</sup> ]	1000 × 10 × 45
$c' \left[ \frac{\text{cm}}{\text{ns}} \right]$	$15.5 \pm 0.1$
$\Delta t$ [ns]	$0.87 \pm 0.1$
$\Delta x$ [cm]	$\approx 6$
efficiency in the energy-range of 200 - 600 keV	$19 \pm 1 \%$
$\lambda$ [cm <sup>-1</sup> ]	$0.0100 \pm 0.0003$

**Table 2.2** – Overview over the most important specifications of one LENA bar. Data from [29].

#### Suitability for s405

The requirements for a detector suitable for using in the  $^{152}\text{Sm}(p,n)^{152}\text{Eu}$  experiment as defined in section 2.1 were met by the tested LENA prototype. It provides the flexibility and a sufficient time resolution for a precise time-of-flight measurement. Therefore it was used in the s405 experiment to measure the essential low-energy neutrons originating from the charge-exchange reactions.



### 2.2.3 LENA in s405

The finalized setup of the detector array in s405 is the answer to the needs derived from the kinematic calculations. Since the expected neutrons have kinetic energies below 1 MeV, amplifiers were used on the paddles 1-7 and 11-15.

The used prototype of LENA consists of fifteen individual detector volumes arranged in three arrays with five detector bars each. Within the holding structure the paddles were rotated to be face the target with the narrow side. The distance of roughly 5 cm between the individual bars was chosen to minimize neutrons scattering from one bar into the neighboring one (the so called *cross talk*).

The three arrays were positioned vertically on the left and the right of and horizontally above the target in angles of around 80 degrees  $\Theta_{\text{lab}}$  and in 100 cm distance, while every individual detector bar has slightly different position parameters. The exact positions are determined during the analysis process and are shown in the table 4.3 in the corresponding chapter of this work. In figure 2.3 a picture of the actual setup is shown on the left. The right shows the internal numbering of LENA bars.

During the experiment, the PMTs were shielded from the magnetic field of the large dipole magnet using  $\mu$ -metal. To have consistency, all measurements and calibration runs were done with the magnetic field turned on.

## 2. The Experimental Method

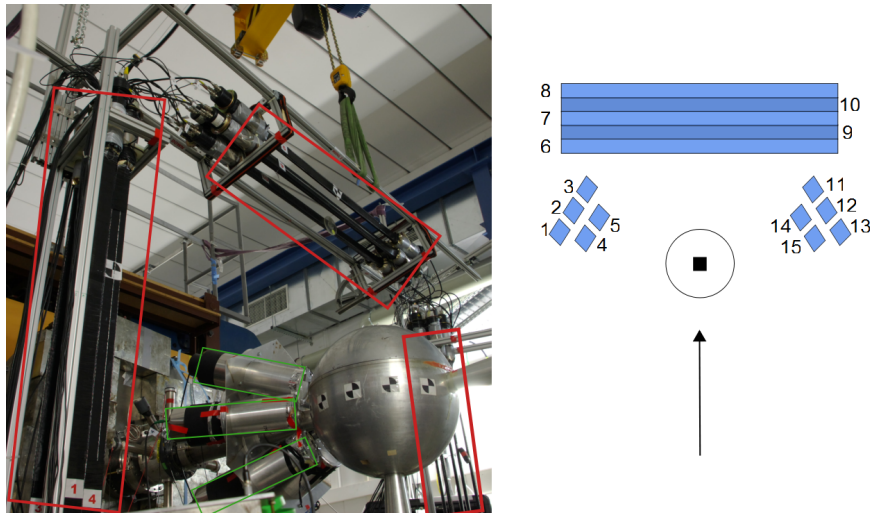


**Figure 2.3** – The left photograph shows LENA during the s405 experiment. The fifteen LENA bars are indicated by the red frame. The sphere in the center of the picture contains the targets, the six aluminum cylinders (green frame) the six  $\text{LaBr}_3\text{:Ce}$  crystals. On the right a top view drawing of the numbering and orientation in respect to the target of the fifteen individual LENA bars is shown, the arrow indicates the beam direction. The position of the three arrays corresponds to the ones in the photograph.

# 3

## The Infrastructure

### 3.1 The LAND/R<sup>3</sup>B Setup at the GSI Helmholtzzentrum

The experiment was performed at the GSI Helmholtzzentrum für Schwerionenforschung GmbH in Darmstadt, Germany (see figure 3.3). Using the combination of heavy duty ion sources, linear accelerator structures and a synchrotron, many different experiments are conducted at GSI.

The first step to produce a stable or radioactive beam for a heavy-ion collision or fixed target experiment is the extraction of ions using a high-current ion source. The first acceleration in the GSI facility is taking place via the Universal Linear Accelerator (*UNILAC*). In a sequence of various steps, including different acceleration methods like Radio Frequency Quadrupoles (*RFQs*), Interdigital H-type structures and Alvarez accelerators, the beam is accelerated to the desired speed. Finally, after around 120 meters, the ions reach a speed of up to 11.4 A MeV. From this point a 130 meter transfer, including a stripper foil, transports the ion beam to the SchwerionenSynchrotron (**SIS 18**). The SIS 18 is a synchrotron with the circumference of 217 meters and about 35 meters in radius. With the maximum bending power of 18 Tm the extraction

### 3. The Infrastructure

energy of the SIS 18 can reach up to 4.5 GeV for a pure proton beam, corresponding to 98.5 % speed-of-light. There are two different extraction modes available: The fast mode with a spill length of 500 ms and the slow extraction with a length of 10 s. In the experiment described in this thesis, the slow extraction mode was used. The beam in s405 was a stable  $^{152}\text{Sm}$  beam with an energy of 300 A MeV and about  $5\text{-}7 \times 10^5$  ions per spill.

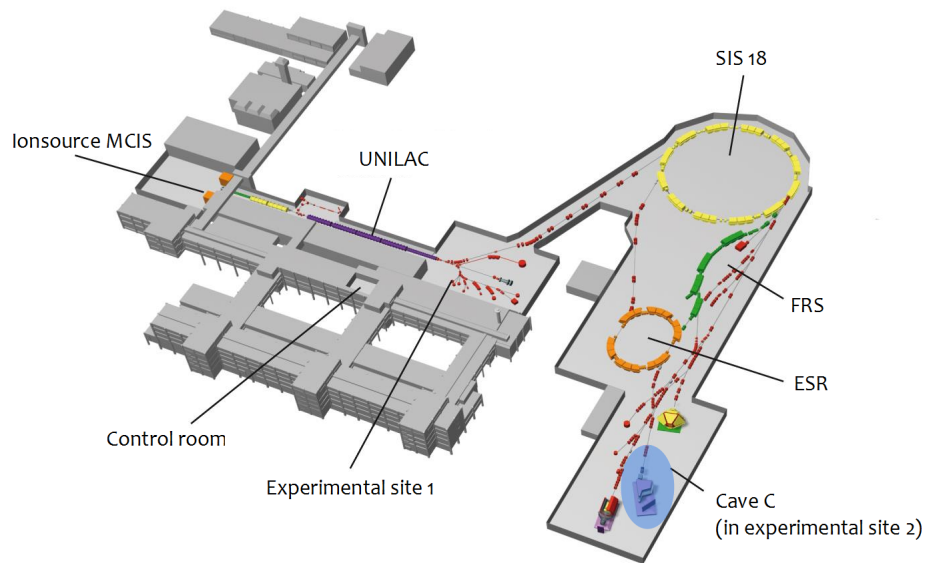


**Figure 3.1** – Schematic drawing of the GSI Helmholtzzentrum für Schwerionenforschung GmbH near Darmstadt. While the gray-scaled sketches represent the building on the GSI site, the colored lines describe the composition of the beam line. The ions are extracted at the ion sources (*MUCIS*), from where the beam is accelerated in first the *UNILAC* part with different accelerator structures. It can be extracted or injected in the *SIS 18* synchrotron. From there a fragment-separator unit (*FRS*) can be used to break the primary isotopes into (radioactive) fragments. Finally, the primary beam or the fragments are lead into the target hall and, in the case of the s405 experiment, into the *LAND/R<sup>3</sup>B* setup at Cave C. From [31], modified.

The  $p(^{152}\text{Sm}, ^{152}\text{Eu})n$  reaction experiment was conducted in Cave C at the GSI facility. The in Cave C situated *LAND/R<sup>3</sup>B* setup was equipped with additional detectors specifically for the s405 experiment. Figure 3.2 shows the *LAND/R<sup>3</sup>B* setup in the s405 configuration.

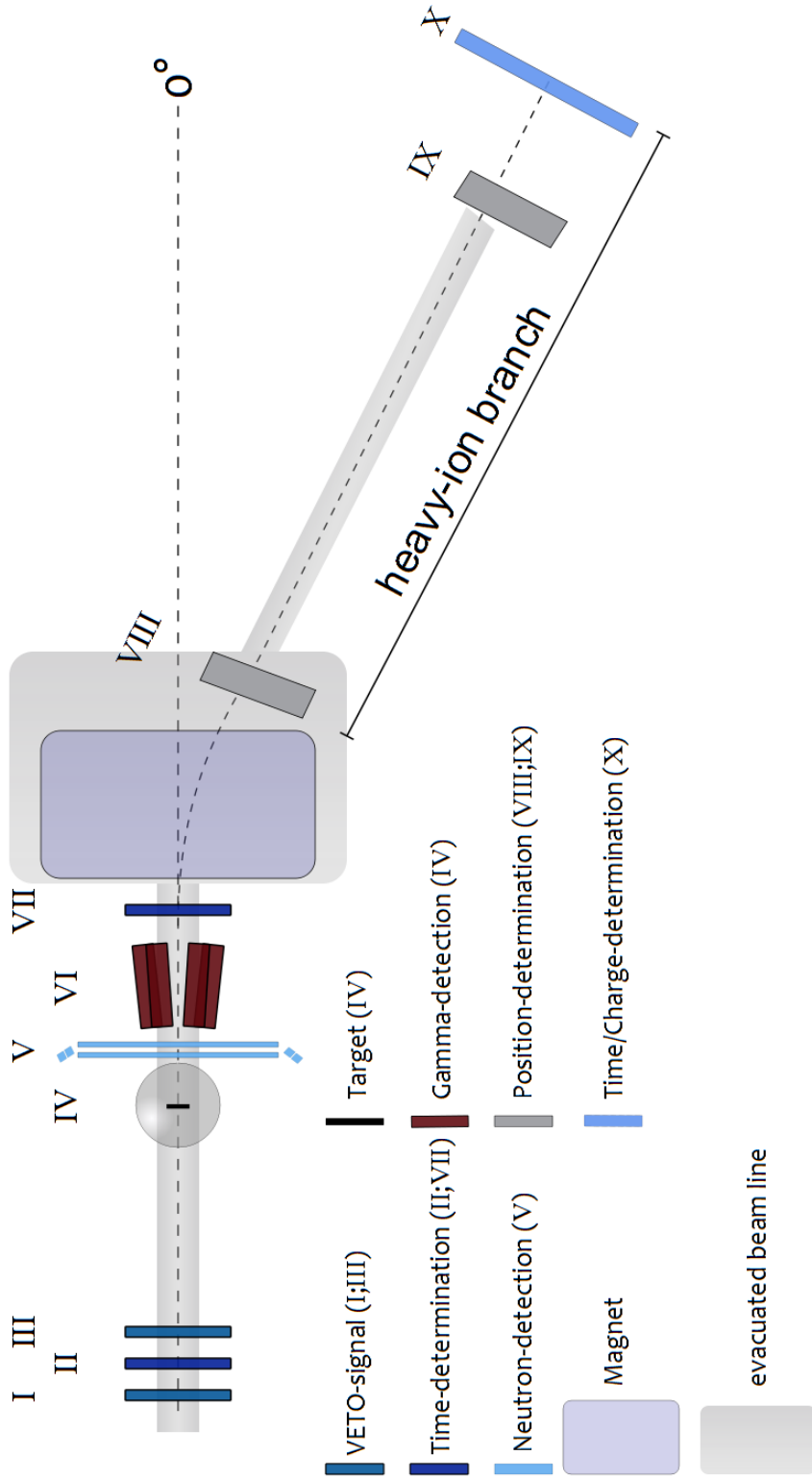


**Figure 3.2** – The s405 experimental setup. The beam enters the setup from the left and has to pass through two veto and one timing detector before reaching the target. After the target the beam particles enter the ALADIN dipole magnet, where they are deflected into the so called heavy-ion (or fragment) branch, the specific angle depending on their mass-to-charge ratio, while neutrons pass the dipole magnet unaffected. (Image not to scale)

## 3.2 Other Detectors used in the s405 Experiment

### 3.2.1 ROLU

The first detector passed by the incoming ion beam is the so called ROLU, which consists of four individual plastic scintillators. The name is an acronym from German RechtsObenLinksUnten (right,top,left,bottom), which is a short description of the detectors basic working principle. The ROLU is used as a VETO detector for the event selection in the data acquisition. It consists of four scintillation paddles, which are arranged at the right, top, left and bottom of the beam. They form a rectangular window around the beam, whose size can be regulated. If a particle passes through the ROLU and leaves energy in the scintillators: the detector delivers a signal (VETO) and this specific event will not be recorded. With the ROLU the beam radius and alignment can be adjusted and controlled.

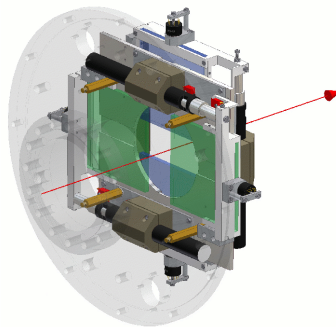


**Figure 3.3** – The ROLU detector as used in the LAND/R<sup>3</sup>B setup during the s405 experiment. The arrow denotes the direction in which the beam passes the detector. The four scintillator paddles create a window in the middle, which can be varied electronically in size from the experimenter and is used to set a cut on the beam quality of the incoming particles [32].

### 3.2.2 POS

In order to provide the starting time for the time-of-flight measurements fast scintillator detectors are used. The so called POS detectors are found on position II and VII in Figure 3.2. The POS detector consists of scintillating material with  $200\ \mu\text{m}$  thickness and an active area of  $2.5 \times 2.5\ \text{cm}^2$ . Four PMTs are attached to light guiding material, which transport the light from the scintillating material to the PMTs. The time resolution of the POS is about 25 ps. This allows exact time-of-flight measurements between the POS and other detectors. A drawing of the POS detector is shown in figure 3.4.

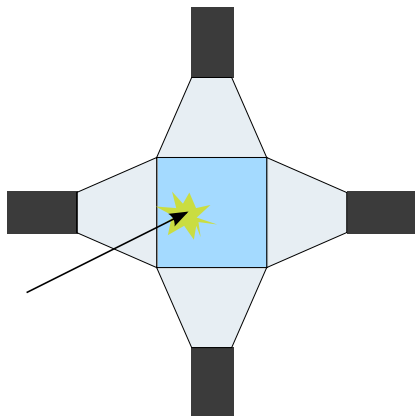


**Figure 3.4** – The POS detector as used in the LAND/R<sup>3</sup>B setup during the s405 experiment. Two of those detectors were used in the experiment. The first one was used to provide the time-of-flight measurement with a starting time information. It is a fast organic scintillation detector with an active area of  $2.5 \times 2.5\ \text{cm}^2$  and four attached Photomultipliertubes. Those are numbered #1 till #4, while odd and even numbers face each other.

### 3. The Infrastructure

#### 3.2.3 LaBr<sub>3</sub>:Ce

Six independent cylindrical (89 mm in diameter by 203 mm radius) cerium doped lanthanum bromide detectors inside an aluminum shielding were especially added for the s405 experiment to the LAND/R<sup>3</sup>B setup and used for  $\gamma$ -detection. The advantages of the LaBr<sub>3</sub>:Ce detectors are the excellent energy resolution of around 3% FWHM at 661.6 keV and the time resolution of less than one nanosecond, depending on the size of the crystal. Large volume LaBr<sub>3</sub>:Ce detectors are capable of providing spectroscopic information in the  $\gamma$ -energy range of a few keV up to 25 MeV. The resolution of the time information can be used to effectively discriminate neutrons. Hamamatsu R10233-100 photo multipliers were used on all of the detectors. All six detectors were mounted in equal distance to each other at an angle of 21 degrees relative to the beam line 30 cm distant to the target [33, 34, 35].



**Figure 3.5** – The picture shows one of the six used LaBr<sub>3</sub>:Ce detectors and the attached photomultiplier. Since the LaBr<sub>3</sub> crystal is toxic and highly hydrophilic, they are contained within a sealed aluminum cylinder. Each detector-crystal has the dimensions of 89 mm in diameter and 203 mm in radius. The LaBr<sub>3</sub>:Ce detectors are used because of their excellent energy and time resolution over a energy-range between a few keV and up to 25 MeV, making them a valuable tool for  $\gamma$ -ray measurements in various experimental setups [36].



#### 3.2.4 GFI

The position measurement behind the ALADIN magnet is provided by the so called GFI detectors. Two GFIs were used in the s405 experiment, one directly after the magnet within the vacuum chamber (position (VIII) in figure 3.2) and a second one just outside the evacuated casing (position (IX), respectively). GFI is a acronym for *Großer Fiber Detektor*, meaning big fiber detector. The name derives from the 475 scintillating fibers of which the active area of each of the detectors consist of. Any of the fibers has a cross section of  $1 \times 1 \text{ mm}^2$  plus cladding. The total active area adds up to a total of  $50 \times 50 \text{ cm}^2$ . A position sensitive PMT is mounted to the 475 fibers. This allows to reconstruct the position-information of passing ions, which is necessary for the reconstruction of the flight path of every ion. The position resolution is better than 1 mm, the efficiency between 89 % and 100 % [37]. The basic design of the GFI detector is shown in figure 3.6.

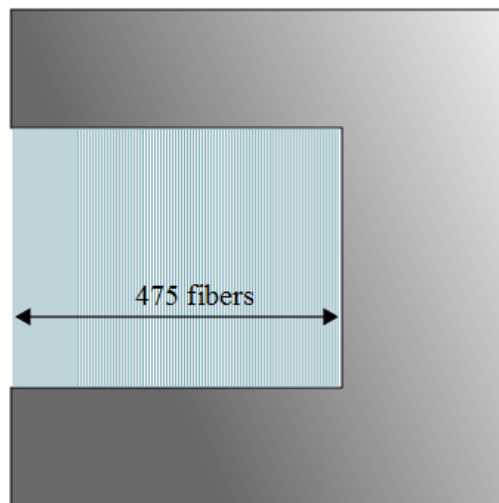


**Figure 3.6** – Basic drawing of one GFI detector. The active area of the detector consist of 475 fibers with a cross section of  $1 \times 1 \text{ mm}^2$  and adds up to a total of  $50 \times 50 \text{ cm}^2$ . Those fibers in combination with a position sensitive photomultiplier allow the reconstruction of the position of passing ions with a resolution of better than 1 mm. The mounting and electronics of the detector are shielded by a metal casing.

### 3. The Infrastructure

#### 3.2.5 TFW

The big time-of-flight wall (TFW) is positioned at the end of the heavy-ion branch. It consists of 32 scintillator paddles, adding up to 64 channels. Each of the 18 horizontal paddles has the dimensions of  $147 \times 10 \times 0.5 \text{ cm}^3$ , the 14 vertical paddles have the dimension  $189 \times 10 \times 0.5 \text{ cm}^3$ . The arrangement is shown in figure 3.7.

The TFW is positioned at the very end of the setup (position X), allowing to measure the total time-of-flight of each incoming ion. Due to the crossed paddle design, the position of the incoming particle can be determined, which is used in the tracking of each beam particle (see chapter 5.2.3.2).

In addition, using the energy loss within the detector paddles, the charge of each ion can be extracted. This mode is especially important in experiments with ions heavier than  $A = 30$ . If the charge of each incoming particle can be resolved with proper accuracy, it is possible to distinguish between the beam particles that did undergo a reaction and those which didn't.

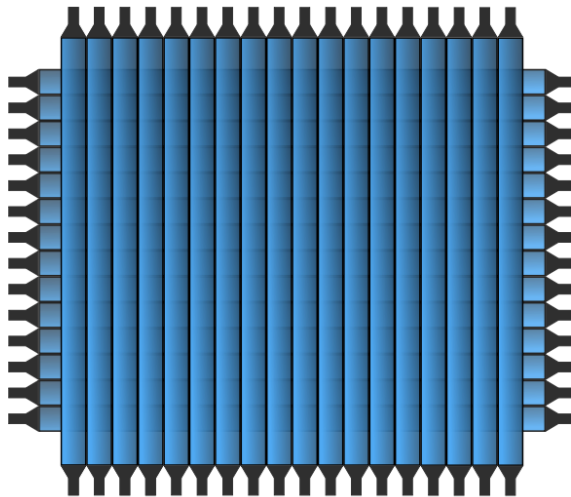


**Figure 3.7** – Simplified depiction of the big time-of-flight wall as used in the LAND/R<sup>3</sup>B setup. It consist of 32 scintillator paddles arranged in two overlapping layers. The horizontal layer is made out of 18 paddles while the vertical consists of 14. The TFW is used for time measurement as well as the determination of the charge of beam particles.

## 3.3 Further Devices in the Beam Line

### 3.3.1 The Target

The targets were mounted on a electrically-operated holding structure, enabling remote change of the target from the outside without breaking the vacuum. The different targets used in the experiment are shown in table 3.1. Apart from the CH<sub>2</sub> target for the (p,n) reaction itself, data were taken with a carbon target as well as without any target at all to subtract the influence of secondary reactions and reactions with the experimental setup itself. The targets were mounted in an angle of 45 degrees relative to the beam direction. This not only increases the effective thickness by roughly 40 %, it also decreases the path of the neutrons through the target material when exiting at high angles.

<b>s405 - Target Details</b>			
target material	thickness [mm]	eff. thickness [mm]	density [ $\frac{\text{g}}{\text{cm}^3}$ ]
polyethylene (CH <sub>2</sub> )	2.31	3.27	0.92
carbon	1	1.43	1.84
no target	-	-	-

**Table 3.1** – Target details for the s405 experiment. Each target was installed in a 45° angle, thus increasing the effective thickness. Two different targets were used in the experiment; a polyethylene target (PE-LD) which was chosen because of its high proton to neutron ratio and a carbon target to measure the influence of the carbon isotopes from the CH<sub>2</sub> target in the reaction between beam and target. In addition, data was taken with no target installed to get information of the interaction of the beam with the setup and subtract this background data from the physical ones.

### 3. The Infrastructure

#### 3.3.2 ALADIN

A centerpiece of the setup is the large dipole magnet ALADIN. It was installed in cave C in 2004. ALADIN is positioned behind the second POS and the  $\text{LaBr}_3\text{:Ce}$  detectors and was evacuated. In the magnetic field of the ALADIN magnet the beam particles are deflected depending on their charge-to-mass ratio and velocity, therefore unreacted and reacted beam particles are separated. Figure 3.8 shows the measured magnetic field.

The individual deflection of the particles due to the magnetic field allows the  $B\rho$  of the particles to be calculated. During the s405 experiment, the front of the magnet was covered with bricks made of paraffin to reduce back-scattering of neutrons into the low-energy neutron detector array.

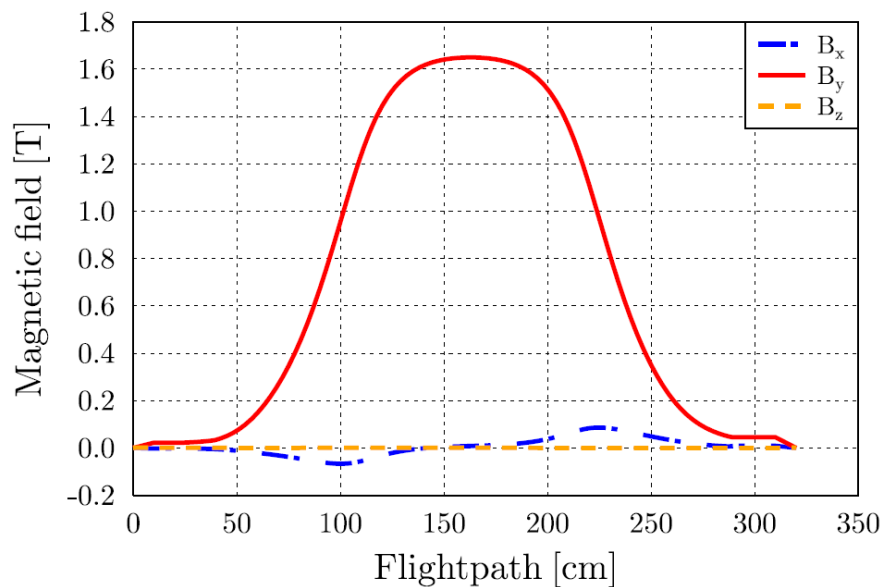


**Figure 3.8** – The magnetic field distribution of the ALADIN magnet was measured using a hall-probe. The gauged field strength inside the magnet along the flight path. The information is also used to calculate the flight path using the tracker software (see chapter 5.2.3.2). Image by courtesy of [27].

# 4

## Data Acquisition and Analysis

### 4.1 Electronics and Software

#### 4.1.1 Data Acquisition and Trigger Patterns

Detectors in a scientific experiment are permanently exposed to a noise signal. Not only in terms of the amount of recorded data it is necessary to suppress noise and lay a focus on more promising signals. Trigger-patterns are a reliable method for gathering data. A trigger signal is defined as a time window, in which specified detectors have to have see signal. Only if this is the case the trigger sends the signal to the data acquisition (*DAQ*) to start recording the current event data. The recording of the data is completed event-wise, allowing to access the individual detector response for each individual recorded event.

If the DAQ is triggered, a signal integral and a time information are recorded for every detector. The pulse coming from the detector is split into two signals.

The energy information, proportional to the amplitude of the signal, is led through passive delays to a Charge to Digital Converter (*QDC*), where, if a signal from the

#### 4. Data Acquisition and Analysis

trigger-module is given, the time integrated current is saved.

The other part of the PMT signal is transferred to a Constant Fraction Discriminator (*CFD*). The information and the path in the electronics it has to cross is called the time branch. The *CFD* module is used to extract a time information from signals with varying amplitudes. It discriminates the potential signal from the noise by using a defined threshold, and it converts it into a logical signal. The incoming signal is split inside the module. Both signals are used separately. One signal is delayed with a fixed time, while the second signal is inverted and added to the first. The zero crossing of the signal defines the trigger for the time measurement. The signal is transmitted to the Time to Digital Converter (*TDC*), and if triggered it is recorded.

The decision if such a master gate is produced by the trigger module is relying on coincidences from different detector systems. The size of the master gate can be modulated by the experimenters. While the master gate is successfully created, no other event is created until the data readout ended. This results in the DAQ dead time.

Different combinations of responding detectors result in different trigger patterns. The patterns are used to downscale recorded events. Since background events are expected to occur in bigger numbers than physical data and use up a huge amount of storage, the events are scaled down. The down-scaling of events is used to suppress the proportionally larger amounts of data. For example, minimum-bias data is more common than in coincidence with a signal in LENA and is suppressed by a factor of 256, thus only every 256th event is recorded. Additionally those patterns are stored for every event, making it possible to apply specific conditions during the analysis. Table 4.1 shows the different trigger patterns (internally called TPat) used during the experiment.

s405 - Trigger Patterns		
TPat [bin]	definition	condition
1	min bias	good beam + ROLU
2	GB + LaBr	good beam + LaBr <sub>3</sub> :Ce detector
4	GB + LANDhi	good beam + LAND-detector
8	GB + TFW	good beam + TFW
16	GB + LENA	good beam + LENA

**Table 4.1** – Trigger patterns used in s405. The number of each TPat represents the bins set in the daq for each event. TPats are implemented to downscale events. In addition different trigger patterns allow in the analysis to distinguish between different reaction conditions during the experiment. While the trigger for GB+LENA is a constraint for measuring the demanded (p,n) reaction, other patterns allow to estimate the background noise from other reactions. A good beam is defined by an event without a VETO but without any other criteria applied.

## 4. Data Acquisition and Analysis

### 4.1.2 The Land02 Framework

The land02 framework is the main software tool to perform substantial parts of the analysis. It is written in C++. The event-wise data acquired during the experiment are unpacked, calibrated and analyzed using the land02 software. Different stages of unpacking, reflecting different stages of the calibration and analysis can be accessed. The available unpacking levels are, from uncalibrated data to the final step:

- **RAW** This level contains raw data without any calibration done. The data delivered in the form of channels for all detectors, as directly provided by the read out electronics.
- **TCAL** In this unpacking level, the time information is transferred to ns and pedestals (compare 4.2.1) are subtracted from the energy information.
- **SYNC** The times of the different subsystems of each detector are synchronized. The energy information in those subsystems are gain matched.
- **DHIT** The components (i.e. all PMTs) of each detector bar, are treated as one, reducing the number of subsystems for each detector. Intrinsic detector coordinates are provided.
- **HIT** All sub-modules of a detector are combined into one single energy, time and multiplicity information. All coordinates are transferred to the external coordinate system of the detector.



## 4.2 Detector Calibration

A lot of the detectors in the LAND/R<sup>3</sup>B setup are used on a regular basis. For those, semi-automatic calibration scripts exist. These scripts use the calibration algorithms efficiently. Nonetheless, the results of the scripted calibration have to be controlled and typically small corrections have to be applied manually by the user. For some other detectors, an automatized calibration is currently not available, therefore these have to be synchronized manually.

### 4.2.1 CLOCK and TCAL

The via a QDC gathered energy signal in the raw level contains so called pedestal: A current is laid on the read-out electronics, when no physics signal is delivered, resulting in a peak in the energy spectra at low channel numbers. It corresponds to measuring zero energy and hence needs to be subtracted from all physics measurements. During the experiment a clock is continuously running, which prompts a signal to the electronics, triggering the energy-branch read-out modules when no physics signal is coming in. This leads to the recording of this sole pedestal. Using the software-based CLOCK routine, those intrinsic pedestals can be isolated, fitted with a gaussian and subtracted from real physics data.

Similar, the so called Time CALibrator (*TCAL*) is sending randomized time signals during beam-breaks into the setup. The provided time interval is recorded in ns in a variable called *tcalt*. This reference time can be plotted against the time information in channels of each detector-channel, allowing to convert channels directly into ns.

### 4.2.2 POS

The calibration of the POS detector is straightforward, since only a time information is used. After conducting the CLOCK, to eliminate pedestals, and TCAL, to get time signals converted into ns, routines, the time signals of the four PMTs are synchronized in respect to each other. This allows to gain a start signal for the time-of-flight measurements. During the experiment, one of the four PMTs failed, so that for the analysis only the opposing PMTs #2 and #4 have been used.

## 4. Data Acquisition and Analysis

### 4.2.3 LaBr<sub>3</sub>:Ce

To calibrate the LaBr<sub>3</sub>:Ce detector, various  $\gamma$ -ray sources with different  $\gamma$ -ray energies were used (see table 4.2) on each of the six modules. Using the resulting spectra, an energy calibration in the form

$$y = m \cdot x + b \quad (4.1)$$

where  $y$  is the actual  $\gamma$ -energy from the source,  $x$  the channel number of the corresponding peak,  $b$  the offset and  $m$  the calibration factor, was performed. For  $x$ , the channel number was obtained via a gaussian fit, with  $\sigma$  as the error margin. Figure 4.1 shows the calibrated spectra for one of the LaBr<sub>3</sub>:Ce modules with different calibration sources applied. The <sup>152</sup>Eu source allows a calibration within the most interesting area between 70 and 500 keV. In addition the intrinsic detector radiation can be seen in the runs with and without any source. This calibration procedure was performed for all six LaBr<sub>3</sub>:Ce crystals. All six detector crystals had different detection thresholds.

LaBr <sub>3</sub> :Ce Calibration		
Source [isotope]	Energy [keV]	Channels [detector 3]
<sup>22</sup> Na	511	366 ± 19
<sup>22</sup> Na	1275	928 ± 14
<sup>60</sup> Co	1173	797 ± 19
<sup>152</sup> Eu	344	244 ± 18

**Table 4.2** – The table contains the energies of the emitted  $\gamma$ -rays of the sources, used to calibrate the energy spectrum of the LaBr<sub>3</sub>:Ce detector.

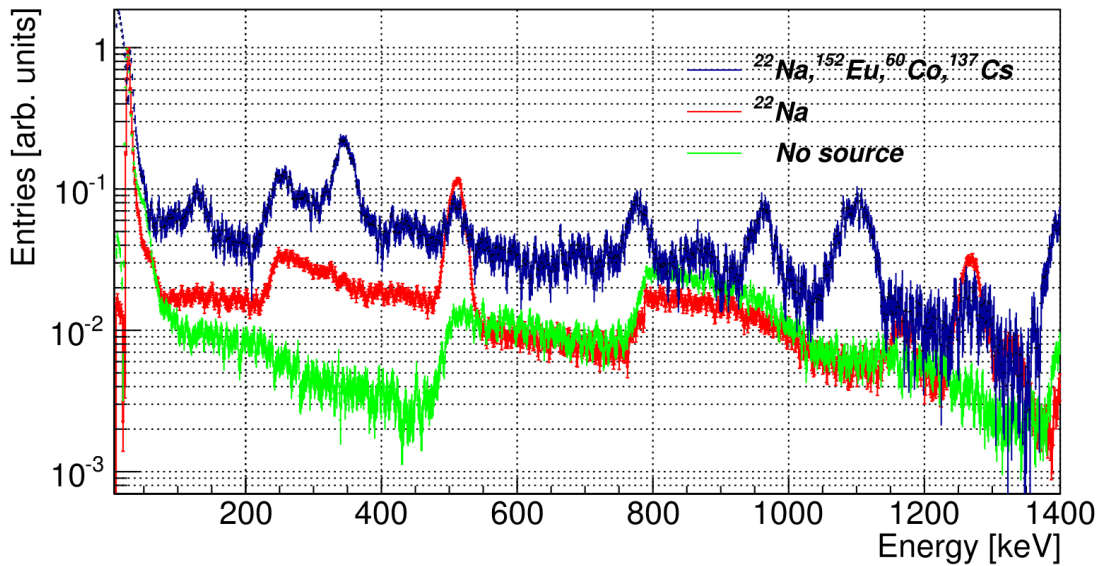


**Figure 4.1** – The plot shows three different energy spectra as a function of the calibrated energy, recorded with the same detector (#3). The green line represents the spectra without any calibration source. The detector intrinsic lines at different energies (5.6, 37.4, 789, 1440 and 1472 keV) can be seen. For the red spectra, a  $^{22}\text{Na}$  source was applied to the detector. For the blue line additionally a  $^{152}\text{Eu}$ , a  $^{137}\text{Cs}$  and a  $^{60}\text{Co}$  source were attached. With the gained information, a correction factor was calculated. While the detector response to  $\gamma$ -rays is not strictly linear, in the important energy range between 70 and 500 keV it is sufficient.

## 4. Data Acquisition and Analysis

### 4.2.4 LENA

The calibration of the Low-Energy Neutron detector Array is divided in two parts: The first is the calibration of the detector itself. This means the calibration of the time and energy information. The second step is the determination of the correct detector position with respect to the target. Both are essential to determine the flight path and emission angles.

#### 4.2.4.1 Calibration of Time and Energy

To perform the CLOCK and TCAL calibrations standardized routines were used. After successfully done, the data can now be unpacked in the TCAL level. Using the TCAL data, the time and energy signals for each PMT on each paddle are synchronized in respect to each other. The data can now be treated in the SYNC level.

For the SYNC level calibration, the PMTs on each paddle are synchronized. To do so, the measured mean time of both PMTs is plotted and corrected. Afterward all paddles are synchronized in respect to each other. The energy information is gain-matched as well. This leads to an analysis level of the data, which allows to gain correct information on time and energy of particles passing through the detector paddle.

For the analysis of the experiment, the LENA data is used in the SYNC level, (D)HIT level is not applied. Since all paddles have an individual geometric position in angle and distance to the target, LENA is treated as fifteen individual detectors. Using the time of the two photomultipliers at each end of the bar, the position of the interaction within the detector bar can be calculated using equation 2.7. Figure 4.2 shows the position of the signal of one LENA paddle during a source run. The source was placed directly on the wrapped bar close to the middle. The positions on the bar were calculated using the formulas 2.7 for  $\text{Position}_{\text{time}}$  and 2.9 for  $\text{Position}_{\text{energy}}$ . The position calculated with the time information is more precise than the position acquired from the rather unreliable energy signal.

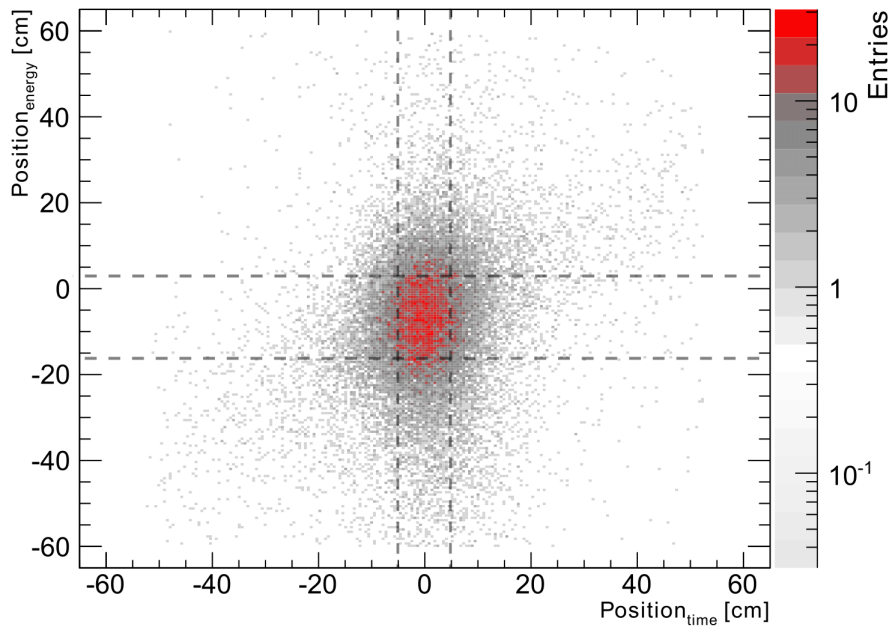


**Figure 4.2** – Position from time vs position from energy (both in cm) measured for the LENA bar #2. A  $^{137}\text{Cs}$  source was applied on the middle of the bar. The position calculated from the time is about 70% more precise than the one from the energy. This is result of the arbitrary energy deposition of the neutrons in the bar. Therefore the time is used to calculate the position.

## 4. Data Acquisition and Analysis

### 4.2.4.2 Position Reconstruction of LENA

As pointed out in chapter 2.1, it is crucial for the reconstruction of the low-energy neutrons to measure their kinetic energy and the emission angle. The position of the detector has to be known as exactly as possible. This was done using the photogrammetry software *Photomodeler* (see reference [38] for more information):

With a calibrated camera photographs were taken from several positions and angles. The detector bars were equipped with several markers. Using the *Photomodeler* software, pointers were set on the photographs, on the markers as well as on various characteristic geometric spots (e.g. edges or similar). The pointers are connected with lines, and pointers on the same places of the detector are cross-referenced between different photographs. After providing the program with the actual measured distance between two of the defined spots, the *Photomodeler* is able to produce an accurate three-dimensional model of the detector setup, including distances between the defined geometric structures. Figure 4.3 shows the visual output, based on the software calculations, of the constructed three-dimensional model of the detector. Using the available data and projecting a plane along the beam axis, one can calculate the angles of each single detector bar relative to the beam line as well as the exact distances to the single detector bars from the target, which is essential to measure the correct energy via the time-of-flight method. The margin of error for the position determined with the *Photomodeler* is assumed to be below 1% and decreases with an increasing number of pictures and reference knots used, which is negligible compared to the uncertainty  $\approx 6$  cm from the position resolution within the LENA bar. The distances and angles for each paddle can be found in table 4.3.

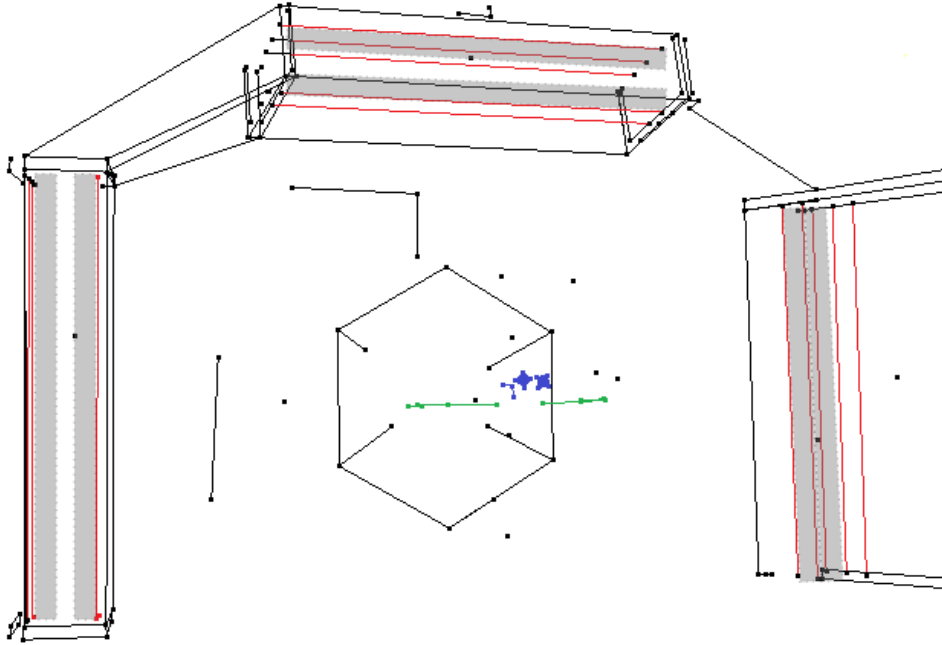


**Figure 4.3** – Three-dimensional model of the s405 setup around the target area with focus on LENA. The points and lines are used to indicate specific structures and intersections during the reconstruction process. The red lines represent the front/back of each of the fifteen LENA paddles, of which six are indicated with the gray areas. The hexagonal shaped in the center is the holding of the  $\text{LaBr}_3\text{:Ce}$  detectors. The green vertical lines mark the outer area of the target sphere, defining the beam plane. The blue squares bordered by this sphere are different targets, which can be brought into the beam.

It has to be noted that the reconstruction angle of the incoming particle is dependent on the position of interaction within the LENA bar. Therefore, the angles relative to the beam line given in table 4.3 are in respect of the height of the beam and thus in the middle of each bar. The angle changes as a function of the point of interaction. This dependence is shown in figure 4.4. It is apparent that the angle and length of the flight path for incoming particles differ for different interaction points within the individual LENA bar.

#### 4. Data Acquisition and Analysis

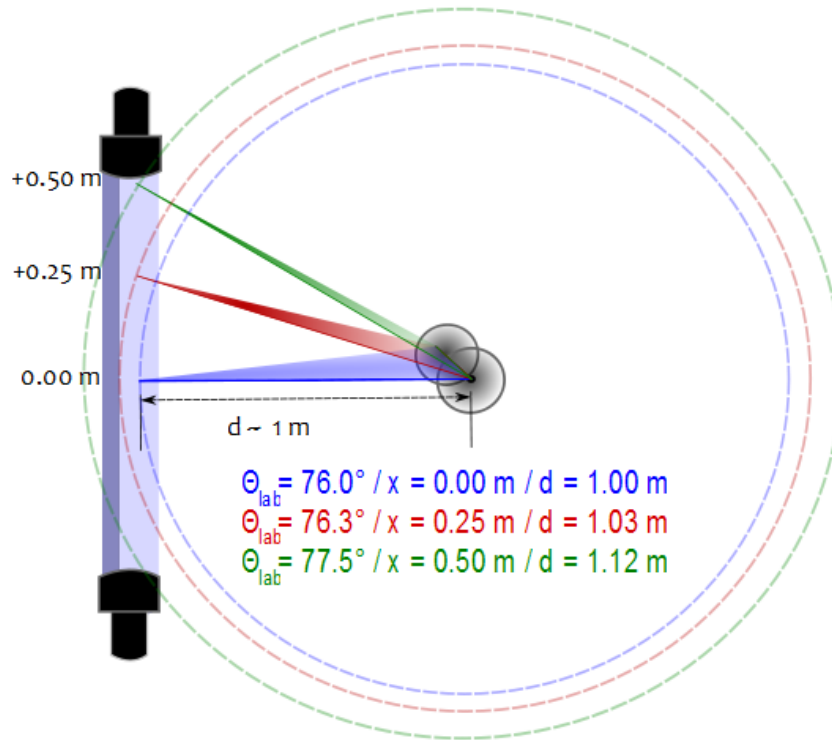


**Figure 4.4** – In this figure, the correlation of the flight path and the emission angle of neutrons from the target is shown. The arrow indicates the beam direction. The more the interaction point on the individual detector bar deviates from the center, the bigger the emission angle and the longer the flight path are. The angle  $\Theta_{lab}$  is the angle between the beam line and the LENA bar,  $x$  the point of interaction in the bar and  $d$  the flight path from the target. The correlation is non-linear, leading to an emphasis of the angles of the middle of the bar.



<b>To target</b>					
module [#]	distance [cm]	angle [°]	module [#]	distance [cm]	angle [°]
1	109.4	81.3	9	77.1	84.7
2	109.3	77.4	10	76.3	79.1
3	109.3	73.6	11	108.4	72.9
4	102.8	80.8	12	108.5	76.9
5	102.7	76.4	13	109.1	80.9
6	83.8	85.5	14	101.6	76.3
7	82.4	80.1	15	102.3	80.4
8	82.4	74.4			

**Table 4.3** – List of the with the Photomodeler determined distances and adjustment angles relative to the beam line for each LENA bar. The angles are given for the middle of the bar. The uncertainties are in the order of 1%. For the numbering and orientation of each bar, see figure 2.3

### 4.2.5 GFI

GFI detectors (compare chapter 3.2) are used to determine the position of the passing beam particles. The position-sensitive PMTs on each GFI provide a position after ALADIN in its internal coordinates ( $u,v$ ) which after the calibration process are transferred to the  $x$ -position in the laboratory frame.

For the calibration a so called sweep run is used: by changing the ALADIN current the beam is steered over the complete active area in  $x$ -direction to illuminate all fibers, thus making it possible to mark the correct position for every fiber in the intrinsic coordinate system of the detector. The grid points are represented by the peaks in figure 4.5. Using an algorithm, the peaks are identified (symbolized with a red cross in 4.5). Since some of the peaks are not identified automatically, those have to be added manually. After the calibration with a sweep run, all grid points are identified in the read-out grid mask, allowing to calculate the interaction point of the beam and thus its position in the laboratory frame.

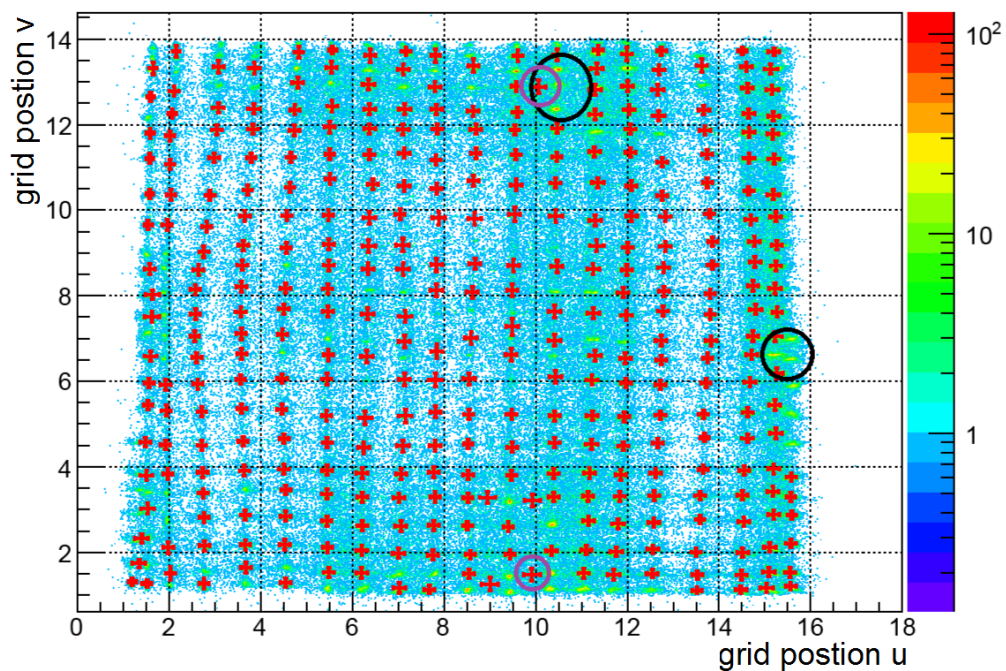


**Figure 4.5** – This two-dimensional plot shows the ongoing calibration of a GFI detector. A automated script is used to identify the peaks. If a peak (= a fiber) is successfully reconstructed, it and the corresponding error margin are indicated with the red crosses. It is visible, that some fibers are not reconstructed properly (black circles) or a product of false reconstruction (purple circle). The former is a product of insufficient statistics, while the latter a product of fibers that are very close each other. Both phenomena have to be corrected manually.

### 4.2.6 TFW

The TFW is the last detector in the s405 setup. It is a scintillation detector, thus measuring time and energy. In general, the calibration of the different organic scintillator detectors within the LAND/R<sup>3</sup>B setup follows the same principles, though the analysis process makes different stages of the calibration necessary.

- TCAL and SYNC level are reached in the same fashion as for the LENA detector (see 4.2.4).
- For the DHIT level, both PMTs on each paddle are combined. This results in only one time and energy information for each paddle.
- In the HIT level, the entire detector is treated as one unit, no individual paddle information are given anymore.

The calibration is mostly done by automated scripts, while some adjustments are made by the experimental researcher.

The time information allows to determine the time-of-flight between the first POS detector and the TFW. From the measured energy information it is possible to calculate the charge of the incoming isotope. The relation between the charge and deposited energy is given by:

$$Z \propto \beta \sqrt{(\Delta E)} \quad (4.2)$$

This is based on the energy-loss in the detector material described by the Bethe-formula [39]:

$$-\frac{dE}{dx} = \frac{4\pi n z^3}{m_e c^2 \beta^2} \cdot \left(\frac{e^2}{4\pi\epsilon_0}\right)^2 \cdot \left[ \ln \left( \frac{2m_e \cdot c^2 \cdot \beta^2}{I \cdot (1 - \beta^2)} \right) - \beta^2 \right] \quad (4.3)$$

The vacuum permittivity is depicted as  $\epsilon_0$ ,  $n$  is the electron density and  $I$  average excitation potential. For small energies the validity of the formula is severely limited.



# 5

## Results and Discussion

With all detectors calibrated, the analysis based on the determined physical parameters like charge, mass and energy can proceed. The application of well-chosen cuts on the multidimensional experimental data is aimed to reduce the background more than the signal. Cuts are conditions in one dimension of the multidimensional event data, e.g. conditions on the  $\gamma$ -energy, when looking on the reconstructed  $E_{kin}^{neutron}$  or other parameters.

### 5.1 Removal of the Background Contribution

Since a pure-proton target is more complicated to handle, an organic target ( $\text{CH}_2$ ) was used to measure the  $^{152}\text{Sm}(p,n)^{152}\text{Eu}$  reaction. This target is easy to handle and can be produced or acquired at low costs. On the downside, it also contains carbon atoms bound in the polyethylene molecules. In order to determine the reaction on the hydrogen atoms only, the reactions on the carbon atoms have to be subtracted. In addition, there are reactions between the beam and the setup, where no target is involved. This leads to background signals in all detectors which have to be removed from the  $\text{CH}_2$  data as well as the contributions from carbon.

## 5. Results and Discussion

To remove the reactions on carbon atoms of the CH<sub>2</sub> target, runs with a pure carbon target were carried out (compare chapter 2.1). The areal density of both targets have to be scaled. This is called the target thickness  $d_T$ , given in  $\frac{\text{g}}{\text{cm}^2}$ . With the target thickness calculated from the density  $\rho_T$  of the target material and the flight path through the target, the ratio between the carbon atoms in both targets can be derived using the the molar Mass  $M_T$  as well as the Avogadro number  $N_A$ . The correction factor  $\xi$  is introduced.

$$\xi = \left( \frac{d_{\text{CH}_2} \times N_A}{M_{\text{CH}_2}} \frac{M_C}{d_C \times N_A} \right) \quad (5.1)$$

Taking into account, that the target-independent background has to be subtracted too, the probability for a reaction on a single proton ( $P_{\text{prot}}$ ) is calculated from the probabilities of reaction on the CH<sub>2</sub> ( $P_{\text{CH}_2}$ ), the carbon ( $P_C$ ) target and the background contribution ( $P_{\text{NT}}$ ):

$$P_{\text{prot}} = 0.5 \cdot P_{\text{H}_2} = 0.5 \cdot (P_{\text{CH}_2} - \xi \cdot P_C - P_{\text{NT}}(1 - \xi)) \quad (5.2)$$

This calculation leaves the proton-induced reaction data. The result is the  $P_{\text{H}_2}$ , to scale it to a single-proton contribution a factor of 0.5 is introduced.

The reaction probabilities ( $P_T$ ) are calculated by determining the isotopes reacting with the target in relation to the incoming particles.

For the subtraction of background and carbon contribution from plotted data, the corresponding spectra are scaled and then subtracted.

The factor scaling factor is calculated to be  $\xi = 0.955303$ . This represents the very shallow contribution of the setup itself to the data that has to be removed.

## 5.2 Data Selection Steps

Extracting the physical reaction data the experimental researcher is interested in from the whole pile of recorded data poses a huge challenge. This is especially the case when the studied reactions have small reaction probabilities. To filter the data so called data selection steps (*DSS*) are introduced. The numbering is an effect of the order in which those constraints are used during the analyzing process.

### 5.2.1 Reconstruction of the Kinetic Energy

The goal of the analysis was to measure the  $E_{\text{kin}}^{\text{neutron}}$  in dependence of the emitted  $\Theta_{\text{lab}}$  as laid down in chapter 2 and thus to proof the method of replacing the measurement of electron capture with charge-exchange reactions.

The determination of the emission angle was discussed in the previous chapter 4.2.4. Using the time-of-flight method, the  $E_{\text{kin}}^{\text{neutron}}$  for each neutron on each individual detector bar was calculated, completing the set of necessary parameters. To allow a comparison, the data of each target run is scaled to a single event (see section 5.2.2.1).

## 5. Results and Discussion

### 5.2.1.1 Time-of-Flight

The time-of-flight was measured using the time difference between a particle passing the POS detector in front of the target and a valid signal in LENA. Figure 5.1 shows the time-of-flight spectra between the target and LENA in nanoseconds. The upper plot shows the time-of-flight spectrum with the condition of a valid signal in LENA and POS as only restriction, while the middle ones shows the same plot after the final analysis with DSS 4 applied. The different data selection steps will be discussed in the next section in detail. The blue circles represent the data from CH<sub>2</sub> runs, the green triangles the data from carbon runs and the red squares represent the run data without any target. After subtracting those latter two contribution, the data from reactions on a single proton in the target are left. Those are indicated with magenta diamonds and are additionally shown at the bottom of figure 5.1.

The first peak is the result of the so called  $\gamma$ -*flash*: When the beam isotopes hit the target a huge amount of  $\gamma$ -rays is emitted. They arrive at the LENA detector in around 100 centimeters away in a time of 3 ns, corresponding to the speed-of-light in air. The broadening is a result of the setup geometries, the flight-paths may vary between 76 and 120 cm which translates to a time range of 2.6 and 4.5 ns. In addition a contribution from non-target interaction may lead to further broadening of the peak.



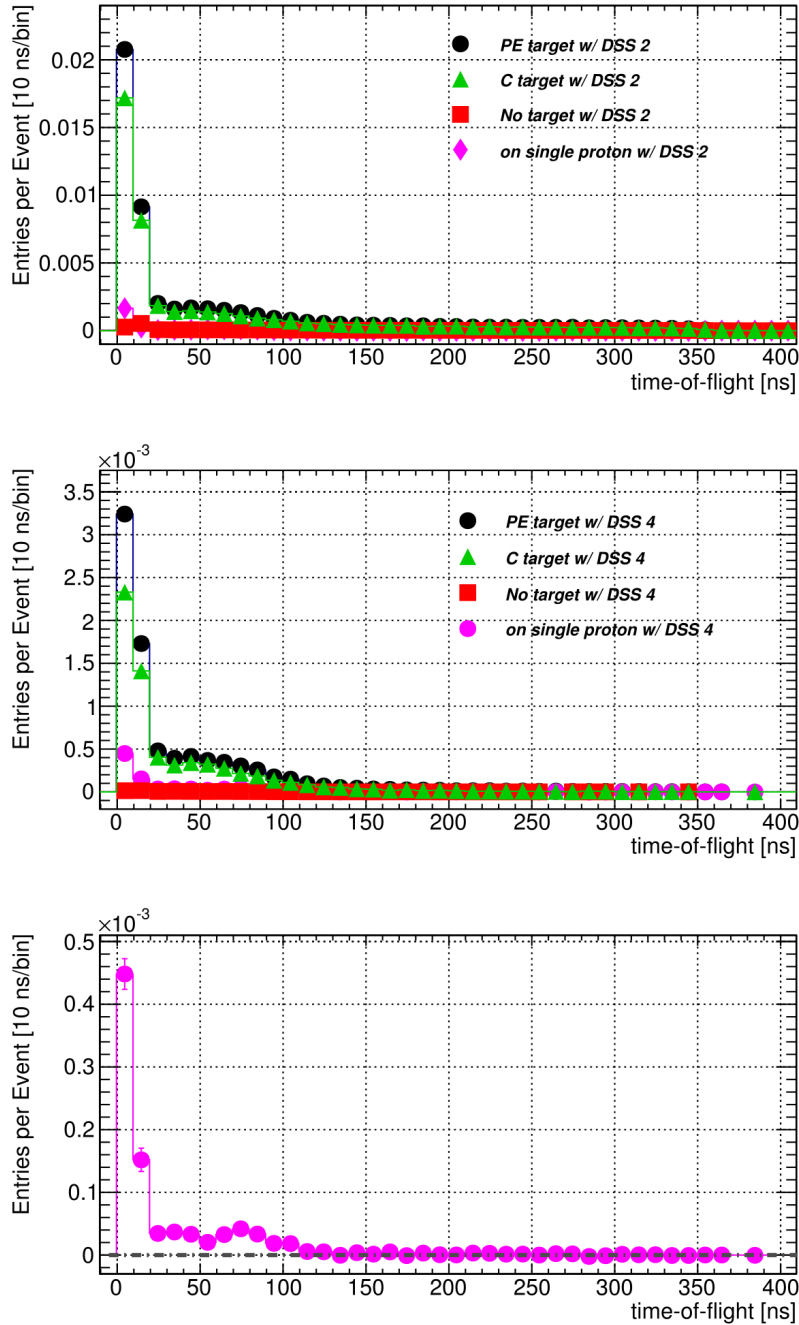


**Figure 5.1** – Time-of-flight spectra gathered with LENA. The upper spectrum shows the spectrum with only minor cuts while on the lower spectrum a majority of the cut set applied (DSS 4). The peak originating from the gamma-flash is visible in the region of around 3.5 ns. This corresponds to the distance of around 76-110 cm between the target and the individual LENA bars. The region of interest for the expected neutrons begins at about 60 ns.

## 5. Results and Discussion

### 5.2.1.2 Inverted Velocity

LENA consists of fifteen individual bars with fifteen individual positions, thus the time-of-flights can not easily be compared. A more suitable way to represent the individual flight times is the  $t/s$ -plot: dividing the flight time by the flight path.

The flight path was acquired using the interaction point within the individual LENA bar and assuming a straight flight path between the target and it.

The time is divided by the length of the flight path resulting in an inverted velocity which is independent of the flight path itself. Considering the complex geometric of LENA, this exposure represents the time-dependent data better than a pure time-of-flight spectrum. The results are shown in figure 5.2. The color coding is similar to the one used in 5.1. In the plot at the bottom, the data from interaction with a single proton after passing the data selection steps up to fourth. The first peak originates from  $\gamma$ s, which travel at the speed-of-light. The second bump, which is highlighted after applying data selection steps may be a result of neutrons in the desired kinetic energy range. It can be seen, that with applying the set of data selection steps the ratio between reactions on protons and background can be changed in favor of the first.

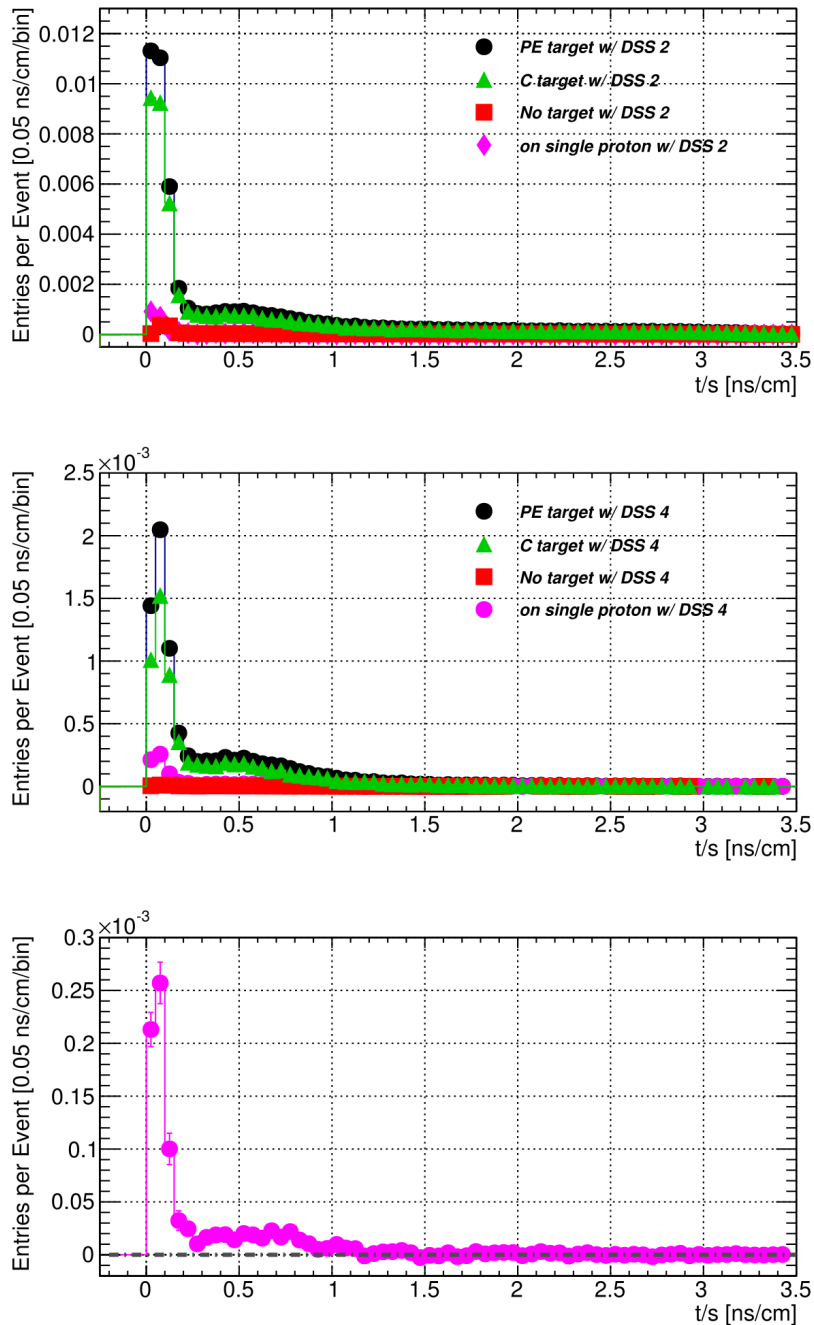


**Figure 5.2** – Inverted velocity spectra gathered with LENA. The upper spectrum shows the  $t/s$  spectrum with only minor cuts while on the lower spectrum a majority of the cut set applied (DSS 4). This plot is an improvement to the time-of-flight plots, because it gets rid of the dependence on the flight path. This is very useful since LENA consists of fifteen bars with different spacings.

## 5. Results and Discussion

### 5.2.1.3 Reconstruction of the Kinetic Energy

The main analysis task of the s405 experiment is the testing of LENA under experimental conditions and the reconstructing of the low-energy neutrons from the  $^{152}\text{Sm}(p,n)^{152}\text{Eu}$  reaction. With the flight path and time-of-flight in hand the  $E_{\text{kin}}^{\text{neutron}}$  was calculated via the formula 2.4. Neutrons are assumed, therefore the mass of a neutron is considered in the calculation. For each paddle the individual distance and angle in respect to the target as well as the point of interaction inside the bar were considered.

#### $E_{\text{kin}}^{\text{neutron}}$ as a benchmark

The event selection from the signals in LENA is optimized to the reconstruction of the expected (p,n) reaction kinematics. In order to improve the signal-to-background ratio different cuts were studied and applied. The spectra of the determined  $E_{\text{kin}}^{\text{neutron}}$  in the range from 20 to 1200 keV will be used as a benchmark to illustrate the effectiveness and efficiency of the applied cuts. Following the order as used in the analysis process a total of five data selection steps will be discussed. In the summary of this work, the efficiency and applicability of those will be pointed out.

## 5.2.2 Neutron-Related Cuts

### 5.2.2.1 Trigger Patterns

#### Scaling Basis - TPat&8

A specific trigger pattern is used as a basic ingredient for background and noise subtraction. To scale the CH<sub>2</sub>, carbon and no-target data recorded in different run-length, a scaling basis in respect to unreacted events has to be defined: The isotopes have to reach the TFW detector at the end of the setup. This is provided by the trigger pattern 8, thus defining TPat&8 as the standard for a valid event and appointing the scaling factor for comparison of the different target runs. All the spectra shown in this section are scaled in respect to this trigger pattern. It has to be noted that TPat&8 is downscaled by a factor of 256.

#### TPat&16 - Data Selection Step 2

The first in-analysis constraint on the data is the trigger pattern. As described in section 4.1.1 the information which detector responded for each individual event is available. The focus in the  $^{152}\text{Sm}(p,n)^{152}\text{Eu}$  reaction measurement is placed on the low-energy neutrons resulting from the (p,n) reaction. Therefore, the first condition used in the analysis is a trigger-signal in LENA (as explained in section 4.1.1). Events have to be considered useful signal in the LENA detector. This is provided by the trigger pattern 16 (compare table 4.1).

The calculated  $E_{\text{kin}}^{\text{neutron}}$  spectra for all LENA bars after data selection step 2 is applied is shown in figure 5.3. The upper spectra shows the scaled data from the CH<sub>2</sub> (black circle), carbon (green triangles) and no-target runs (red square). The  $E_{\text{kin}}^{\text{neutron}}$  from reactions on a single proton are shown as magenta diamonds and are presented separately in the lower spectrum of figure 5.3. Secondary particles - originating from scattering or other reactions than  $^{152}\text{Sm}(p,n)^{152}\text{Eu}$  - dominate those spectra in this step of analysis. They are measured with a relatively long time-of-flight, resulting in low calculated  $E_{\text{kin}}^{\text{neutron}}$ .

## 5. Results and Discussion

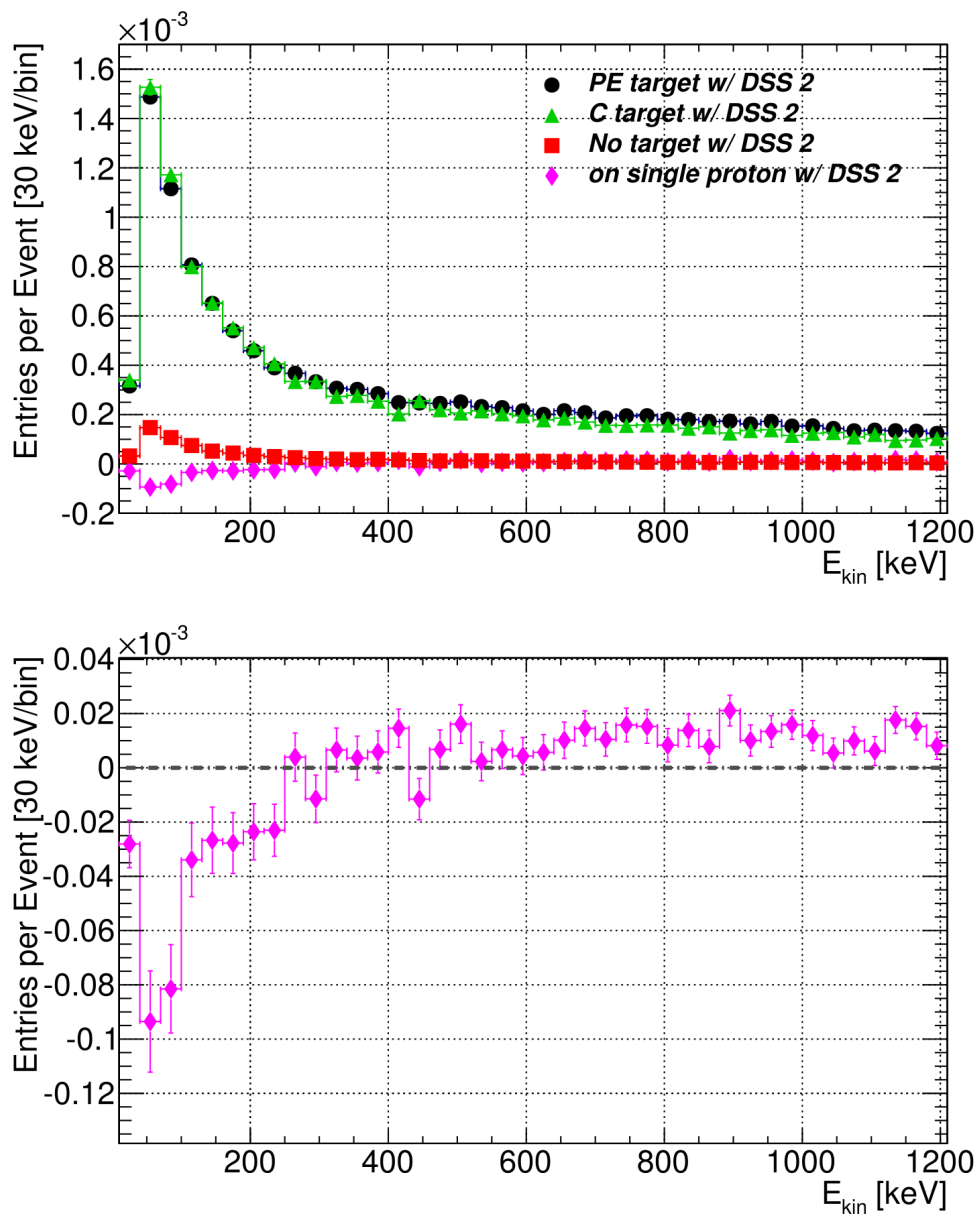


**Figure 5.3** – The calculated  $E_{kin}^{neutron}$  at the data selection step 2. In the plots the scaled data for CH<sub>2</sub> (black circles), carbon (green triangles) and no-target (red squares) runs are show. The subtracted values for the reaction on one proton are indicated by the magenta diamonds and are additionally shown in the lower plot for better comparison. The spectra are dominated by low  $E_{kin}^{neutron}$ , mostly originating from secondary reactions and scattering. Within the errors, the contribution from the carbon and the CH<sub>2</sub> targets are in the same order of magnitude.

### 5.2.2.2 Deposited Energy - DSS 3

In chapter 2.2 it was clarified, that the  $E_{\text{dep}}$  is virtually independent of the  $E_{\text{kin}}$  when considering low-energy neutrons, since energy transfer from neutron to proton within the detector material is dependent on the scattering process and the scattering angle, parameters that are not provided by the detector. From this assumption follows that the measured energy via the electronic read-out  $E_{\text{dep}}$  can not be higher than the actual  $E_{\text{kin}}^{\text{neutron}}$  and therefore the condition of the data selection step 3 is defined as:

$$E_{\text{dep}} \stackrel{!}{\leq} E_{\text{kin}}^{\text{neutron}} \quad (5.3)$$

The figure 5.4 shows the measured  $E_{\text{dep}}$  in dependence of determined  $E_{\text{kin}}^{\text{neutron}}$  within LENA. The diagonal line shows the cut boundaries. Everything below it is accepted while the events above are dismissed. The plot shows the scaled reaction on a single proton with DSS 4 - except the cut on  $E_{\text{dep}}$  naturally - applied. In figure 5.5 the impact of this cut on the calculated  $E_{\text{kin}}^{\text{neutron}}$  is shown. Similar to 5.3, the upper plot shows the  $E_{\text{kin}}^{\text{neutron}}$  for all targets, and the lower the scaled and subtracted  $E_{\text{kin}}^{\text{neutron}}$  from reactions on a single proton. The data selection step 3 is applied to all data. Unlike the spectrum at DSS 2, the peak at low  $E_{\text{kin}}^{\text{neutron}}$  is heavily reduced and a rather consistent reduction of the yield with increasing  $E_{\text{kin}}^{\text{neutron}}$  can be seen.

This data selection step can clearly reduce the spectra in the  $E_{\text{kin}}^{\text{neutron}}$  region below 100 keV, where a lot of secondary and scattered particles are removed. This is true for very slow neutrons stemming from reactions with the surroundings as well as those from cross-talk and  $\gamma$ -rays produced by both.

## 5. Results and Discussion

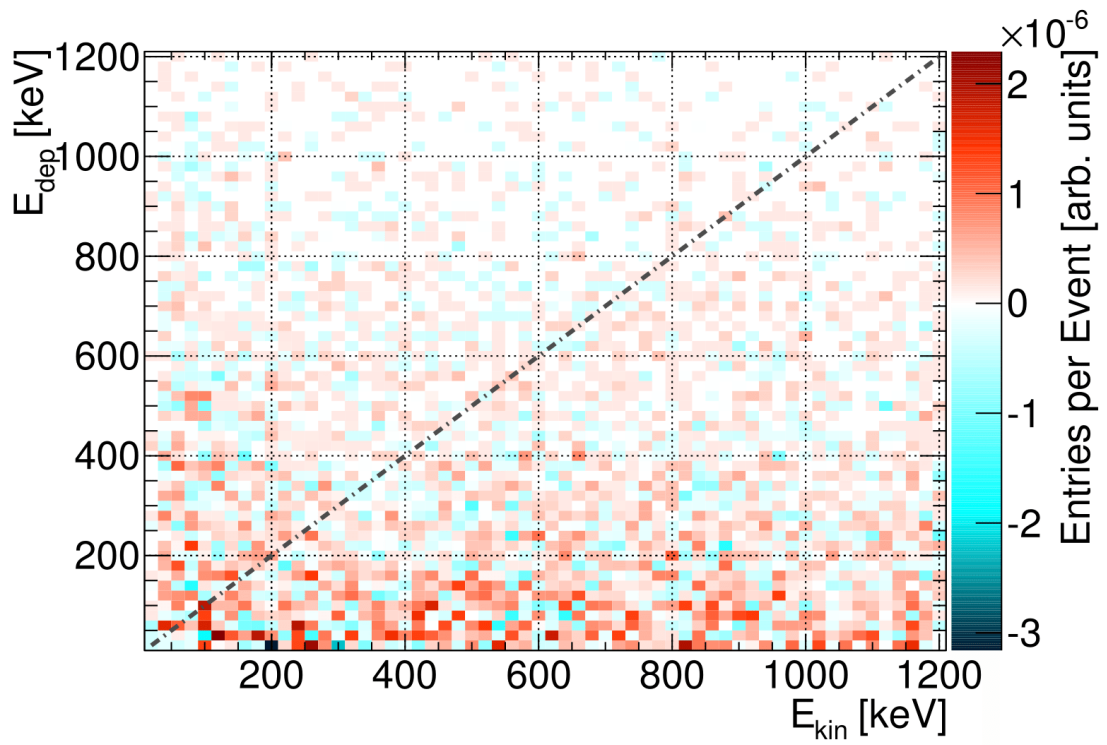


**Figure 5.4** – The measured  $E_{dep}$  as a function of the calculated  $E_{kin}^{neutron}$  within LENA. The dotted line shows the threshold for the acceptance of events in respect to their measured  $E_{dep}$  as a function of the calculated  $E_{kin}^{neutron}$ . The data shown is the result after applying DSS 4 (see next chapter) - but naturally without an constraint on the  $E_{dep}$  - and after subtraction carbon and setup contribution.



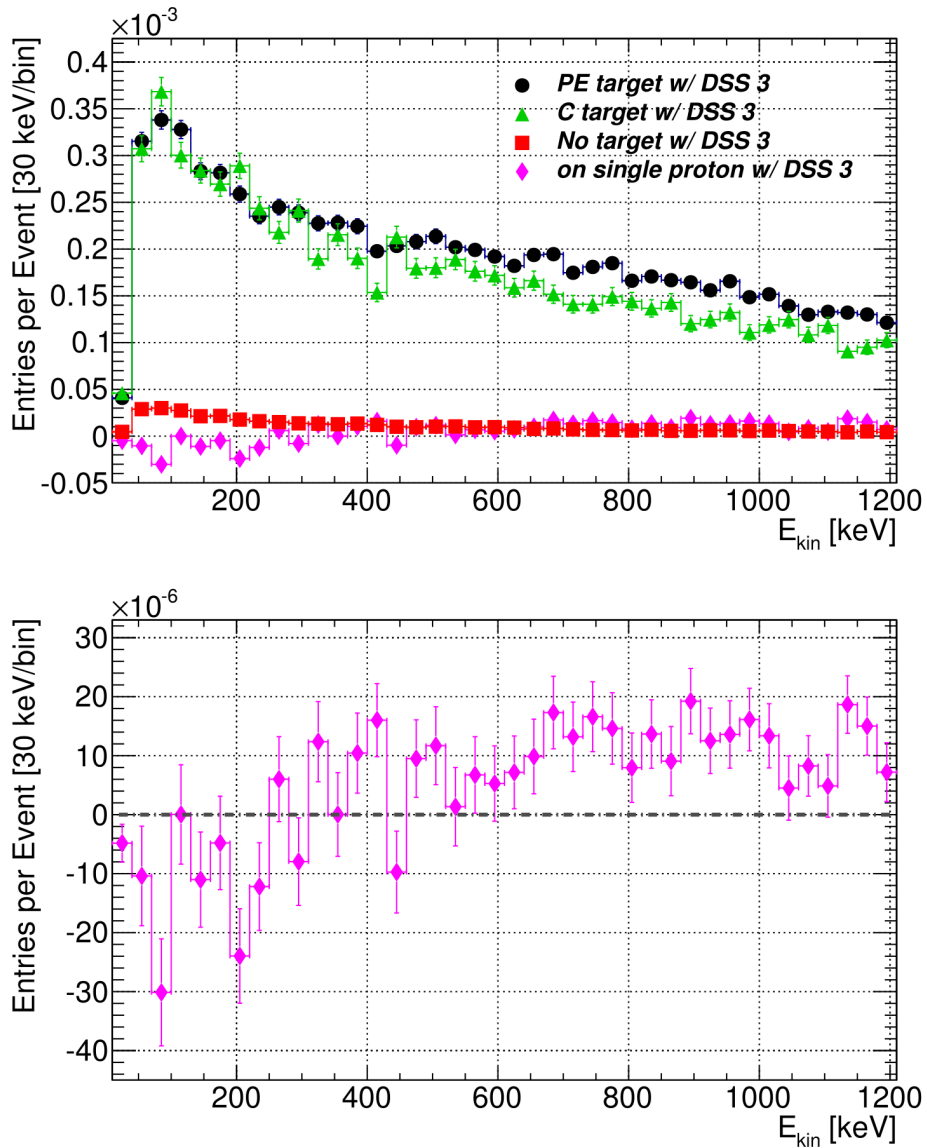


**Figure 5.5** – The calculated  $E_{kin}^{neutron}$  at the data selection step 3. In the plots the scaled data for  $\text{CH}_2$  (black circles), carbon (green triangles) and no-target (red squares) runs are show. The subtracted values for the reaction on one proton are indicated by the magenta diamonds and are additionally shown in the lower plot for better comparison. This selection step removes the excess of low  $E_{kin}^{neutron}$  from secondary and/or scattered particles measured with LENA. In relation to the data selection step 2, the strong peak around a low  $E_{kin}^{neutron}$  is removed and the spectra are declining less steep and smoother.

### 5.2.3 Non-Neutron-Related Data Selection

#### 5.2.3.1 Analyzing the $\gamma$ -Energy Signals

In the  $p(^{152}\text{Sm}, ^{152}\text{Eu})n$  reaction, the excited  $^{152}\text{Eu}$  ejectile emits  $\gamma$ -rays specific to the excitation level during disexcitation. Since the ejectile isotopes are in motion with an reasonable speed, the  $\gamma$ -rays get Doppler shifted and a correction has to be made. Following [40], the measured energy  $E_\gamma$  is calculated from the non-shifted energy with:

$$E_\gamma = E_{\gamma 0} \frac{\sqrt{1 - \beta^2}}{1 - \beta \cos(\theta_\gamma)} \quad (5.4)$$

where  $E_\gamma$  is the actual measured  $\gamma$ -energy in the  $\text{LaBr}_3:\text{Ce}$  detector,  $E_{\gamma 0}$  the unshifted  $\gamma$ -energy and  $\theta_\gamma$  the angle of the detector relative to the beam axis.

Figure 5.6 shows the calculated Doppler-shift for  $\gamma$ -rays of a  $^{152}\text{Sm}$  beam with an energy of 300A MeV as a function of the detector emission angle  $\theta_\gamma$  relative to the beam line.

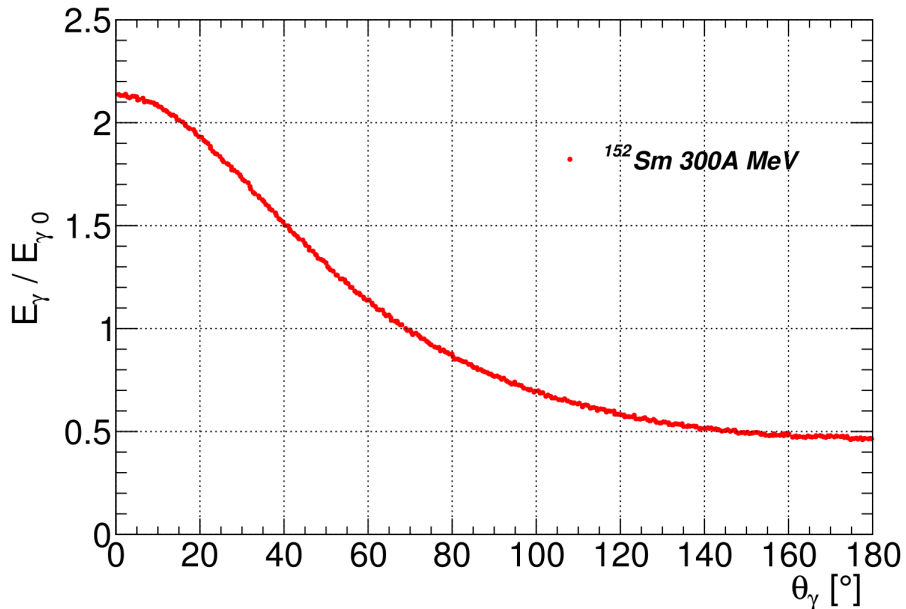


**Figure 5.6** – The figure shows the Doppler-shifted energies for  $\gamma$ -rays dependent on the detection angle relative to the beam line. For the energy of the  $\gamma$ -ray emitting isotope an energy of 300A MeV at the target was assumed.

Taking the angle of around  $\approx 21$  degrees relative to the beam line into account and assuming a  $\beta = 0.6395$  (corresponding to a beam energy of 300A MeV before and 260A MeV after the CH<sub>2</sub> target), the  $E_\gamma$  values for the photons emitted while disexcitating from the three different excitation states are calculated.

Since the angles are given for the centered axis of the cylindrical LaBr<sub>3</sub>:Ce detectors relative to the beam axis, also  $\gamma$ s entering in slightly steeper or flatter slopes have to be considered. The maximal deviation in the angle was estimated to be 8 degrees. The calculations and assumptions lead to the constraints given in table 5.1.

<b>LaBr<sub>3</sub>:Ce - Doppler corrections</b>		
<b>for 21 degrees relative to beam-line</b>		$\pm 8$ degrees
$E_{\gamma_0}$ [keV]	$E_\gamma$ [keV]	Range [keV]
79 keV excitation level		
32.6 ( $I_\gamma$ 100)	62.2	56 - 67
158 keV excitation level		
79.8 ( $I_\gamma$ 100)	152.2	139 - 163
92.8 ( $I_\gamma$ 51)	177	161 - 190
112.5 ( $I_\gamma$ 63)	214.6	196 - 230
249 keV excitation level		
131.2 ( $I_\gamma$ 39)	250.1	228 - 268
171.1 ( $I_\gamma$ 100)	326.4	298 - 349
184 ( $I_\gamma$ 28)	351	321 - 376
203.7 ( $I_\gamma$ 41)	388.6	355 - 416

**Table 5.1** – The table shows the calculated  $\gamma$ -ray energies in the detector which are deviate disexcitation of <sup>152</sup>Eu and the corresponding  $I_\gamma$ . The  $E_{\gamma_0}$  due to the Doppler-shift was determined for all eligible  $\gamma$ s. The third column indicates the acceptances window for the measured  $E_\gamma$ . Decay schemes and energies from [41].

## 5. Results and Discussion

Not only the energy, also the emission angles of the  $\gamma$ -rays are shifted. The light-aberration due to the relativistic velocity of the emitting isotope can be described as

$$\frac{\gamma_{\text{observed}}}{\gamma_{\text{emitted}}} = \frac{1 - \beta^2}{(1 - \beta \cos(\theta_\gamma))^2} \quad (5.5)$$

For a 300A MeV beam this relationship is shown in figure 5.7.

About 12% of the solid angle was covered by the LaBr<sub>3</sub>:Ce detectors defining the geometrical acceptance, while the detector efficiency can be estimated to be close to 100% due to the relatively low  $\gamma$ -energy and the active detection volume of 0.012 m<sup>3</sup> per crystal.

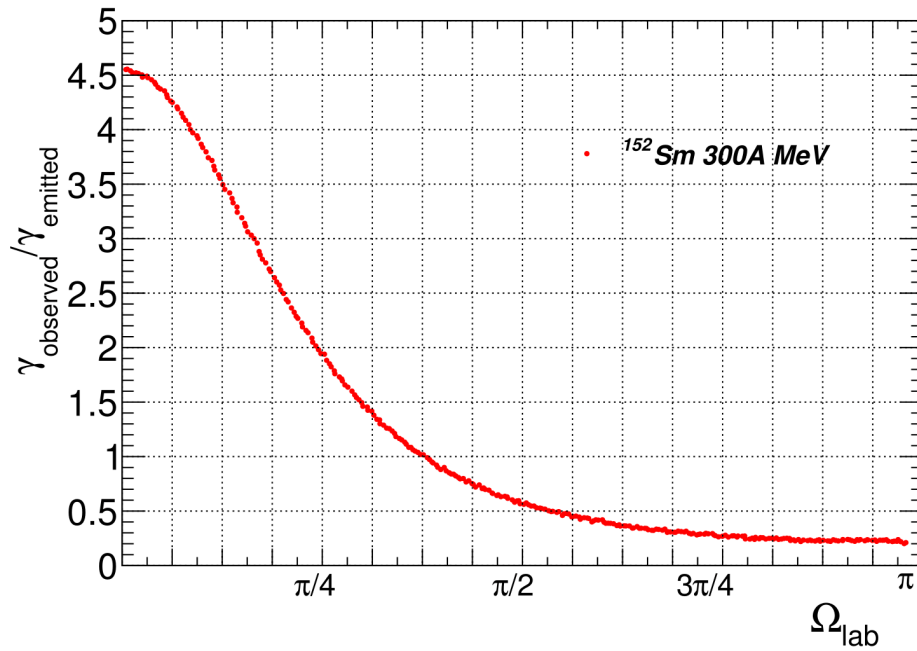


**Figure 5.7** – Calculated light-aberration of the observed  $\gamma$ -rays relative to the solid angle in forward direction for  $\gamma$ -rays stemming from a isotope with an energy of 300A MeV.

The coincidence between  $\gamma$ -rays in the desired energy ranges and valid signals in LENA can be used to reduce background data from the setup and those not originating from (p,n) reactions. Only if a  $\gamma$ -ray with an energy in the restricted energy ranges is measured the event is used for further analysis. The impact of this third data selection step is shown in figure 5.8. While the overall data is reduced, the  $E_{\text{kin}}^{\text{neutron}}$  of reactions on a single proton are favored.

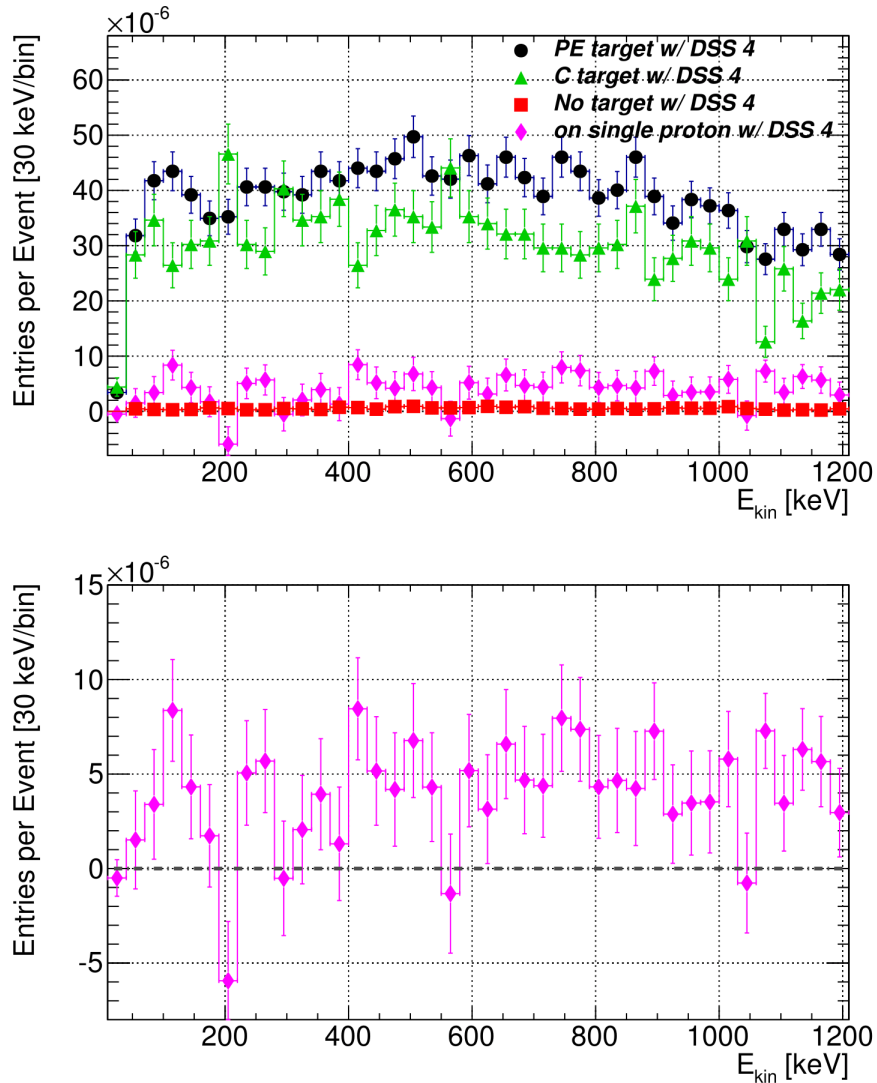


**Figure 5.8** – The calculated  $E_{kin}^{neutron}$  at the data selection step 4. In the plots the scaled data for  $\text{CH}_2$  (black circles), carbon (green triangles) and no-target (red squares) runs are show. The subtracted values for the reaction on one proton are indicated by the magenta diamonds and are additionally shown in the lower plot for better comparison. Applying this constraint on the data, the background can be reduced significantly. Nearly no events are left below the zero-line, implying that reactions on single protons can be emphasized using this data selection step.

## 5. Results and Discussion

### 5.2.3.2 Separating Reaction Products from the Unreacted Beam

An elaborate method to reduce background is based on the differentiation between reacted and unreacted events. The (p,n) reaction induces a change of one atomic charge unit. Two different approaches for the discrimination may be applied: using the TFW and using the TRACKER software.

#### TFW

Usually the energy information gained with the TFW is used to calculate the charge of incoming particles. As described in 4.2.6 the energy loss of the isotopes while passing through the detector can be used to identify the charge. This was first described by Hans Bethe. If the resolution of the resulting spectra is sufficient, it allows to set a restraint on the event selection and therefore distinguish between different isotopes in the outgoing reaction channel.

Unfortunately, in the s405 experiment it was not possible to use this constraint in the established way. Due to the relatively low energy of the heavy  $^{152}\text{Sm}$  isotopes, they got stopped in the TFW. This was leading to a  $Z$  resolution of more than  $2.5 Z$  when fitted with a Gauss-function, making the distinction between  $^{152}\text{Sm}$  and  $^{152}\text{Eu}$  isotopes impossible.

Figures 5.9 and 5.10 show the calculated  $Z_{\text{TFW}}$  using the energy information from the TFW at different DSS. The color coding is similar for all of them: black circles for data from the  $\text{CH}_2$  target, green triangles for the data from the carbon target, red squares for the contribution from the setup and the magenta diamonds for the reactions on a single proton. The first plot in figure 5.9 shows the spectra for  $Z_{\text{TFW}}$  with only DSS 2 applied. The plot below shows the same spectra but at DSS 4. In both no distinctive peak can be seen and therefore a separation between the isotopes of  $^{152}\text{Eu}$  from the  $^{152}\text{Sm}(p,n)^{152}\text{Eu}$  reaction and unreacted  $^{152}\text{Sm}$  isotopes are possible, since the difference in charge is only one unit. To see if a correlation between the  $Z_{\text{TFW}}$  and the reconstructed  $E_{\text{kin}}^{\text{neutron}}$  are seen and this may be used to improve the  $Z_{\text{TFW}}$  resolution, a constraint on  $E_{\text{kin}}^{\text{neutron}}$  was set. The results are shown in figure 5.10. No real improvement could be achieved.

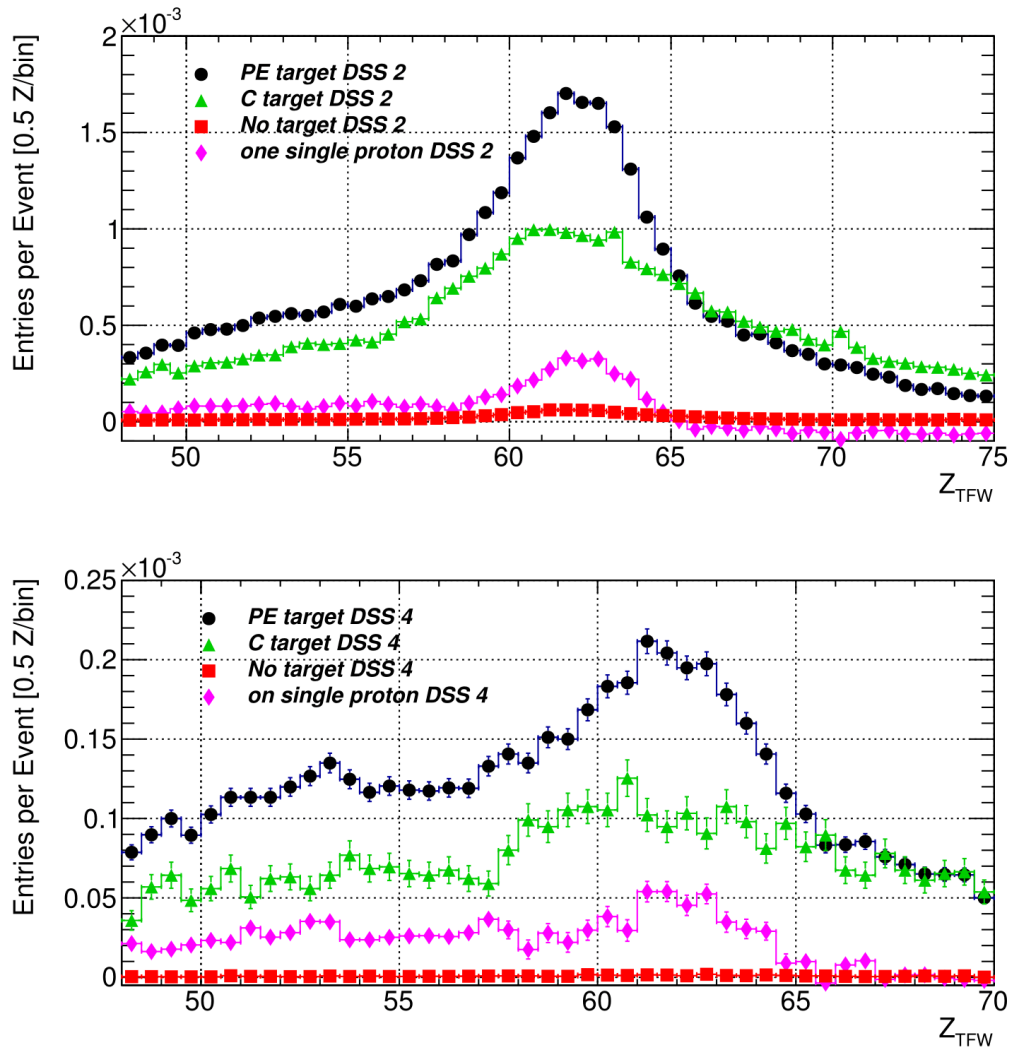


**Figure 5.9** – Determined  $Z$  using the TFW. The upper plot shows the spectra with DSS 2, the lower plot with DSS 4 applied. No distinct peak can be seen, a differentiation between reacted isotopes from the  $^{152}\text{Sm}(p,n)^{152}\text{Eu}$  with  $Z = 63$  and unreacted with  $Z = 62$  is not possible. The application of DSS 4 does not significantly improve the resolution.

## 5. Results and Discussion

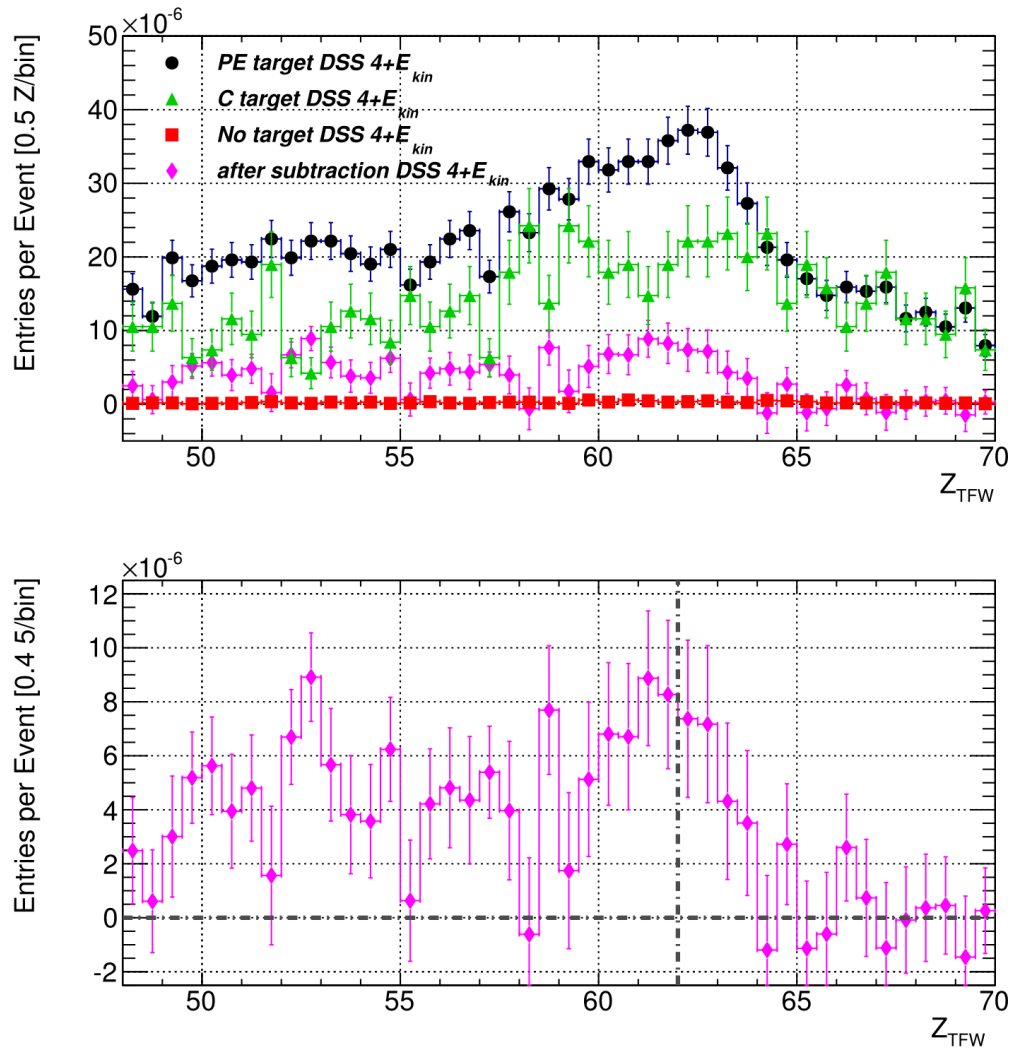


**Figure 5.10** – Determined  $Z$  using the TFW. The upper plot shows the spectra with DSS 4 and an additional constraint on  $E_{kin}^{neutron}$ . This was done to study the correlation of  $Z_{TFW}$  and the expected  $E_{kin}^{neutron}$ . The lower plot shows the data on a single proton with the same DSS conditions. No distinct peak can be seen, a differentiation between reacted isotopes from the  $^{152}\text{Sm}(p,n)^{152}\text{Eu}$  reaction with  $Z = 63$  and unreacted with  $Z = 62$  is not possible.



## Tracking

The second possible technique to separate the different isotopes in the outgoing reaction channel is tracking. The data is prepared using a specially designed software routine, called the *tracker*. It is provided with the positions of the detectors within the experimental setup, the magnetic field distribution of ALADIN and the isotope mass. This information is combined with the vertices of interaction within the position sensitive detectors in the beam line. Reconstructing the trajectory behind and using the position before the dipole magnet, the deflection and thus the charge to mass ratio of the specific isotope. The procedure within the routine uses the following steps: First the position of the isotope in the POS in front of the dipole magnet is determined. Next, the trajectory is guessed, based on the magnetic field and mass of the isotope. It is then compared with the position information from the position sensitive detectors behind the magnet. If the trajectory is not aligned with the position information, it is corrected and the matching process repeated until a sufficient agreement is reached. This method is best suited for lighter isotopes. The results of the tracking, analogue to the determination of the isotopes charge number with the TFW, are used to distinguish between different types of particles in the outgoing reaction channel.

In the s405 experiment a high number of ions per spill were used. The usually available position sensitive detectors around the target, which are used in other experiments in the LAND/R<sup>3</sup>B setup between the target and the dipole magnet, are not capable to handle the high amount of incoming ions. Therefore they were not used in the s405 experiment. An exact determination of the position and angle of the beam before the large dipole magnet was not existent, rendering the further tracking imprecise. Therefore, the standard procedure of tracking in s405 proved to be not sufficient. The results of the tracking are shown in the figures 5.11 and 5.12, with figure 5.11 showing the tracked data for DSS 2 in the upper and DSS 4 in the lower plot. The peak at  $Z = 62$  represents the unreacted beam. After subtracting the non-proton reaction contribution, it nearly disappears, as expected. Around  $Z = 63$  no clear peak can be seen, while a big contribution from non (p,n) reactions is visible at lower  $Z$ . In order to investigate the data for a correlation of  $Z_{\text{Track}}$ , with an additional constraint on  $E_{\text{kin}}^{\text{neutron}}$ , in respect to the expected energy range of the emitted neutrons, was put on the DSS 4 data. This is shown in 5.12. While a small excess around  $Z = 63$  can be seen, it is statistically not sufficient for a qualitative analysis.

## 5. Results and Discussion

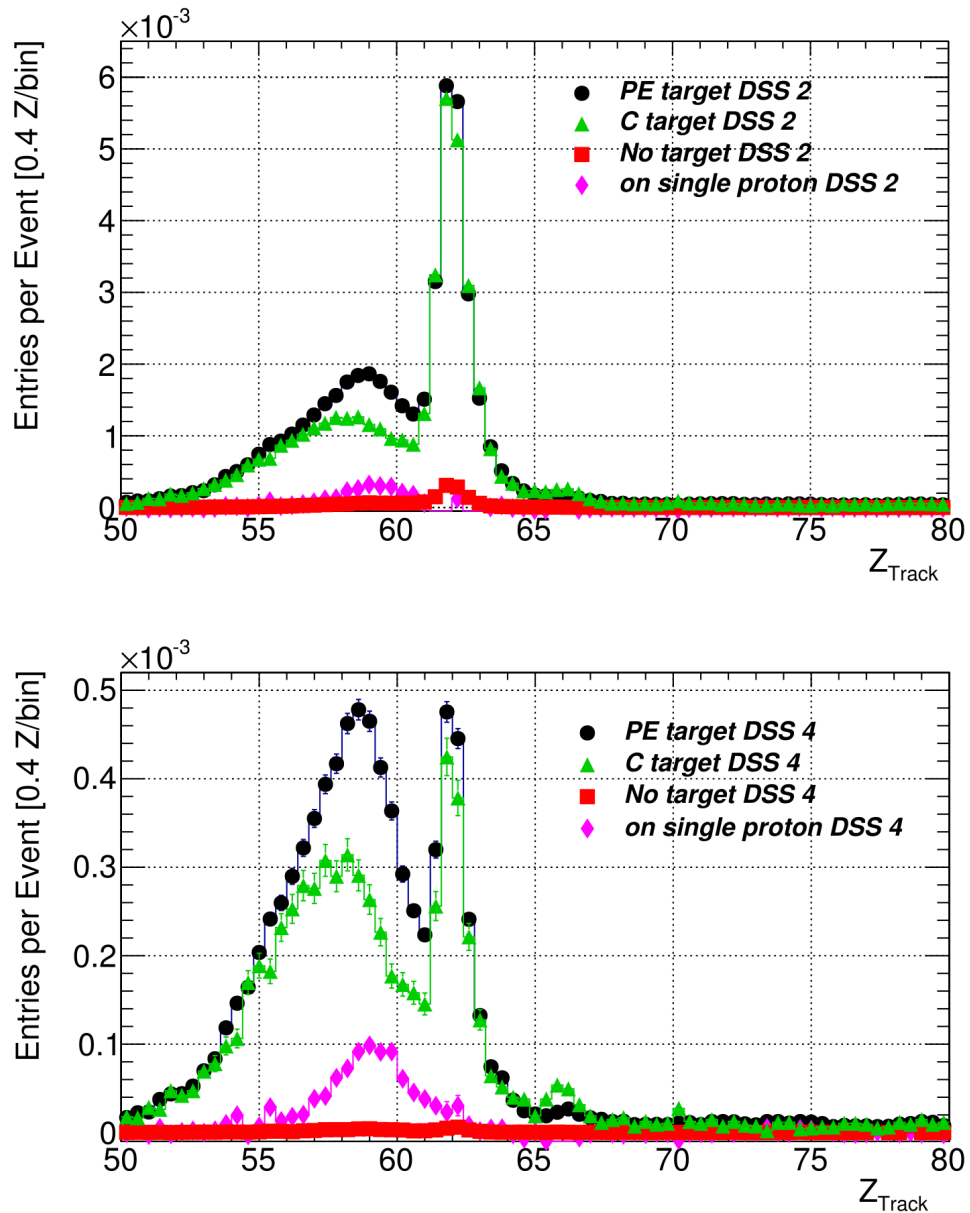


**Figure 5.11** – Determined  $Z$  using the Tracker. The upper plot shows the spectra with DSS 2, the lower plot with DSS 4 applied. While the unreacted isotopes at  $Z = 62$  can be clearly seen, at  $Z = 63$  no excess is visible. After subtracting the carbon and setup contribution to the data, isotopes originating in non (p,n) reactions can be seen at lower  $Z_{\text{Track}}$ . From DSS 2 to 4 the ration between the unreacted peak and the isotopes stemming from diverse reactions and are reconstructed with a smaller  $Z$  is shifted massively in favor of the reacted isotopes allowing to suppress unreacted isotopes with the constraint on  $Z_{\text{Track}}$ .

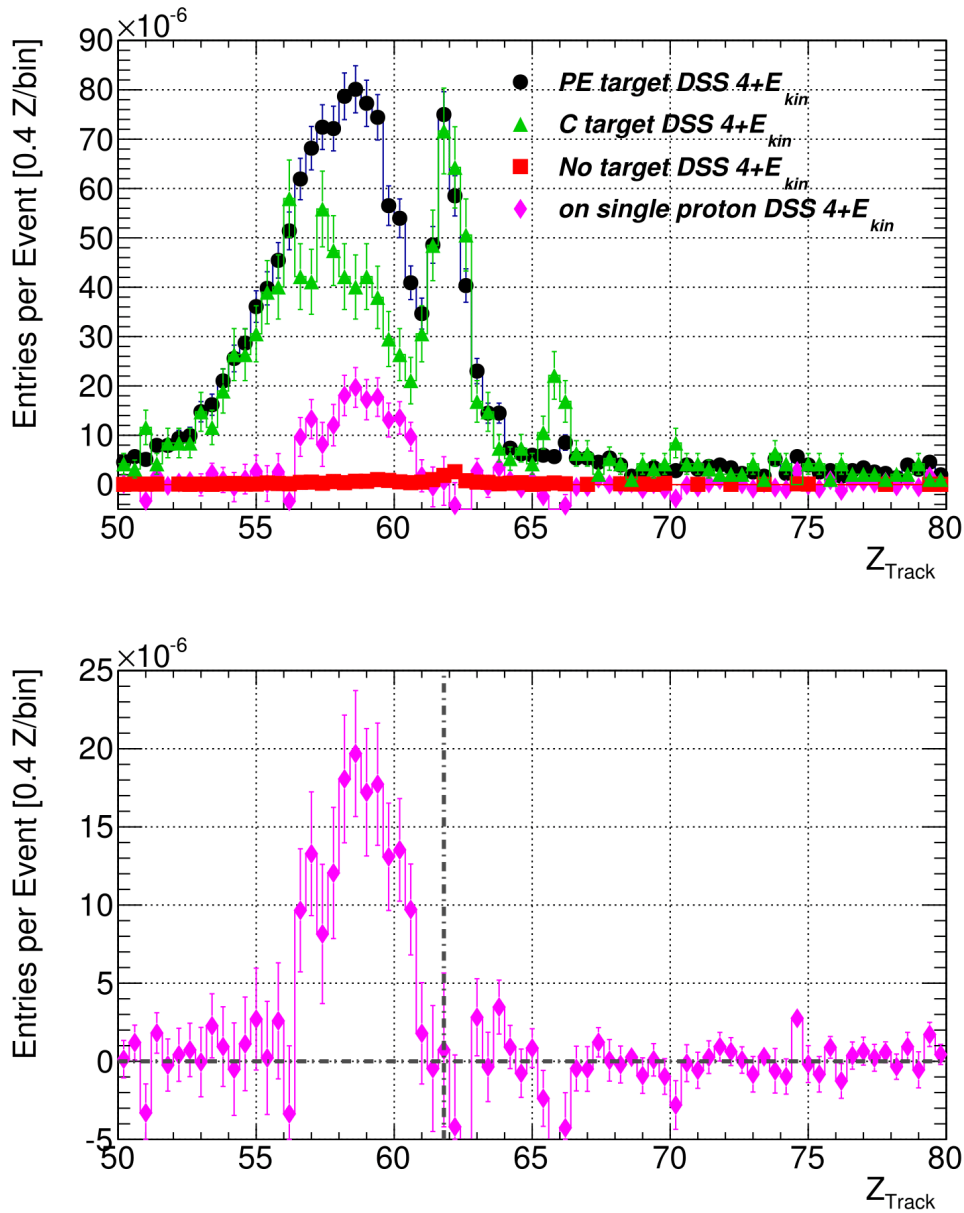


**Figure 5.12** – Determined  $Z$  using the tracker. The upper plot shows the spectra with DSS 4 and an additional constraint on  $E_{kin}^{neutron}$ . This was done to study the correlation of  $Z_{track}$  and the expected  $E_{kin}^{neutron}$ . The lower plot shows the data on a single proton with the same DSS conditions. Around  $Z = 63-64.5$  an excess of signals can be seen, hinting to possible  $^{152}\text{Sm}(p,n)^{152}\text{Eu}$  reaction data.

## 5. Results and Discussion

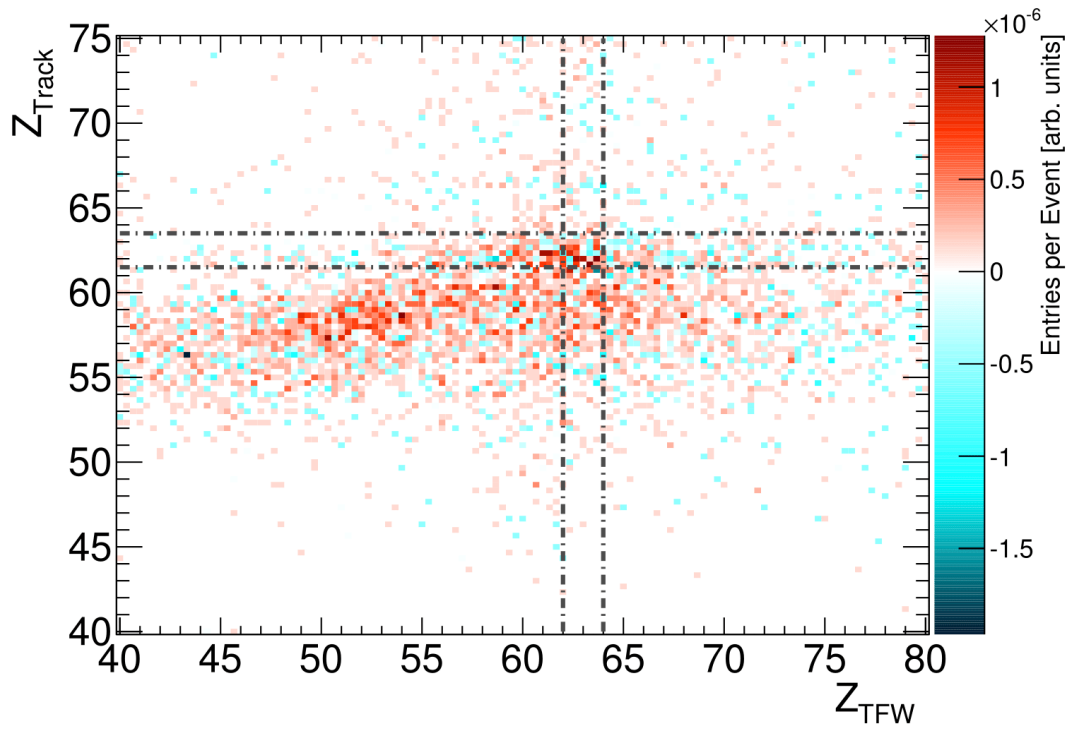
### 5.2.3.3 Combining the $Z$ Determination - DSS 5

The insufficiency in the traditional ways of separating the reacted from unreacted beams leaves the experimental researcher with the challenge of finding a applicable way to distinguish between the reactions.

To compensate those two deviations from the standardized procedure it was tried to combine the diffuse information of both methods. To see if the possible (p,n) data on  $Z_{\text{Track}}$  and  $Z_{\text{TFW}}$  are correlated the two-dimensional relationship was studied. The result with DSS 4 and the restraint on  $E_{\text{kin}}^{\text{neutron}}$  is shown in figure 5.13. It can be seen that the identified  $Z_{\text{TFW}}$  below  $Z = 62$  is correlated with  $Z_{\text{Track}}$  of below  $Z = 62$ . This favors dismissing those events in the further analysis. In addition, there is a faint peak to be identified. From this information the DSS 5 was derived as:

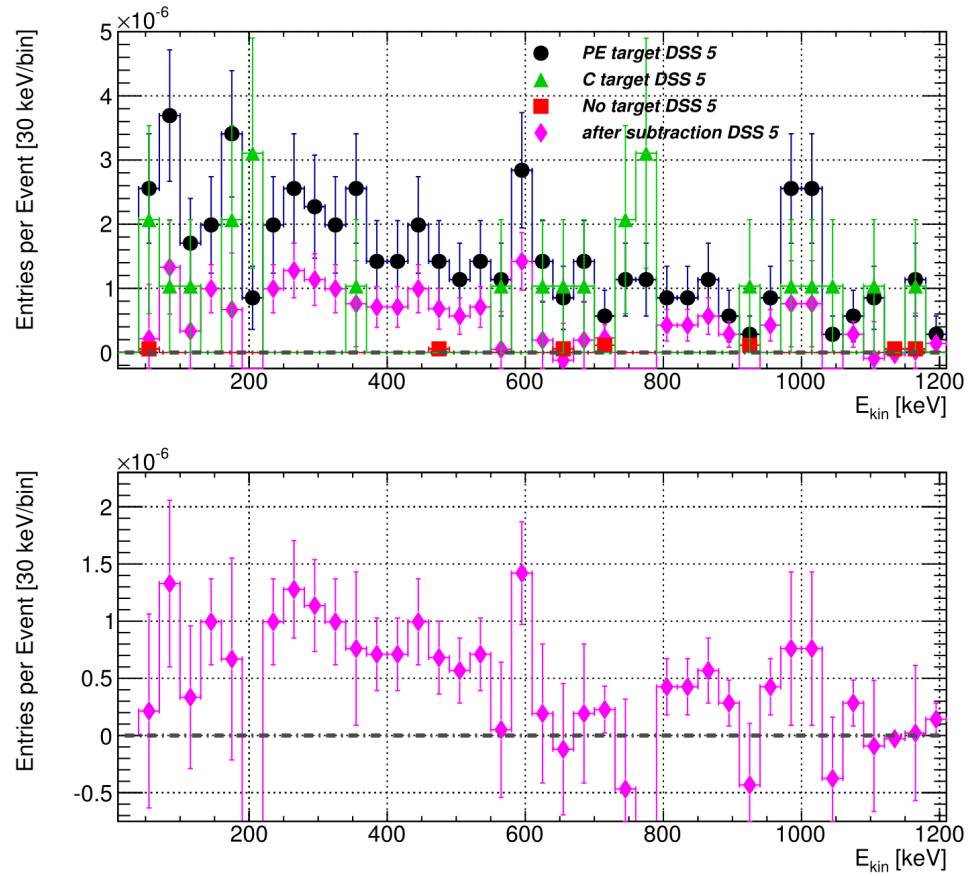
$$Z_{\text{TFW}} \stackrel{!}{\geq} 62 \ \& \ Z_{\text{TFW}} \stackrel{!}{\leq} 64 \ \& \ Z_{\text{Track}} \stackrel{!}{\geq} 62 \ \& \ Z_{\text{Track}} \stackrel{!}{\leq} 63.5 \quad (5.6)$$

Figure 5.14 shows the  $E_{\text{kin}}^{\text{neutron}}$  data with DSS 5 applied. The upper plots show the scaled data for CH<sub>2</sub>, pure carbon and no-target runs as well as the subtracted events. The lower plot shows the cleaned reaction data on a single target proton with DSS 5 applied, too, for better understanding. Nearly no data is below zero what argues for the validity of this constraint. On the other hand the low statistics make the with quantitative analysis of the efficiency of DSS 5 weak.



**Figure 5.13** – Two-dimensional correlation plot of  $Z_{\text{Track}}$  and  $Z_{\text{TFW}}$  with DSS 4 and a constraint on  $E_{\text{kin}}^{\text{neutron}}$  applied. It is implied that the  $Z_{\text{TFW}}$  below 62 are correlated with  $Z_{\text{Track}}$  below 62, suggestion they may stem from non (p,n) data. In addition between the reconstructed charges of 62 and 64 a faint peak can be assumed. Using this information a constraint, indicated by the lines, is derived. The binning is 0.3  $Z$  per bin in both axes.

## 5. Results and Discussion



**Figure 5.14** – The calculated  $E_{kin}^{neutron}$  at the data selection step 5. In the plots the scaled data for  $\text{CH}_2$  (black circles), carbon (green triangles) and no-target (red squares) runs are shown. The subtracted values for the reaction on one proton are indicated by the magenta diamonds and are additionally shown in the lower plot for better comparison. While the complete data is reduced significantly by this DSS, it can be argued that DSS 5 is an improvement in the identification of the  $^{152}\text{Sm}(p,n)^{152}\text{Eu}$  data.

### 5.2.4 Summary

After studying the data and considering different correlations and effects, a total set of five cuts was developed. They were explained in the previous section. The different data selection steps are listed in table 5.2. Processing the data with those, the dependence of the calculated  $E_{kin}^{neutron}$  on the  $\Theta_{lab}$  was determined.

Data selection steps	
Description	DSS
Good Beam	1
Valid Signal in LENA	2
$E_{dep}$	3
LaBr <sub>3</sub> :Ce	4
$Z_{TFW}$ & $Z_{Track}$	5

**Table 5.2** – The full set of data selection steps as used in the analysis of the s405 experiment. They are presented in the order they have to be passed during the analysis process.

### The Problem of Insufficient Statistics

Due to several complications and challenges during the s405 experiment less data were gathered than planned. After passing the quality cuts too few valid events were left. While the validity of the data selection steps can be assumed, more statistics would improve the study of the  $^{152}\text{Sm}(p,n)^{152}\text{Eu}$  reaction in detail.

### 5.3 Calculating the $E_{\text{kin}}$ as a Function of $\Theta_{\text{lab}}$

The main task in the analysis was to reconstruct the neutron velocity and emission angle as simulated in chapter 2.1. This is done by plotting the calculated  $E_{\text{kin}}^{\text{neutron}}$  as a function of the corresponding angle of the bar in respect to the beam line (see table 4.3 in 4.2.4.2). Since the determination of DSS 5 was a rather vague endeavor, the results for DSS 4 and DSS 5 are shown. The data for reactions on a single proton with DSS 4 applied are shown in 5.15, with DSS 5 applied in figure 5.16. The simulated data are shown by the dotted red line. Due to their positioning two bars (#6 and #9) are outside the predicted  $\Theta_{\text{lab}}$  emission range and therefore should not contain data from the  $^{152}\text{Sm}(p,n)^{152}\text{Eu}$  reaction. This can be used to double-check the analysis. If significant data after applying the data selection steps is shown in the region of 85 - 87 degrees, the background is not correctly suppressed. This is not the case.

At DSS 4 there is no significant data to reproduce the simulated distributions in the relevant  $E_{\text{kin}}^{\text{neutron}}$  ranges and the corresponding emission angles. That is most probably due to the insufficient statistics. Nevertheless an excess of signals in the emission angles of interest are shown compared to the mentioned 85 - 87 degrees area.

If DSS 5 is applied, the total amount of data is reduced dramatically. Especially in the higher  $E_{\text{kin}}^{\text{neutron}}$  ranges at the lower angles, where no neutrons from the  $^{152}\text{Sm}(p,n)^{152}\text{Eu}$  reaction are expected, the number of events is reduced. Along the red lines, which represent the simulated neutron kinematics, some clusters are observable. This may implicate the actual neutron from the  $^{152}\text{Sm}(p,n)^{152}\text{Eu}$  reaction.



### 5.3 Calculating the $E_{kin}$ as a Function of $\Theta_{lab}$

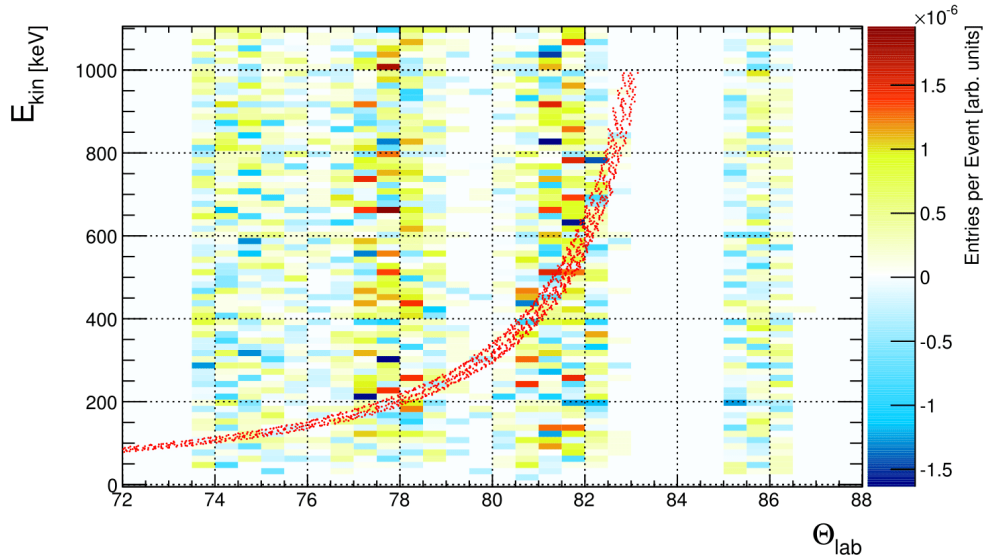


**Figure 5.15** – Reconstructed dependence of  $E_{kin}^{neutron}$  on  $\Theta_{lab}$  at DSS 4. While the two-dimensional plot shows the determined results of reconstruction the expected neutron kinematics in s405. The dotted red line shows the simulated neutron distribution. No definite distributions that would allow a calculation of the reaction probability can be seen in the s405 data. This is most probable a matter of insufficient statistics.

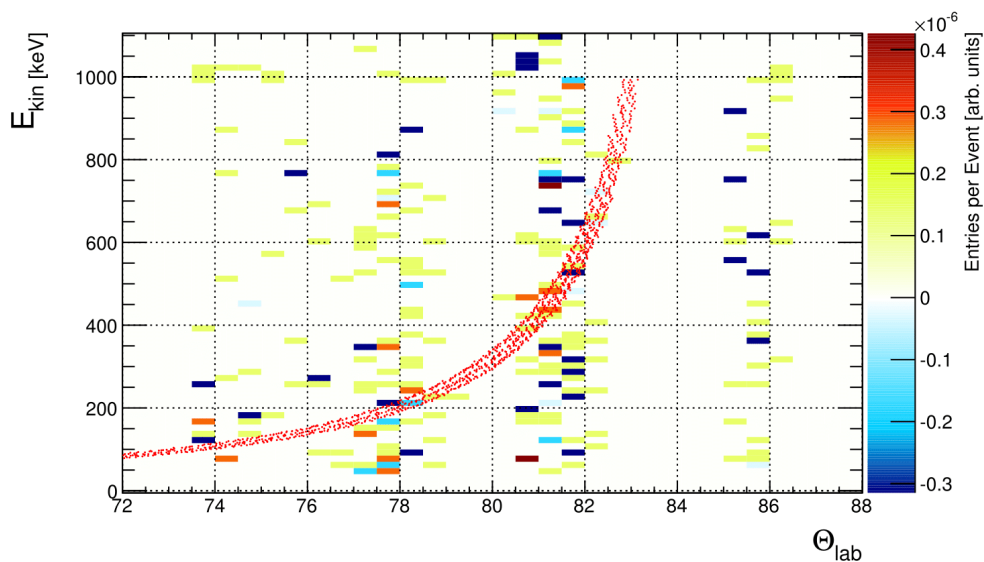


**Figure 5.16** – Reconstructed dependence of  $E_{kin}^{neutron}$  on  $\Theta_{lab}$  at DSS 5. The application of DSS 5 in comparison to DSS 4 shows a significant reduction in the overall data while faintly emphasizing the signals in the expected regions.

### 5.4 Simulation of LENAs Response to Neutrons

To achieve a better understanding of the reaction kinematics as well as the efficiency of the detector and analysis routine, a GEANT3 simulation of the experiment and the expected low-energy neutrons (see 2.1) was performed.

After modeling the setup around the target up to the ALADIN magnet in detail, the emission of low-energy neutrons corresponding to the calculated reaction kinematic (see chapter 2.1) was simulated.

The neutron emission point was placed in the middle of the target sphere. The emitted neutrons followed the calculated 0 to 90 degrees  $\Theta_{\text{lab}}$  distribution and a  $4\pi$  emission distribution in the azimuthal plane.

To understand the response of LENA and get valuable information for future applications, alongside the expected neutrons from the  $^{152}\text{Sm}(p,n)^{152}\text{Eu}$  reaction neutrons from other excitations levels of the ejectile were studied to determine if the distinction between those is possible with LENA alone. The simulated  $^{152}\text{Eu}$  excitation levels were 79, 158, 249, 500, 750, 1000 and 2000 keV. While the first three are the actual excitation levels of  $^{152}\text{Eu}$  may be scattered, the others represent a variety of different energies to study the differences at increasing excitation energy.

400 million neutrons were emitted for each simulated excitation level to gain a sufficient number of reconstructed events and therefore to estimate the efficiency and geometrical acceptance of the detector setup.

During the simulation the time information and the exact point of interaction of each neutron within the LENA detector were recorded, while the resolution of position and time within LENA was considered. Afterwards, the simulated data were analyzed using the same routines as for the real data to calculate the  $E_{\text{kin}}^{\text{neutron}}$  and  $\Theta_{\text{lab}}$  for each individual neutron, using the same determined geometrical information.

#### 5.4 Simulation of LENAs Response to Neutrons

Figure 5.17 shows the results from the simulation for low-energy neutrons emitted by the  $^{152}\text{Eu}$  at excitations levels of 79, 158 and 249 keV. All the measured particles are neutrons originating at the emission-point in the target. Neutrons that are scattered in the surrounding detectors or equipment or are subject to cross-talk between the individual LENA paddles may also be reconstructed and are responsible for the signals outside the simulated neutron distributions. The background from such events can be distinguished from the neutrons directly interacting with LENA. Due to the time resolution of LENA and the uncertainties considering the exact position, the three different groups of neutron are not distinguishable with the neutron detector alone. The lower plot mirrors the upper one, with the simulation-input distributions plotted over the reconstructed spectra.

## 5. Results and Discussion

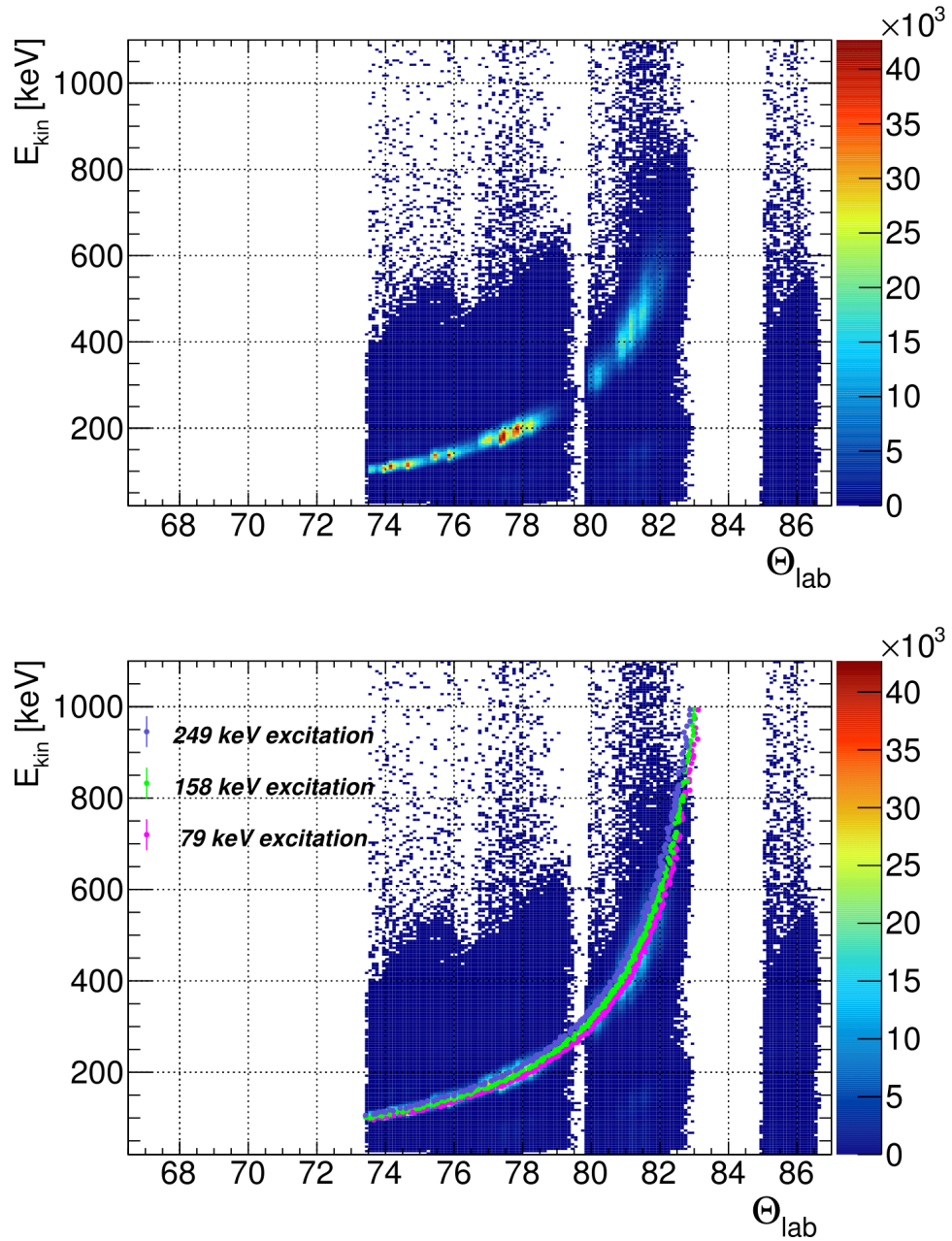


**Figure 5.17** – Simulation of the measurement of low-energy neutrons stemming from the  $^{152}\text{Sm}(p,n)^{152}\text{Eu}$  with LENA. The results from the simulation were folded with the time resolution and uncertainties of the positioning of LENA to make them comparable to the experimental data. The upper plot shows the measured neutrons in LENA with their reconstructed  $E_{\text{kin}}^{\text{neutron}}$  and  $\Theta_{\text{lab}}$ . It is not possible to distinguish between the three different excitation levels. The lower plot shows the same spectra but with the calculated  $E_{\text{kin}}^{\text{neutron}}$  to  $\Theta_{\text{lab}}$  relation. The energy is given with 5 keV per bin, the angle with 0.1 degrees, while the reconstruction efficiency is about 0.9 %.

#### 5.4 Simulation of LENAs Response to Neutrons

Figure 5.18 shows the simulation results for the emitted low-energy neutrons from  $^{152}\text{Eu}$  at the excitation energies of 79, 158, 29, 500, 750, 1000 and 2000 keV. Analogue to 5.17 the upper plot shows the reconstructed data while the lower on also emphasizes the input data. It can be seen, that for  $^{152}\text{Eu}$  excitation states with a few hundred keV the differences are big enough to be resolved with LENA only.

Using the simulation, which includes the geometrical acceptance as well as a detection threshold in terms of the  $E_{\text{dep}}$ , the overall efficiency of LENA in the s405 experiment can be estimated. By integrating the region-of-interest in the two dimensional spectra, the efficiencies are calculated to around 0.9%. In detail they are 0.92 % for the 79 keV, 0.95 % for the 158 keV and 0.94 % for the 249 keV excitation-level of  $^{152}\text{Eu}$  . The efficiency is also listed in table 5.3.

Acceptance and Efficiency for LENA	
excitation level	eff <sub>total</sub>
79 keV	0.92 %
158 keV	0.95 %
249 keV	0.94 %
500 keV	0.90 %
750 keV	0.89 %
1000 keV	0.88 %
2000 keV	0.66 %

**Table 5.3** – The efficiencies of LENA including the geometrical acceptance calculated from the simulations. For the simulated excitation levels of  $^{152}\text{Eu}$  a total of about 0.9 % of the neutrons are measured in the expected  $E_{\text{kin}}^{\text{neutron}}$  to  $\Theta_{\text{lab}}$  ratio. With increasing energies the reconstruction gets more costly. At 2000 keV the  $E_{\text{kin}}^{\text{neutron}}$  increases very fast with  $\Theta_{\text{lab}}$ , so that the highest  $E_{\text{kin}}^{\text{neutron}}$  can not be resolved and the efficiency is reduced to 0.66 % at the simulated detector position.

## 5. Results and Discussion

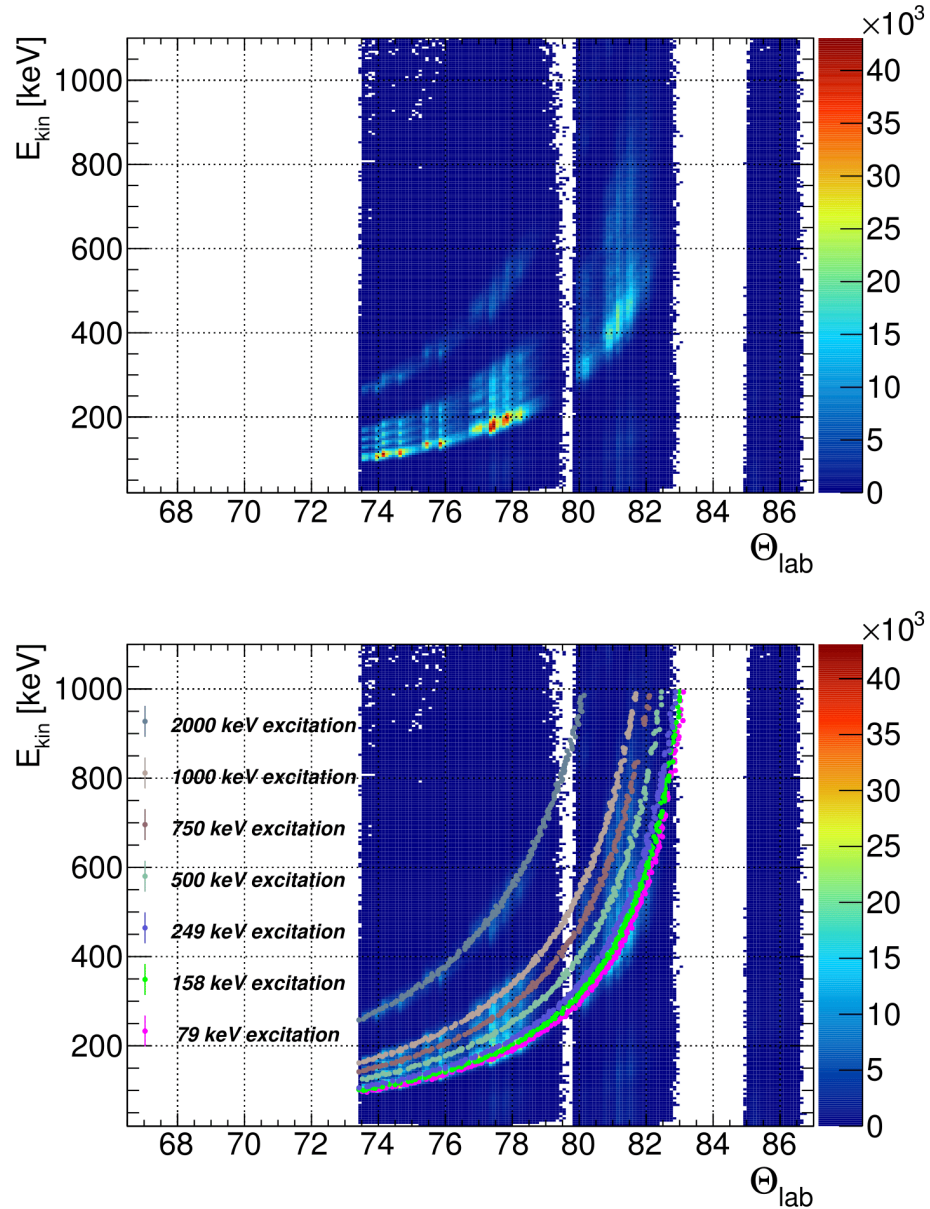


**Figure 5.18** – Simulation of the measurement of low-energy neutrons stemming from  $^{152}\text{Eu}$  with excitation energies of 79, 158, 249, 500, 750, 1000 and 2000 keV LENA. The results from the simulation were folded with the time resolution and uncertainties of the positioning of LENA to make them comparable to the experimental data. The upper plot shows the measured neutrons in LENA with their reconstructed  $E_{\text{kin}}^{\text{neutron}}$  and  $\Theta_{\text{lab}}$ . In difference to the neutrons from the three excitation levels measured in s405, neutrons emitted by excitation levels with higher excitation energies can be differentiated. The lower plot shows the same spectra but with the calculated  $E_{\text{kin}}^{\text{neutron}}$  to  $\Theta_{\text{lab}}$  relation for each excitation level. The reconstruction efficiency decreases from 0.92 for 79 keV to 0.66 % for the 2000 keV level.

# 6

## Summary and Perspectives

### 6.1 Summary

The s405 experiment was a pioneering experiment performed in October of 2011 at the GSI facility. It was proposed to demonstrate the possibility to measure Gamow-Teller transition electron-captures of heavy isotopes by substituting them with a charge-exchange reaction. It was complemented by first tests of the newly developed Low-Energy Neutron detector Array *LENA*. *LENA* is a scintillation detector made of 15 independent detector bars and capable of measuring neutrons with kinetic energies in the range from several keV to several MeV. This capability is especially interesting for (p,n) reactions with low-energy momentum transfers. The experiment was performed with the current LAND/R<sup>3</sup>B setup, using a variety of detectors. The first step in the analysis process was the calibration of those detectors. Organic scintillating detectors were used to gather time and energy information as well as the path of the beam-isotopes. In addition, a  $\gamma$ -ray detector was placed close to the target to measure the photons originating from the disexcitation of the reaction products.

The detectors were calibrated and, if they consist of more than one independent ac-

## 6. Summary and Perspectives

tive volume, synchronized with a focus on the exact reconstruction of the position of each individual LENA bar. Distance and angle with respect to the target were reconstructed using a photogrammetry software. The dependence of the energy of the emitted neutrons on their emission angle is crucial for the determination of the reaction parameters.

### Data Selection

Following the calibration, the main task of the analysis was to develop a set of data selection steps, which are suitable to reduce the unwanted background in favor of the  $^{152}\text{Sm}(p,n)^{152}\text{Eu}$  events.

The first two data selection steps were straight forward. A valid signal in all the used detectors as well as a trigger signal from the main detector, LENA, were required.

The next requirement was based on the correlation of deposited energy and the kinetic energy based on the time-of-flight. It was shown that a cut significantly reduces  $\gamma$ -induced background.

Using a  $\gamma$ -detector has advantages and disadvantages. On the one hand, it was shown that the three studied  $^{152}\text{Eu}$  excitation levels of 79, 158 and 249 keV can not be separated using only the reconstructed kinetic energy and the emission angle. The use of an additional  $\gamma$ -energy information to determine the populated excitation levels is indispensable when relatively low-level excitation states with energies close to each other are involved.

On the other hand the usage of a  $\gamma$ -detector reduces the efficiency of the reconstruction significantly. The  $\text{LaBr}_3:\text{Ce}$  detectors used in the s405 experiment covered a solid angle of only 12%. The emission in forward direction, however, (in which the  $\text{LaBr}_3:\text{Ce}$  detector was mounted) is boosted, which slightly improves the reconstruction efficiency.

In addition, the half-lives of the excitation states have to be taken into account. For the  $^{152}\text{Eu}$  excitation state with an energy of 79 keV the half-life is about 120 ns, corresponding to a flight path of about 20 meters. Therefore the freshly produced  $^{152}\text{Eu}$  passes the  $\gamma$ -detector before deexciting. In conclusion, the usage of a  $\gamma$ -detector has to be evaluated for each reaction individually. For short lived excitation levels with excitation energies close to each other a  $4\pi$  detector would be very useful. Figure 6.1 shows the final determined kinetic neutron energy as a function of the reconstructed emission angle  $\Theta_{\text{lab}}$  plot with all data selection steps except any constraint on the  $\gamma$ -energy. In comparison to the data with the constraint on the  $\gamma$ -energy (figure 5.16) the number



of events of the two-dimensional plot is about ten times higher, but no structure along the simulated neutron kinematics can be seen.

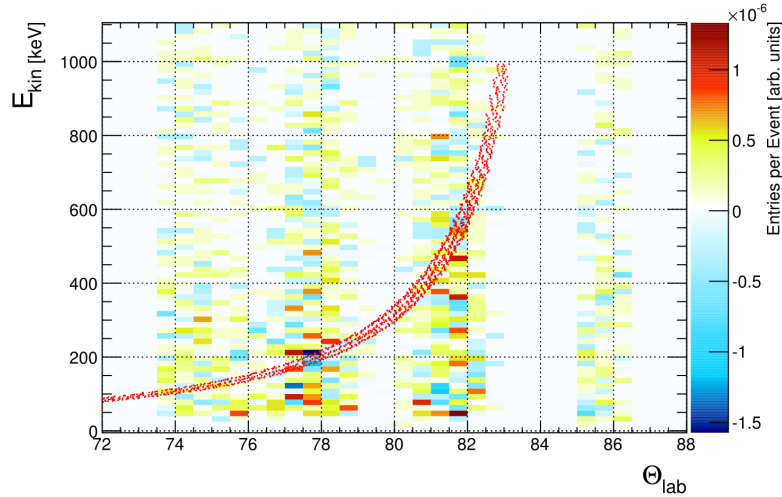


**Figure 6.1** – Reconstructed dependence of  $E_{kin}^{neutron}$  on  $\Theta_{lab}$  at data selection step 5 without a  $\gamma$ -energy constraint. While the  $\gamma$ -constraint significantly reduces the yield, it seems to have no big impact on the distribution of the reconstructed data.

The separation of reacted from incoming beam isotopes posed a proper challenge. In s405 none of the established methods were effective. The first method investigated here is using the time-of-flight wall (*TFW*) to calculate the isotope charge  $Z$  from the energy loss in the detector. In s405 the resolution of the isotope charge determined with the *TFW* ( $Z_{TFW}$ ) was more than 2.7 units of charge. One reason for the broad signals in  $Z_{TFW}$  is the stopping of the beam isotopes within the *TFW*. Because of the rather low beam energy of 300 A MeV the isotopes lost all their energy in the setup, finally stopping in the *TFW* and not passing the whole detector volumes.

For a successful tracking, precise information on angle and position of the ions passing the target is needed. Due to the high rate of incoming beam particles, the position and angle sensitive detectors, which are usually used around the target, were dismissed. This makes a determination of the charge of the reaction products via the tracking software challenging.

In order get distinguish between products and unreacted isotopes in s405, a combination of both flawed method was used. After studying various correlations and dependencies, a rough constraint on the reconstructed charge of the passing ions was developed. It mostly suppresses of non-(p,n) reaction data, but a clear distinction between  $Z = 62$  for  $^{152}\text{Sm}$  and  $Z = 63$  for  $^{152}\text{Eu}$  was not possible.

## 6. Summary and Perspectives

### Conclusion

The low-energy neutron detector array LENA proved successful in its first real usage in an high-energy beam experiment. LENA can be adapted to the experimental needs and is therefore a powerful tool. The efficiency of LENA can be improved by increasing the number of detector volumes. It has to be noted that also the geometrical acceptance of LENA can be optimized. With a better  $Z$  reconstruction and a longer run time to gain more information, the determination of the (p,n) cross section for heavy isotopes would have been possible. Only 48 hours of beam time were available.

For lighter isotopes the substitution of electron capture with charge-exchange reactions was successfully performed at MSU [42].

## 6.2 Perspectives

### 6.2.1 Future Plans - R<sup>3</sup>B at FAIR

In 2003, the German ministry for research and education (Bundesministerium für Bildung und Forschung or *BMBF*) decided, following the recommendation of the science expert groups, and approved the plan to upgrade the GSI Helmholtzzentrum für Schwerionenforschung GmbH to expand the scientific possibilities for future applications. The new, upgraded facility, called the Facility for Antiproton and Ion Research or *FAIR*, is currently built east of the existing GSI facility. First radioactive beams are expected in 2018.

The centerpiece of the new accelerator will be a heavy ion synchrotron with a circumference of around 1100 meters, and additionally a number of new high-capacity storage rings and accelerators will be installed. A layout of the upcoming facility is shown in figure 6.2. The size of the upgrade in relation to the current facility can be clearly seen.

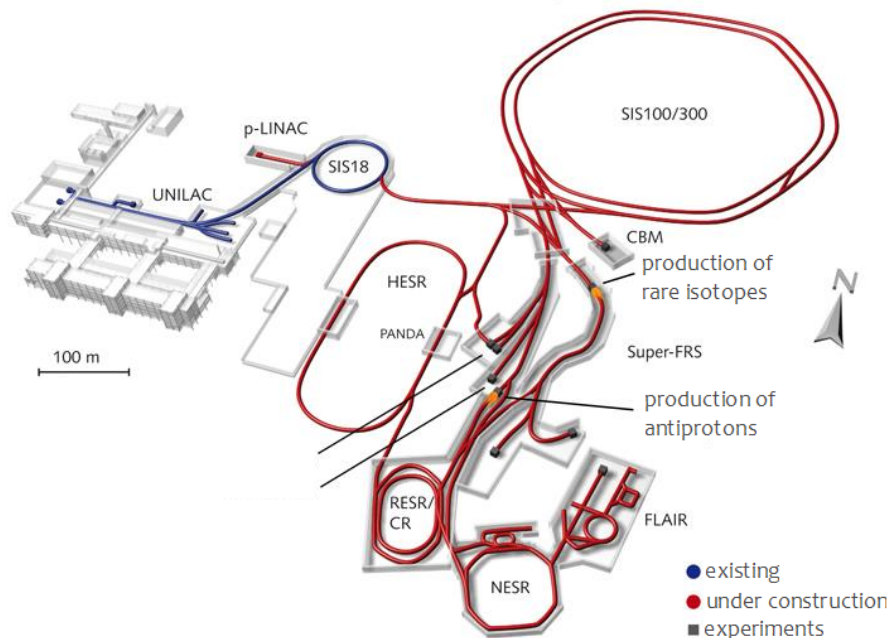


**Figure 6.2** – The upcoming FAIR facility. On the left, the current layout of the GSI facility is shown. The blue lines show the existing beam line parts, that will be included in the new, with red lines marked, beam line and experimental layout. Centerpieces are the SIS 100/300 synchrotron rings. From [31], modified.

## 6. Summary and Perspectives

### **R<sup>3</sup>B**

The Four pillars of the future basic research at FAIR are: Antiproton-proton annihilation, atomic and plasma physics, baryonic matter and nuclear structure and astrophysics. The initiative within nuclear structure and astrophysics are under the umbrella *NUSTAR*, and the LAND/R<sup>3</sup>B setup will be included into the new FAIR facility. During the upgrade, the name will be changed to *R<sup>3</sup>B*, Reactions with Relativistic Radioactive Beams. As currently possible, ions of any element up to uranium will be accelerated in the FAIR laboratory. With the new fragmentation system *SuperFRS* radioactive isotopes can be produced, separated and directed to the experimental setups. In the FAIR laboratory, those radioactive beams can be produced with much higher intensities. Therefore, while the basic layout of the current setup will be preserved, most detectors will be upgraded to new, high performance versions, which will allow a kinematically complete measurement of the reaction products. The planned setup is shown figure 6.3. An addition to the old LAND/R<sup>3</sup>B during the upgrade to the R<sup>3</sup>B setup is the low-energy detector array LENA. Furthermore a new magnet, large area neutron detector, a new  $\gamma$ -detector and time-of-flight walls complete the upgrade. The lessons learned during the s405 experiment are important for the coming years, when the future detectors will be constructed.

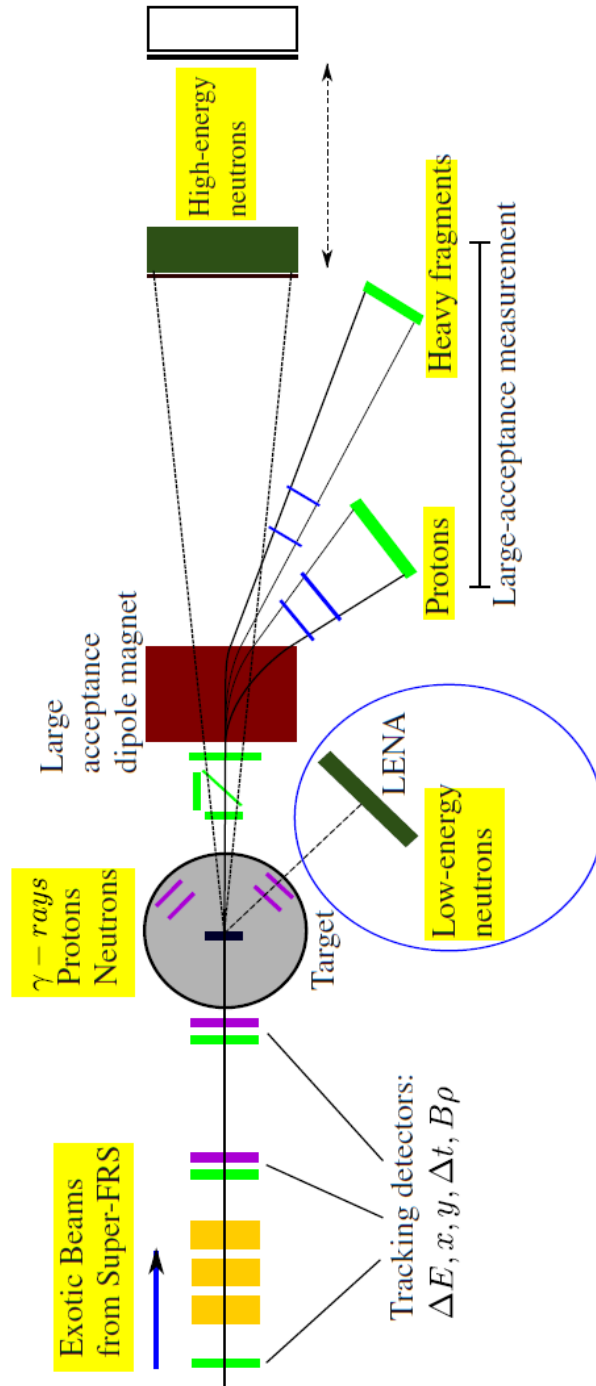


**Figure 6.3** – Drawing of the planned future R<sup>3</sup>B setup at FAIR. While in the basic composition it resembles the current LAND/R<sup>3</sup>B setup (figure 3.2), most detectors will be replaced with more capable ones. A new addition is LENA, which will provide the measurement of low-energy neutrons, an important addition to the desired kinematically complete measurement of the reactions. Image by courtesy of [27]. (Image not to scale)

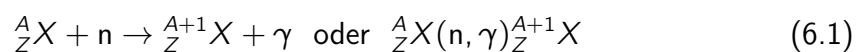


# Zusammenfassung

Mit Ausnahme der sehr leichten Elemente Wasserstoff und Helium haben alle anderen chemischen Elemente sowie deren verschiedene Isotope ihren Ursprung in den vielen Elementfabriken des Universums: Den Sternen.

In diesen Nukleosyntheseprozessen werden zu anfangs in verschiedenen Fusionsreaktionen ausgehend von Wasserstoff immer mehr und schwerere Elemente produziert. Ausgehend von der *pp-Kette* und dem *CNO-Zyklus*, die Wasserstoff zu Helium fusionieren, werden Elemente mit immer höherer Ladungs- ( $Z$ ) und Massezahl ( $A$ ) aufgebaut. Die Fusion von leichten Elementen zu schwereren endet mit der Erzeugung von  $^{56}\text{Fe}$ . Ab diesem Element ist die Coulombbarriere, erzeugt durch die Ladung der Protonen im Nuklidkern, so hoch, dass Fusionsprozesse stark gehemmt werden. Zusätzlich stellen die Isotope um  $^{56}\text{Fe}$  diejenigen mit der höchsten Bindungsenergie da, so dass endotherme Reaktionen für die Erzeugungen von Isotopen mit höherer Masse und Ladung aber geringerer Bindungsenergie notwendig sind.

Von hier an übernehmen andere Prozesse die weitere Synthese von Elementen. Der Großteil der schweren Elemente wird dabei durch Neutroneneinfangprozesse erzeugt. Der dabei grundlegende Prozess ist der Einfang eines Neutrons durch ein Isotop. Diese nukleare Reaktion wird dabei wie folgt beschrieben:



wobei  $A$  und  $Z$  die Isotopmasse bzw. die Ladungszahl sind. Unter der Emission von Photonen wird ein Neutron angelagert, welches aufgrund der nicht vorhandenen Ladung nicht durch die Coulombbarriere blockiert wird. Dies führt zu einer Änderung der Massezahl. Das chemische Element bleibt dabei unverändert. Die stete Erhöhung der Neutronenzahl führt zur Instabilität des Isotopes. Im Stern führt diese Instabilität zu einem  $\beta$ -Zerfall. Dabei entsteht ein Isotop eines anderen chemischen Elements aber

## Zusammenfassung

gleicher Masse:



Je nachdem welches astrophysikalische Szenario assoziiert ist, unterscheidet man zwischen dem schnellen (*rapid*) und langsamen (*slow*) Neutroneneinfangprozess, genannt *r-Prozess* und *s-Prozess*. Während sich beim r-Prozess die Einfangszeiten im Rahmen von Millisekunden bewegen, liegen sie im s-Prozess in der Größenordnung von Jahren. Dementsprechend werden die sehr neutronenreichen Isotope sehr selten im s-Prozess gebildet, da ein größerer Neutronenüberschuss eine kürzere Halbwertszeit bedeutet und bei Halbwertszeiten von deutlich unter einem Jahr die Isotope in s-Prozess Umgebungen zerfallen bevor ein neues Neutron angelagert wird.

### Der s-Prozess Verzweigungspunkt ${}^{152}\text{Eu}$

Liegen  $\beta^-$  - Halbwertszeit und Neutroneneinfangszeit allerdings in der selben Größenordnung, ist dieses Isotop ein sogenannter *Verzweigungspunkt*. Bei dem Isotop  ${}^{152}\text{Eu}$  handelt es sich um einen solchen Verzweigungspunkt im s-Prozess Netzwerk. Die Bedeutung dieser Verzweigungspunkte ist offensichtlich: Um die Nukleosyntheseprozesse korrekt zu modellieren und damit Rechnungen und Simulationen durchzuführen um schlussendlich die genauen Abläufe der Entstehung aller Elemente zu verstehen, ist es notwendig, Verzweigungsverhältnisse und Raten exakt zu kennen.

Verschiedene Schwierigkeiten gilt es bei der Bestimmung dieser Raten zu überwinden. Eine davon ist die Radioaktivität des zu untersuchenden Verzweigungspunktes. Isotope mit sehr geringer Halbwertszeit eignen sich nicht gut für die Produktion eines Targets. Hingegen lassen sich radioaktive Strahlen oftmals einfacher produzieren, so dass die Reaktion umgekehrt wird. Dabei spricht man von einer Reaktion in inverser Kinematik. Dies ist beispielsweise möglich indem statt der Reaktion  ${}^A_Z X(n, \gamma){}^{A+1}_Z X$ , die Reaktion  ${}^{A+1}_Z X(\gamma, n){}^A_Z X$  untersucht.

Eine weitere Problematik findet sich in Gestalt von möglichen Anregungszuständen der Isotope. Im stellaren Plasma können sich Grund- und Anregungszustände von Isotopen im Gleichgewicht befinden. Da Anregungszustände andere Halbwertszeiten besitzen führt die zu abweichenden Zerfallszeiten des Isotops und damit anderen Verzweigungsverhältnissen als im Fall von nur im Grundzustand vorliegenden können. Im Fall von  ${}^{152}\text{Eu}$  können diese in Abhängigkeit der Umgebungstemperatur um bis zu vier Größenordnungen abweichen (vgl. [13]).

Um diese Anregungszustände bei schweren Kernen zu vermessen wurde im s405 Ex-



periment ein neues Verfahren getestet. Dabei wurde die Reaktion nicht nur in inverser Kinematik durchgeführt, was potentiell die Nutzung von radioaktiven Strahlisotopen erlaubt und somit das Problem der radioaktiven Isotope durch eine Zeitumkehr der Reaktion löst, sondern der Elektroneneinfang wurde durch eine Ladungsaustauschreaktion substituiert. Dies ist in diesem Fall möglich, da die beteiligten Operatoren identisch sind:

Bei  $\beta$ -Zerfällen spielen Gamow-Teller (GT) und Fermi-Übergänge (F) eine Rolle. Diese unterscheiden sich durch die Ausrichtung der Spin-Vektoren der emittierten Leptonen, die bei (GT)-Übergängen parallel stehen, während sie bei (F)-Übergängen antiparallel ausgerichtet sind. In astrophysikalischen Szenarien werden  $\beta$ -Zerfälle mittels Gamow-Teller Übergängen bevorzugt, wenn Elektroneneinfänge die bevorzugte Zerfallsmethode sind. Im Rahmen des mittels dem  $\vec{\tau}$ -Operator übertragenen Fermi-Überganges kann es zu einer Umkehr Isospin-Vektors kommen, während beim durch den  $\vec{\sigma}\vec{\tau}$ -Operator bestimmten Gamow-Teller-Übergang sowohl eine Isospin als auch eine Spinumkehr ablaufen können.

In Ladungsaustauschreaktionen verhält es sich analog. Wenn die Ladungsaustauschreaktion nur eine Isospinumkehr enthält, spielt der  $\vec{\tau}$ -Operator eine Rolle, ist eine Spinumkehr Bestandteil der Reaktion, dann wird diese mittels dem  $\vec{\sigma}\vec{\tau}$ -Operator beschrieben. Die Änderung des Spins wiederum erlaubt dem Tochterkern nach dem  $\beta$ -Zerfall einen angeregten Zustand einzunehmen. Die zugehörigen Matrixelemente für Fermi- und Gamow-Teller-Übergänge sind definiert als:

$$B(F, i \rightarrow f) = | \langle f | T_- | i \rangle |^2 \quad (6.3)$$

und

$$B(GT, i \rightarrow f) = \sum \mu | \langle f | \beta_{-(\mu)} | i \rangle |^2 \quad (6.4)$$

Dabei steht  $B(X, i \rightarrow f)$  für die Übergangsstärke,  $T_-$  und  $\beta_{-(\mu)}$  sind die Operatoren, die die Isospin- beziehungsweise Isospin-Spin-Umkehr beschreiben. Diese Elemente sind auch in der Beschreibung der (p,n) Reaktion vorhanden.

## Zusammenfassung

Für den Gamow-Teller Fall lässt sich mittels der Born-Näherung lösen:

$$\frac{d\sigma}{d\theta}(q \approx 0) = \left(\frac{\mu}{\pi\hbar^2}\right)^2 \frac{k_f}{k_i} N_{\sigma\tau} |J_{\sigma\tau}^{NN}|^2 B(GT, i \rightarrow f) \quad (6.5)$$

Die reduzierte Masse ist mit  $\mu$  bezeichnet und  $k_i$  und  $k_f$  stehen für die kinematischen Faktoren für die initiale und finale Welle, während  $N$  ein spezieller Verzerrungsfaktor und  $J^{NN}$  das Volumenintegral für die Nukleon-Nukleon Reaktion ist.

Es ist ersichtlich, dass die Matrixelemente die Überangsstärke  $B(GT, i \rightarrow f)$  enthalten. Daraus folgt, dass die Messung der (p,n) Wechselwirkungswahrscheinlichkeit bei  $\approx 0^\circ$  proportional zur Gamow-Teller Stärke ist [23, 24, 25].

Daraus lässt sich ableiten, dass die (p,n) Reaktion eine wirkungsvolle Methode zur Vermessung von astrophysikalisch motivierten nuklearen Reaktionen ist. Für die Validierung dieses Ansatzes bei schweren Kernen wurde das s405 Experiment vorgeschlagen.

## Das s405 Experiment und LENA

Die in den (p,n) Reaktionen emittierten Neutronen besitzen einen großen Winkel relativ zur Strahlachse und eine geringe kinetische Energie. Dies folgt unmittelbar aus der Forderung, dass der Streuwinkel im Schwerpunktsystem  $\approx 0^\circ$  beträgt. Die Reaktionskinematik ist in Abbildung 6.4 dargestellt: Auf der oberen Grafik sind die kinematischen Zusammenhänge der Winkelverteilungen abgebildet. Die untere Grafik zeigt das Ergebnis der simulierten Reaktionskinematik. Ausgehend von diesen Anforderungen an einen flexiblen, auf die Reaktionskinematik einstellbaren Detektor wurde der Low-Energy Neutron detector Array, kurz LENA, entwickelt. Dieses besteht im s405 Experiment aus fünfzehn Polyethylen Szintillatormodulen in der Dimension von  $1000 \times 10 \times 45 \text{ mm}^3$  mit einem Elektronenvervielfacher an jedem Ende. LENA kann je nach Bedarf im entsprechendem Abstand und Winkel um den Interaktionspunkt des Experimentes modular und unkompliziert aufgestellt werden. Für die Analyse der experimentell gewonnenen Daten muss die genaue Position der einzelnen Module vermessen werden. Diese konnte mittels der Photogrammetrie-Software Photomodeller rekonstruiert werden.

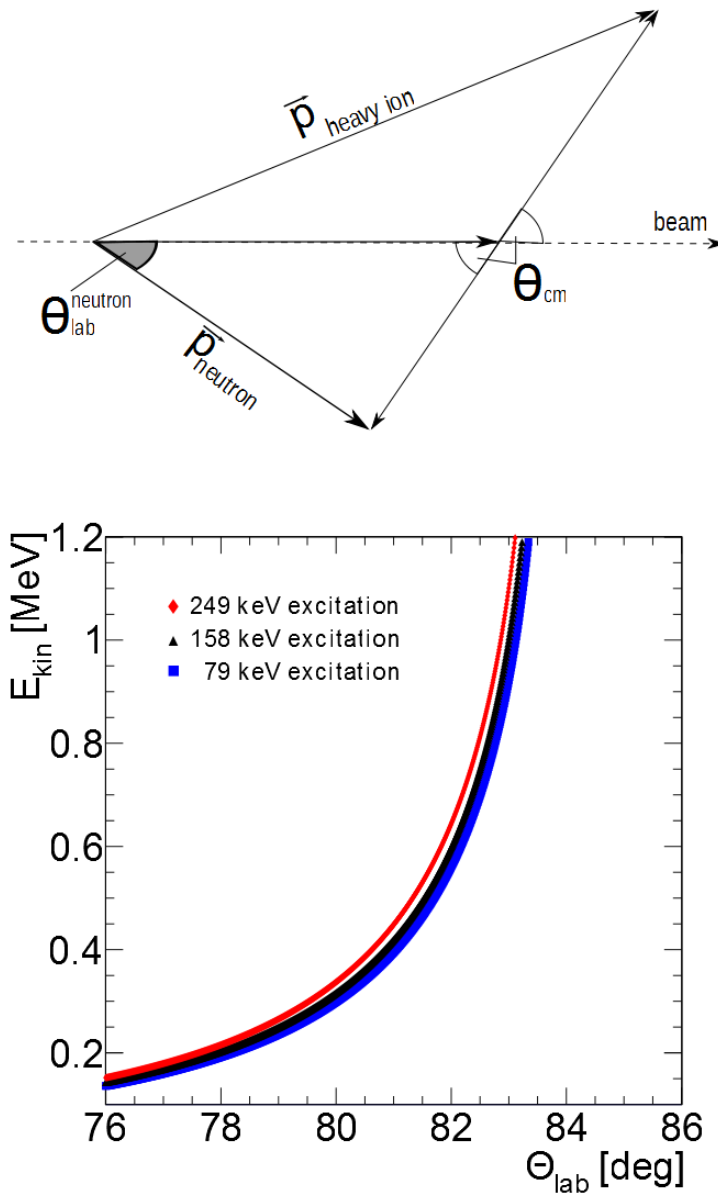


**Figure 6.4** – Die obere Grafik zeigt die kinematischen Zusammenhänge von Emissionswinkeln und Energien. Der untere Plot zeigt das Ergebnis einer kinematischen Simulation der emittierten Neutronenenergie in Relation des Emissionswinkels. Die drei verschiedenen Symbole stehen dabei für die drei verschiedenen Anregungszustände die  $^{152}\text{Eu}$  nach der Reaktion erreichen kann. In der Legende sind die entsprechenden Anregungsenergien vermerkt.

## Zusammenfassung

Das s405 Experiment wurde am LAND/R<sup>3</sup>B Aufbau im Cave C am GSI Helmholtz-zentrum für Schwerionenforschung GmbH in Darmstadt durchgeführt. Verschiedene Detektoren zur Positions-, Energie- und Zeitinformationsbestimmung wurden dabei genutzt. LENA wurde im erwarteten Emissionswinkel um das Target aufgestellt, ebenso ein LaBr<sub>3</sub>:Ce Detektor zur Vermessung der Photonen aus der <sup>152</sup>Eu Abregung.

Für die Vermessung der (p,n) Reaktion wurde ein CH<sub>2</sub> Target genutzt. Um den Kohlenstoffanteil der reagierten Daten zu bestimmen, wurden zudem Daten mit einem reinen Kohlenstofftarget aufgenommen. Ebenso wurden Untergrundsignale durch Interaktion des Ionenstrahls mit dem Aufbau berücksichtigt. Nach der Kalibrierung der genutzten Detektoren wurden die Daten analysiert. Der Fokus bei der Analyse des Experiments lag auf der Rekonstruktion des gezeigten simulierten Neutronenspektrums. Die kinetische Energie der Neutronen wurde dabei mittels der Formel

$$E_n^{\text{kin}} = \left( \frac{1}{\sqrt{1 - \left(\frac{v}{c}\right)^2}} - 1 \right) mc^2 \quad (6.6)$$

aus der Flugzeit und dem Flugweg berechnet.

Dabei wurden verschiedene Qualitätskriterien auf die Daten angewendet. Die Entwicklung dieser über den Zeitraum von mehreren Monaten wurde unter dem Gesichtspunkt der Signaloptimierung geführt. Neben der Nutzung von Flugzeiten, gemessener Energie in den Detektoren und der Abstrahlung von Gammas durch die Abregung der <sup>152</sup>Eu Kerne stellte im besonderen Maße die Trennung von Reaktionsprodukten und un-reagierten Strahl eine Herausforderung da. Aufgrund der hohen Rate der einlaufenden Ionenpakete und deren niedrigen Energie in Relation zur Masse, konnten die etablierten Methoden nicht einfach angewandt werden. Durch die Kombination mehrerer Methoden konnte zumindest der Großteil des un-reagierten Strahles aus den Daten entfernt werden, wenn auch nicht ohne Verluste bei den Reaktionsprodukten.

Da es sich bei LENA um einen flexiblen und variablen Detektor handelt, wurde dessen genaue Position mittels einer Spezialsoftware rekonstruiert und genutzt, um nicht nur die korrekten Flugwege sondern auch die Winkel der individuellen Detektorvolumina gegenüber der Strahlachse zu bestimmen.

Damit konnte das Verhältnis der kinetischen Energie als Funktion des Abstrahlwinkels für jedes Neutron bestimmt und die sich daraus ergebenden Daten mit der Berechnung (Abbildung 6.4) verglichen werden. Dies ist in Abbildung 6.5 dargestellt.

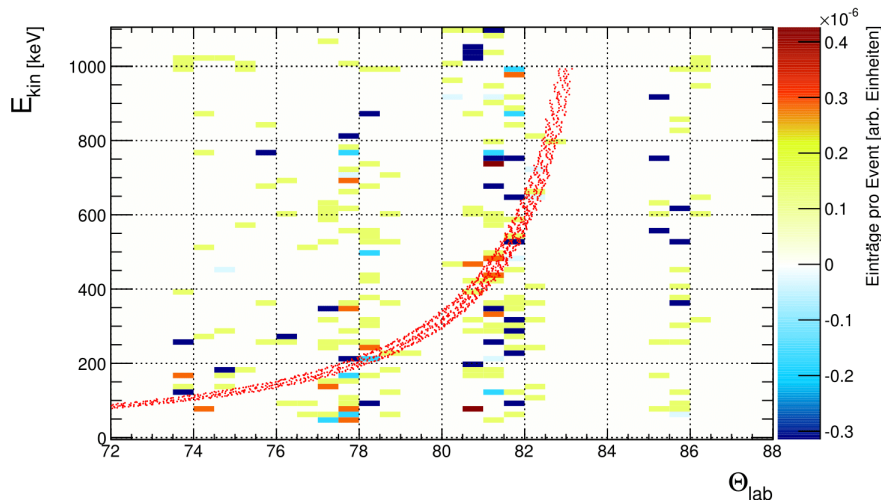


**Figure 6.5** – Rekonstruierte Verteilung von  $E_{\text{kin}}^{\text{Neutron}}$  in Abhängigkeit von  $\Theta_{\text{lab}}$ . Das zweidimensionale Spektrum zeigt die mit LENA gemessene Neutronenenergie in Abhängigkeit des gemessenen Emissionswinkels. Dabei wurden alle in der Analyse erarbeiteten Qualitätskriterien angewandt. Die roten Linien zeigen die erwartete Neutronenverteilung.

### Simulation der Detektorreaktion auf niederenergetische Neutronen

Da die Menge der im Rahmen des s405 Experimentes gewonnenen Daten nicht ausreicht, um eine statistisch haltbare Aussage über den Wirkungsquerschnitt zu machen und um die Reaktion von LENA auf die erwarteten Neutronenenergie sowie Neutronenverteilungen zu studieren, wurden zusätzlich Simulationen mittels GEANT3 durchgeführt. Neben den drei in der  $^{152}\text{Sm}(p,n)^{152}\text{Eu}$  Reaktion erwarteten Anregungsenergien des  $^{152}\text{Eu}$  Kerns wurden außerdem weitere Anregungsenergien simuliert, um erkennen zu können, ab welchen Anregungsenergieunterschieden LENA ohne weitere Detektoren die verschiedenen Anregungszustände trennen könnte. Während dies bei den Anregungsenergien von 79, 158 und 249 keV nicht der Fall ist, kann schon der Unterschied zwischen 249 und 500 keV ausreichend aufgelöst werden. Die ist in Abbildung 6.6 aufgezeigt.

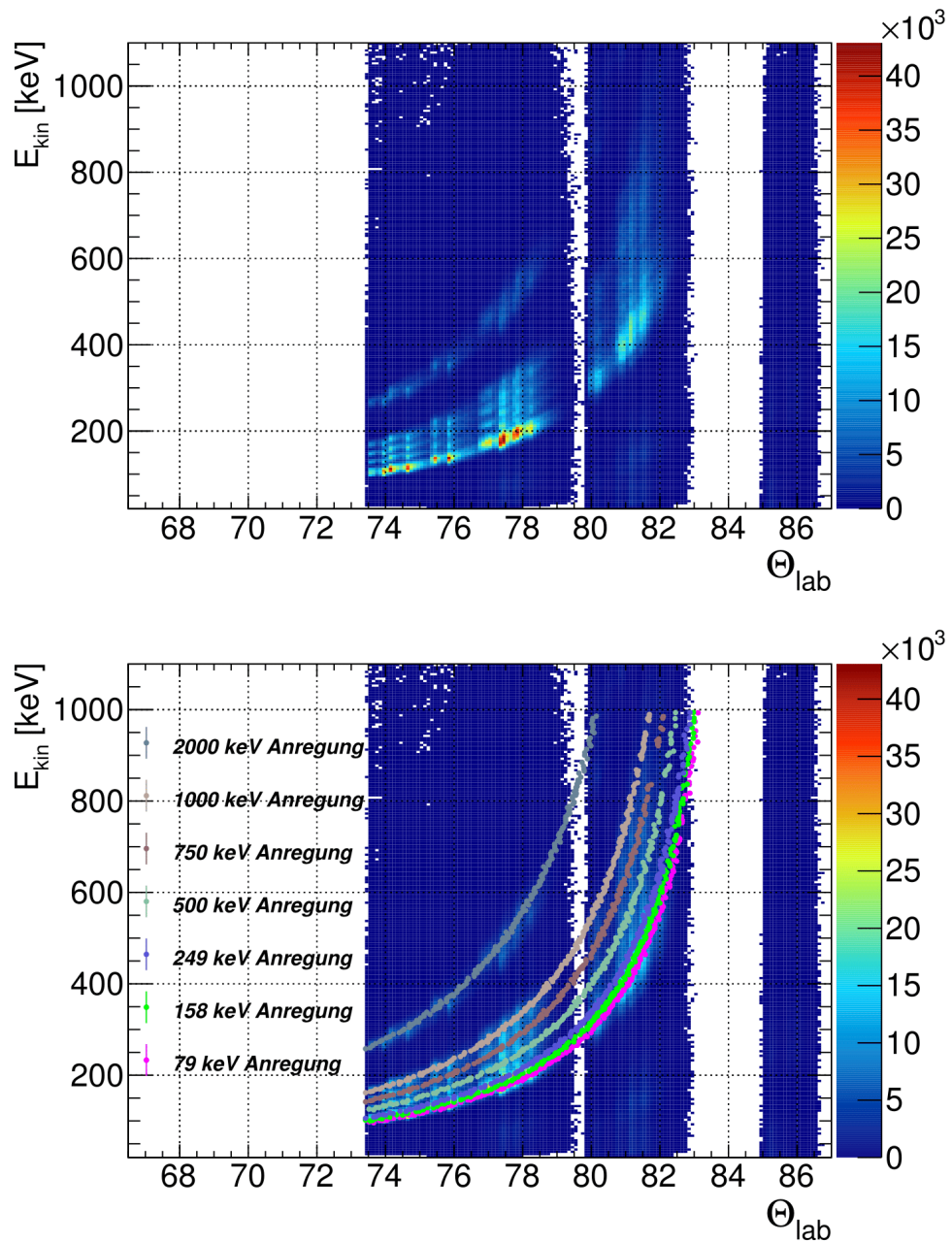


**Figure 6.6** – Simulierte Reaktion von LENA auf niederenergetische Neutronen. Verschiedene Anregungszustände zwischen 79 und 2000 keV wurden simuliert um die Effizienz und das Auflösungsvermögen von LENA zu bestimmen. Die drei im s405 Experiment erreichten Anregungszustände können von LENA nicht ohne die Informationen weiterer Detektoren aufgelöst werden.

## Ergebnis und zukünftige Vorhaben

Es konnte gezeigt werden, dass mit LENA die Messung von niederenergetischen Neutronen gut möglich ist. Die intrinsische Detektorauflösung ist gut genug, um verschiedene Anregungsniveaus des Tochterkerns bei Kernreaktionen ausreichend zu trennen und somit Wirkungsquerschnitte und Reaktionswahrscheinlichkeiten zu bestimmen, wenn die Anregungsenergie mindestens 120 keV auseinander liegt. Die Messung von Reaktionen unter der Ausstrahlung von niederenergetischen Neutronen kann mit Hilfe weiterer Detektoren verbessert werden. Eine Auswahl möglicher Detektoren, der untersuchten Bedingungen und deren Effizienz wurden im Rahmen dieser Arbeit transparent dargestellt. Als problematisch stellt sich die im Rahmen des s405 Experiments gewonnene Statistik dar. Insgesamt wurden nur 48 Stunden lang Daten aufgenommen und nach der Datenselektion und Abzug des Untergrundes blieben nicht genug Events übrig um eine qualitative Aussage über die - recht kleine - Wechselwirkungsquerschnitte der Reaktion  $^{152}\text{Sm}(p,n)^{152}\text{Eu}$  und damit über den Elektroneneinfang an  $^{152}\text{Eu}$  zu treffen. Eine Strahlzeit von etwa zwei Wochen wäre hierfür erforderlich.

Im Rahmen des Erweiterungs-Neubaus der FAIR-Anlage am GSI Helmholtzzentrum für Schwerionenforschung GmbH wird auch der ALADIN/R<sup>3</sup>B Aufbau erweitert. Neben einem neuen Magneten und verbesserten Versionen der auch in dieser Arbeit beschriebenen Detektoren könnte dabei ein Detektor wie LENA nahe des Hauptinteraktionspunktes gebaut werden, um niederenergetische Neutronen zu registrieren und somit zu den gewünschten kinematisch vollständigen Vermessungen der kernphysikalischen Reaktionen beizutragen. Dies ist von besonderem Interesse bei den in dieser Arbeit thematisierten Ladungsaustauschreaktionen, die einen neuen Zugang zu stellaren Reaktionsraten von hochangeregten und instabilen Kernen ermöglichen.





# Bibliography

- [1] T. Heftrich. *Stellare Produktions- und Destruktionsraten des radioaktiven Isotops  $^{60}\text{Fe}$* . Dissertation, Institut für Angewandte Physik, Goethe-Universität, Frankfurt am Main, 2013. 3
- [2] K. Lodders. Solar system abundances and condensation temperatures of the elements. *The Astrophysical Journal*, 591(2):1220–1247, 2003. 3
- [3] G. M. Fuller, G. J. Mathews, and C. R. Alcock. Quark-hadron phase transition in the early universe: Isothermal baryon-number fluctuations and primordial nucleosynthesis. *Physical Review D*, 37(6):1380, 1988. 4
- [4] B. Povh, K. Rith, C. Scholz, and F. Zetsche. *Teilchen und Kerne*. Springer Verlag, 1999. 4, 6, 20
- [5] A.D. Doglov. Big bang: Nucleosynthesis. *Nuclear Physics - Proceedings Supplements*, (137-43), 2002. 4
- [6] C. E. Rolfs and W. S. Rodney. *Cauldrons in the Cosmos*. University Of Chicago Press, 2005. 4, 6, 14
- [7] E.M. Burbidge, G.R. Burbidge, W.A. Fowler, and F. Hoyle. Synthesis of the elements in stars. *Reviews of Modern Physics*, 29(4):547–650, 1957. 6, 17, 18
- [8] H. A. Bethe. Energy production in stars. *Physical Review*, 55:434, 1939. 6
- [9] F. Käppeler. The origin of the heavy elements: The s process. *Progress in Particle and Nuclear Physics*, 43:419–483, 1999. 8, 13
- [10] F. Käppeler, R. Gallino, S. Bisterzo, and W. Aoki. The s process: Nuclear physics, stellar models, and observations. *Reviews of Modern Physics*, 83(1):157–194, 2011. 8, 14, 15

## BIBLIOGRAPHY

- [11] M. Busso, R. Gallino, and G.J. Wasserburg. Nucleosynthesis in asymptotic giant branch stars: Relevance for galactic enrichment and solar system formation. *Annual Review of Astronomy and Astrophysics*, 37(1):239–309, 1999. 8, 14
- [12] R. Gallino et. al. Evolution and nucleosynthesis in low-mass asymptotic giant branch stars. ii. neutron capture and the s process. *The Astrophysical Journal*, 497(1):388, 1998. 8
- [13] K. Takahashi and K. Yoko. Beta-decay rates of highly ionized heavy atoms in stellar interiors. *Physical Review C*, 36:1522–1528, 1987. 12, 104
- [14] U. Ratzel et al. Nucleosynthesis at the termination point of the s process. *Physical Review C*, 70:065803, 2004. 12
- [15] D. D. Clayton and R. A. Ward. s process studies: Exact evaluation of an exponential distribution of exposures. *The Astrophysical Journal*, 193:397–400, 1974. 13
- [16] R. Reifarth, C. Lederer, and F. Käppeler. Neutron reactions in astrophysics. *Journal of Physics G: Nuclear and Particle Physics*, 41(5), 2014. 15
- [17] A. G. W. Cameron. Nuclear reactions in stars and nucleogenesis. *Publications of the Astronomical Society of the Pacific*, 69(408):201–222, 1957. 17, 18
- [18] M. Arnould and S. Goriely. The p process of stellar nucleosynthesis: Astrophysics and nuclear physics status. *Physics Reports*, 384(1-2):1–84, 2003. 17, 18
- [19] T. Rauscher. Origin of p-nuclei in explosive nucleosynthesis. *Proceedings of Science. NIC XI*, (059), 2010. 18
- [20] S. Goriely, J. Jose, M. Hernanz, M. Rayet, and M. Arnould. He-detonation in sub-chandrasekhar CO white dwarfs: A new insight into energetics and p process nucleosynthesis. *Astronomy and Astrophysics*, 383:L27–L30, 2001. 18
- [21] C. Froehlich et al. Neutrino-induced nucleosynthesis of  $A > 64$  nuclei: The  $\nu p$  process. *Physical Review Letters*, 96(14), 2006. 18
- [22] C.S. Wu, E. Ambler, R.W. Hayward, D.D. Hoppes, and R.P. Hudson. Experimental test of parity conservation in beta decay. *Physical Review*, (105):1413–1415, 1957. 21
- [23] T. Taddeucci et al. The (p,n) reaction as a probe of the beta decay strength. *Nuclear Physics*, A469(125), 1987. 23, 106

## BIBLIOGRAPHY

- [24] G. R. Satchler. The distorted-waves theory of direct nuclear reactions with spin-orbit effects. *Nuclear Physics*, 55:1–33, 1964. 23, 106
- [25] F. Osterfeld. Nuclear spin and isospin excitations. *Review of Modern Physics*, 64:491, 1992. 23, 106
- [26] ATOMKI Debrecen. <http://www.atomki.hu/>. Contact: Dr. Attila Krasznahorkay, Head of the Nuclear Physics Division. 29
- [27] C. Langer. *Coulomb Dissociation of  $^{31}\text{Cl}$  and  $^{32}\text{Ar}$  - constraining the rp process*. Dissertation, Institut für Angewandte Physik, Goethe-Universität, Frankfurt am Main, 2012. 29, 44, 101
- [28] GEANT - Detector Description and Simulation Tool. via official webpage. retrieved 07.05.2014. 32
- [29] C. Langer et al. Simulations and developments of the low-energy neutron detector array lena. *Nuclear Instruments and Methods in Physics Research A*, (659):411–418, 2011. 32
- [30] R. Beyer et al. Proton-recoil detectors for time-of-flight measurements of neutrons with kinetic energies from some tens of kev to a few mev. *Nuclear Instruments and Methods in Physics Research A*, (575):449, 2007. 32
- [31] Layout of the GSI facility. via official webpage, 2012. retrieved 07.04.2014. 36, 99
- [32] Günther Ickert. internal communication. 38
- [33] A. Giaz et al. Characterization of large volume 3.5" x 8"  $\text{LaBr}_3:\text{Ce}$  detectors. *Nuclear Instruments and Methods in Physics Research, A*(729):910–921, 2013. 40
- [34] E.V.D. van Loef et al. High-energy-resolution scintillator:  $\text{Ce}^{3+}$  activated  $\text{LaBr}_3$ . *Applied Physics Letters*, 79:1573, 2001. 40
- [35] I. Mazumdar et al. Studying the properties and response of a large volume (946  $\text{cm}^3$ )  $\text{LaBr}_3:\text{Ce}$  detector with  $\gamma$ -rays up to 22.5 mev. *Nuclear Instruments and Methods in Physics Research A*, (705):85–92, 2013. 40
- [36]  $\text{LaBr}_3:\text{Ce}$ . Oliver Wieland, via personal communication. retrieved 18.02.2014. 40
- [37] J. Cub, G. Stengel, and A. Grünschoß et al. A large-area scintillating fibre detector for relativistic heavy ions. *Nuclear Instruments and Methods in Physics Research A*, (402):67–74, 1998. 41
- [38] Photomodeler. <http://www.photomodeler.com/index.html>. 54

## BIBLIOGRAPHY

- [39] H. A. Bethe and AshkinJ. Passage of radiation thorough matter. *Experimental Nuclear Physics*, 1(2):253, 1953. 59
- [40] H.J. Wollersheim et al. Rare isotopes investigation at gsi (rising) using gamma-ray spectroscopy at relativistic energies. *Nuclear Instruments and Methods in Physics Research A*, (537):637–657, 2005. 74
- [41] M. J. Martin. Nuclear data sheets for  $A = 152$ . *Nuclear Data Sheets*, 114(11):1497, 2013. 75
- [42] M. Sasano et. al. Gamow-teller transition strengths from  $^{56}\text{Ni}$ . *Physical Review Letters*, 107(20):202501, 2011. 98

# List of Figures

1.1	Solar abundances of isotopes	3
1.2	Schematic chart of nuclides	8
1.3	The s process branching point $^{152}\text{Eu}$	11
1.4	The effective $\beta$ -decay rates of $^{152}\text{Eu}$	12
1.5	The product of s-process abundance and cross section as a function of the mass of the isotopes	15
1.6	Principle mechanisms of a (p,n) reaction	21
1.7	Gamow-Teller and Fermi transitions	22
2.1	Simulation of the neutron kinematics emitted from the $p(^{152}\text{Sm}, ^{152}\text{Eu})n$ reaction	27
2.2	Two different LENA alignments	29
2.3	Picture of LENA during s405	34
3.1	GSI Helmholtzzentrum für Schwerionenforschung GmbH	36
3.2	The s405 experimental setup	37
3.3	The ROLU detector	38
3.4	The POS detector	39
3.5	The $\text{LaBr}_3:\text{Ce}$ detector	40
3.6	The GFI detector	41
3.7	The big time-of-flight wall as used in the LAND/R <sup>3</sup> B setup	42
3.8	Magnetic field distribution of the large dipole magnet	44

## LIST OF FIGURES

4.1	Calibrated LaBr <sub>3</sub> :Ce spectra	51
4.2	Position determined via time and energy in LENA	53
4.3	Three-dimensional model of LENA around the target	55
4.4	Scheme of the correlation of interaction angle, interaction point and flight path	56
4.5	Calibration of GFI	58
5.1	Time-of-flight spectrum gathered with LENA	65
5.2	Inverted velocity spectrum gathered with LENA	67
5.3	$E_{kin}^{neutron}$ at the data selection step 2	70
5.4	The measured $E_{dep}$ as a function of the calculated $E_{kin}^{neutron}$ within LENA	72
5.5	$E_{kin}^{neutron}$ at the data selection step 3	73
5.6	Calculated Doppler-shift for $\gamma$ -rays originating from an isotope with an energy of 300A MeV	74
5.7	Calculated light-aberration for $\gamma$ -rays originating from an isotope with an energy of 300A MeV	76
5.8	$E_{kin}^{neutron}$ at the data selection step 4	77
5.9	Determined $Z$ using the TFW with DSS 2 and DSS 4	79
5.10	Determined $Z$ using the TFW with DSS 4 and an additional constraint on $E_{kin}^{neutron}$	80
5.11	Determined $Z$ using the tracker with DSS 2 and DSS 4	82
5.12	Determined $Z$ using the tracker with DSS 4 and an additional constraint on $E_{kin}^{neutron}$	83
5.13	Two-dimensional correlation plot of $Z_{Track}$ and $Z_{TFW}$	85
5.14	$E_{kin}^{neutron}$ at the data selection step 5	86
5.15	Reconstructed dependence of $E_{kin}^{neutron}$ on $\Theta_{lab}$ at DSS 4	89
5.16	Reconstructed dependence of $E_{kin}^{neutron}$ on $\Theta_{lab}$ at DSS 5	89
5.17	Simulation of the measurement of low-energy neutrons originating from <sup>152</sup> Eu with excitation energies of 79, 158 and 249 keV	92
5.18	Simulation of the measurement of low-energy neutrons stemming from <sup>152</sup> Eu with varying excitation energies from 79 to 2000 keV LENA	94

## LIST OF FIGURES

6.1	Reconstructed dependence of $E_{\text{kin}}^{\text{neutron}}$ on $\Theta_{\text{lab}}$ without $\gamma$ -energy constraint	97
6.2	The upcoming FAIR facility	99
6.3	The future R <sup>3</sup> B setup at FAIR	101
6.4	Simulierte Neutronenkinematik der $p(^{152}\text{Sm}, ^{152}\text{Eu})n$ Reaktion	107
6.5	Rekonstruierte Verteilung von $E_{\text{kin}}^{\text{Neutron}}$ in Abhängigkeit von $\Theta_{\text{lab}}$	109
6.6	Simulierte Reaktion von LENA auf niederenergetische Neutronen	110





# List of Tables

2.1	Experimental details of s405	26
2.2	Specific characteristics of the Low-Energy detector Array LENA	32
3.1	Target details for the s405 experiment	43
4.1	s405 Trigger Patterns	47
4.2	Used $\gamma$ -ray sources used for the LaBr <sub>3</sub> :Ce calibration	50
4.3	List of the distances and adjustment angles relative to the beam line for each LENA bar	57
5.1	Cut range for doppler-shift corrected $\gamma$ -ray energy from excited <sup>152</sup> Eu	75
5.2	Overview of the complete set of data selection steps used in s405	87
5.3	Overview of the determined efficiencies of LENA	93



# Acknowledgments

I thank Professor Dr. René Reifarth for his support throughout the last years. He welcomed me in his working group and always supported me with helpful and pragmatic point of views. It was a great experience working in his group and allowed me to develop my understanding of physics further.

I want to thank my second supervisor Dr. Michael Heil, too. It was a pleasure working with him on various problems and his patience and unique way of explaining scientific problems and solutions was a huge help, not only for me. A big *thank you* is dedicated to Dr. Kerstin Sonnabend who was not only my second corrector of my thesis but also has a huge share in forming the absolutely pleasant work environment we have in the experimental astrophysics group at GUF. I also have to thank Dr. Ralf Plag. I can not imagine how much more I would have got stuck without his help and advice and patience. And I guess that is not only true for me.

I am glad I finished my Ph.D. in the experimental astrophysics working group at the Goethe Universität Frankfurt. It was a great time with a lot of nice, kind and fun people. I really enjoyed the atmosphere there. From all the people being a part of it, current students and researchers as well as alumni likewise, I want to address some in particular. I especially want to thank Zuzana Slavkovská. Ďakujem Ti za všetky úsmevy a energiu, ktorú si priniesla do môjho života. Si jeden z najmilších a najlepších ľudí na tejto planéte. Zostaň taká aká si.

And Susi Kräckmann and Jennifer Ostermüller for all the fun times in the office. Wouldn't be the same all by myself or with anybody else.

Gratitude is owed to Dr. Christoph Langer and Dr. Jan Glorius for helping me with a lot of stuff, from setting ups electronics to analyzing. Same is true for the involved LAND/R<sup>3</sup>B crew at GSI. A bunch of very smart and nice people, a pleasure to work with. Special thanks to Marcel Heine, who helped me a lot with LENAs electronics and introduced me to the photodeler software. And to Dr. Oliver Wieland from

INFN for his help with the LaBr<sub>3</sub>:Ce detectors.

I can not stretch out how grateful I am for my family. They supported me throughout my life. Without them, I can not even imagine where I would be.

And a big thank you to my friends, who understand me disappearing behind my desk for month, but never stopped trying to get me out in the real life now and then.

Last but not least I want to thank the s405 collaboration. A international group of physicists who made the s405 experiment possible.

### **The s405 collaboration:**

Sebastian Altstadt, Leyla Atar, Thomas Aumann, Souyma Bagchi, Clemens Beinrucker, Nivas Blasi, Konstanze Boretzky, Angela Bracco, Sergio Brambilla, Franco Camera, Margit Csatlos, Paloma Diaz Fernandez, Enrico Fiori, Micaela Fonseca, Simon Gannon, Umesh Garg, Max Gilbert, Jan Glorius, Kathrin Göbel, Janos Gulyas, Tanja Heftrich, Michael Heil, Marcel Heine, Ana Henriques, Matthias Holl, Hakan T. Johannsson, Nasser Kalantar-Nayestanaki, Alexander Koloczek, Susanne Kräckmann, Attila Krasznahorkay, Christoph Langer, Bastian Löher, Jorge Machado, Justyna Marganiec, Benedicte Million, Alina Movsesyan, Mohammad Ali Najafi, Ralf Plag, (Moritz Pohl), Ganna Rastrepina, René Reifarth, Catherine Rigollet, Marko Röder, Dominic Rossi, Deniz Savran, Stefan Schmidt, Philipp Schrock, Haik Simon, Kerstin Sonnabend, Laszlo Stuhl, Taniya Thomas, Janos Timar, Meiko Volknandt, Vasily Volkov, Felix Wamers, Mario Weigand, Oliver Wieland and Philip J. Woods.

Thank you.

This work was made possible by the Helmholtz Graduate School for Hadron and Ion Research *HGS-Hire for FAIR*.

# Curriculum Vitae

## Moritz Pohl

### Miscellaneous

---

**Date of Birth** 27.09.1984  
**Place of Birth** Frankfurt am Main, Germany  
**Citizenship** German  
**Marital Status** unwed

### Education

---

#### **Ph.D. Student**

04.2011 - current  
Goethe Universität Frankfurt am Main, Germany

#### **M.Sc., Physics**

11.2008 - 03.2011  
Goethe Universität Frankfurt am Main, Germany  
*Studie zur Messung von  $\psi(2S)$  Mesonen mit dem ALICE Detektor am LHC*

#### **B.Sc., Physics**

10.2005 - 10.2008  
Goethe Universität Frankfurt am Main, Germany  
*Effizienzstudien zur  $K_S^0$  - Rekonstruktion bei 158A GeV Pb-Pb Kollisionen*

#### **Abitur**

06.2004  
Ernst Reuter Schule I Frankfurt am Main, Germany

